# Master Thesis

## Cooling Drag Estimation for Ducted Ram-Air Heat Exchangers

AE5222: Thesis Flight Performance & Propulsion

Julien Bengt Svensson

Delft University of Technology

TU Delft

# Master Thesis

## Cooling Drag Estimation for Ducted Ram-Air Heat Exchangers

by

Julien Bengt Svensson

| | |
|---|---|
| Company Supervisor: | J. Pirnar |
| Academic Supervisor: | W. Baars |
| Thesis Duration: | 09/09/2024 - 19/09/2025 |
| Faculty: | Faculty of Aerospace Engineering, TU Delft |

| | |
|---|---|
| Cover: | Heart Aerospace X1 parked and charging |
| Style: | TU Delft Report Style, with modifications by Daan Zwaneveld |

TU Delft

# Preface

First and foremost, I would like to thank *Pipistrel* for proposing the thesis topic and for sponsoring my thesis work. Jernej, you have been a fantastic supervisor, probably the best that a student could wish to have for this topic. You have largely influenced my understanding of this field and shaped the genuine interest that I have developed in it. Even if I seemed lost at times, you showed great patience and offered your support. I sincerely want to thank you for that.
Thank you also to Woutijn for acting as the academic supervisor. You always offered some valuable insight and your critical points of view have helped me develop the thesis into the final product that it has become.

Handing in my thesis as the new academic year starts offers a great deal of inspiration to reflect on the past six years that I have spent as a student at TU Delft. Seeing the new students arrive, I relive the moments that I experienced when I first came here - the expectations I had and the doubts that I felt. Hardly could I have imagined what adventures I was to embark on and how much I could learn.
Six years later, it turns out that becoming an Aerospace Engineer is no easy task and that in order to get there, one must struggle. But the struggle has been worth it.
In that sense, I am extremely grateful to my parents and my sister, who have supported me throughout this time, helped me move here and there and who have always given their utmost so that I could focus on my studies. I am truly blessed to have you.

To all my friends, I also want to thank you. Whether you helped me directly through your input (special thanks to Sahir), or indirectly by simply being there for me, every one of you has at least contributed a tiny bit to this thesis.

Lastly, I want to thank the two special girls who have accompanied me during the thesis - Rhada and Debbie. One of them is a dog, the other one is my beloved partner. Thank you to Rhada for taking me on walks to digest some of my thesis writing. Thank you Debbie for bringing so much joy to my life and for listening to me ramble about ducted ram-air heat exchangers.

With all nice things having been said: Enjoy the read!

*Julien Bengt Svensson*
*Delft, September 2025*

# Summary

Among the many challenges faced by hydrogen electric and battery electric aviation, the effective dissipation of waste heat is one. Fuel cells (FC), batteries and other power electronics generate heat, but at the same time have a limited range of temperatures at which they can operate to prevent premature degradation or even catastrophic failure, as can be the case for thermal runaway in batteries. This issue necessitates the development of dedicated thermal management systems (TMS) which remove heat from the source and pass it on to the ambient air through ducted ram-air heat exchangers.
The air that is captured by the duct and that passes through the heat exchanger (HX) experiences internal pressure losses due to the ducting and the pressure drop that is caused by the HX. Under the right circumstances, however, the potential of the waste heat that is rejected into the air stream can be turned into a small thrust force. Simultaneously, due to their size and the need for ducting, these HXs can not be integrated flush into the fuselage of the aircraft. Instead, the ducted ram-air HX installations must be housed in excrescences of the fuselage. Inevitably, this causes additional external drag.

The aim of this thesis is to generate tools that quantify the cooling drag of ducted ram-air heat exchangers, taking into account both the internal losses as well as the external drag caused by such installation. For this, the internal drag is assessed through a semi-empirical momentum loss method that is incorporated in a *Python* tool. This method includes a diffuser model, which is sensitive to the shape and the operational conditions of the duct. The outlet nozzle is assumed to be ideal throughout most of this work although the effect of introducing nozzle losses is discussed in a sensitivity analysis.
Users of the tool can choose between two types of HX. Both being crossflow HX, they are similar in nature but have nuances when it comes to channel geometries and the heat transfer surfaces. Both the heat transfer and pressure drop are design sensitive and based on models found in literature. The heat transfer is determined with the $\epsilon - NTU$ method.
To generate the external shape of the installation, a function is made that fits a duct cowling around a given heat exchanger, which can then be modeled in *OpenVSP*, a CAD program. This makes the design and sizing process more tangible than in a purely abstract model and furthermore allows for the estimation of the external drag.
The external drag of the installation is determined with a CFD simulation using *openFoam*, where the duct inflow and outflow from the internal analysis can be imposed as boundary conditions on the closed surface of the CAD model. Due to the computationally expensive nature of this method, a surrogate model is generated for the external drag, which yields a drag coefficient that is both sensitive to the design and the spillage rate of the duct, a measure of how much of the incoming air is diverted around the duct due to internal resistances, instead of entering it.
These three tools, which are the internal model, the duct shape generator and the surrogate model for the external drag, are at last combined in an optimization strategy which aims to reduce the cooling drag in cruise. An exemplary hydrogen FC liquid cooled TMS with a 1 MW electric power output is used to generate representative results and to perform a sensitivity study which analyses the effect of duct design choices, the assumed nozzle efficiency, the TMS operating temperature and the critical atmospheric temperature offset.

The results show that the cooling drag varies starkly throughout the mission. Cooling drag is much larger at take-off than in cruise, since the higher on-ground temperature necessitates a larger air mass flow than at cruise altitude to match the required heat transfer rate. In cruise, the installation manages to offset some drag internally by providing a thrust force from the waste heat. This phenomenon, commonly known as the Meredith effect, is however, largely undone if nozzle losses are introduced.
By performing the optimization for a case where only the internal cooling drag in cruise is minimized, instead of the sum of internal and external contributions, another important lesson regarding the Meredith effect is learned. Namely, that in cases where the Meredith effect is maximally harnessed, the total cooling drag ends up being larger. This is because the installed HX ends up having a much larger frontal area, resulting in additional external cooling drag.

Therefore, caution is advised when seeking to exploit the Meredith effect. Firstly, its extent is largely dictated by the ducting efficiency and secondly, over-focusing on reducing or even annulling cooling drag by exploiting the Meredith effect leads to worse drag performance and oversized designs.
Changing the refrigerant inlet temperature of the HX, and thereby the operating temperature of the TMS, leads to interesting insights. When lowering the the TMS operating temperature by 20 °C, an increase in cooling drag at take-off of nearly 75% is found. However, the cooling drag in cruise remains unchanged. While the size of the ducted ram-air HX installation grows significantly with decreasing TMS operating temperature, the expected rise in external drag is largely offset by the inlet lip suction effect that occurs when the inlet spills air in cruise. Since the larger installations turn out to have higher spillage rates than the more compact ones, the lip suction effect, accounted for in the surrogate external drag model, is more pronounced. As a result, when lowering the TMS operating temperature, in cruise the very slight increase in external drag is even compensated by a stronger internal drag offset due to heat recovery.
Nevertheless, this finding reflects only the cooling drag. The significant difference in HX installation size makes a higher TMS operating temperature the clear favorite, not only because they would be handier to integrate into the airframe, but also because a more compact HX and duct translates to lower mass, significantly improving the performance of an aircraft.
A similar behavior is seen when the ambient temperature at take-off is varied. Since this has a direct influence on the most critical temperature gap between the ambient and the refrigerant throughout a mission, designing the system to reject heat under higher ambient temperatures leads to a larger installation. Counterintuitively, an installation sized to handle extremely hot days (45 °C) at take-off, with the devised method, causes less cooling drag under the same cruise conditions than a more compact installation that handles only moderately hot days (30 °C). This observation regarding cooling drag runs down to the improved heat recovery capabilities and increased lip suction effect of the larger installation in cruise. Despite this, concerns regarding mass and integrability of larger installations still offer clear arguments in favor of smaller, but perhaps less operationally flexible, installations.

The validation of the tools shows that the results from the external drag simulations and the constructed surrogate model are within a satisfactory range. Likewise, the extent of the lip suction effect due to spillage seems properly predicted, when compared to scientific literature. There is some need to improve the heat exchanger models, as both the heat transfer and the pressure drop partially show strong divergence from experimental data. Despite this, the results and usefulness of the tools for their intended purpose are not undermined.

The conclusion of this work is that cooling drag for electric propulsion aircraft, in this case a hydrogen FC powered one, represents a considerable adverse force. Moreover, the scale of the heat exchangers that are part of the TMS, necessitates more focus than was previously allocated on how these can be integrated on board aircraft while minimizing the mass and external drag of the installations. In that sense, it is also clearly shown that neglecting this external drag in the design process, and only aiming to minimize internal losses of the installation leads to worse designs in terms of total cooling drag and installation size.

The key recommendations for future work regard amendments to the tools and further research surrounding cooling drag and HX installations. The internal drag model should be extended to analyze the effect of adding a puller fan to the system which remedies internal pressure losses. Moreover, a critical study concerning overall power savings of such addition also accounting for losses due to a windmilling puller fan should be performed.
For the fuselage bound HX installation the effect of the boundary layer created by the fuselage on air intake and external drag needs be investigated. Initial results in this work point towards a reduction in external drag if the diverter height can be reduced or even removed altogether. However, these claims need to be further substantiated with more accurate simulations and boundary layer models.
By shifting the focus from pure cooling drag to a single value of power consumption due to drag, mass and TMS pumping power, a more conclusive picture of the comparative performance of different installations can be made. Appropriate mass and pumping power models should be added to the tools in order to facilitate this analysis.
Lastly, incorporating other TMS architectures and technologies in the tools, such as 2-phase flows and a microtube HX could be interesting to assess the benefits of adopting these advanced technologies.

# Contents

# List of Figures

# List of Tables

# Nomenclature

## Abbreviations

| Abbreviation | Definition |
|---|---|
| CFD | Computational Fluid Dynamics |
| DEP | Distributed Electric Propulsion |
| DRAX | Ducted Ram-Air Heat Exchanger |
| FTHX | Flat Tube Finned Heat Exchanger |
| HX | Heat Exchanger |
| ISA | International Standard Atmosphere |
| LCS | Liquid Cooling System |
| LH2 | Liquid Hydrogen |
| MDO | Multi-Disciplinary Optimization |
| P2P | Pumped Two-Phase cooling system |
| PFHX | Plate-Fin Heat Exchanger |
| RQ | Research Question |
| TMS | Thermal Management System |
| TOS | Translation of Shapes |
| VCC | Vapour Compression Cycle |
| $\mu$HX | Microtube Heat Exchanger |

## Symbols

| Symbol | Definition | Unit |
|---|---|---|
| $A$ | Area | [m$^2$] |
| $A_{HX,fr}$ | Frontal area of HX; either air side or refrigerant side | [m$^2$] |
| $A_{ht}$ | Heat transfer area | [m$^2$] |
| $A_{pass}$ | Cross-sectional area of single HX passage | [m$^2$] |
| $A_{tot,pass}$ | Total cross-sectional passage area of HX; either air side or refrigerant side | [m$^2$] |
| $A_{max}$ | Maximum projected frontal area of the duct cowling | [m$^2$] |
| $A_{wet}$ | Wetted Area | [m$^2$] |
| $A_0$,$A_1$,$A_2$,$A_3$,$A_4$ | Areas of the duct stations | [m$^2$] |
| $AR$ | Area ratio of the diffuser; $A_2/A_1$ | [-] |
| $AS$ | Aspect ratio; $w/h$ | [-] |
| $B_D$ | Heat exchanger core depth | [m] |
| $B_H$ | Heat exchanger core height | [m] |
| $B_W$ | Heat exchanger core width | [m] |
| $B_1$ | Inlet blockage | [-] |
| $b$ | Burial depth of the heat exchanger | [m] |
| $C_D$ | Drag coefficient | [-] |
| $C_{D,press}$ | Pressure drag coefficient | [-] |
| $C_f$ | Friction coefficient | [-] |
| $C_{min}$, $C_{max}$ | Minimum and maximum heat capacity rate | [W/K] |
| $C_p$ | Pressure coefficient | [-] |
| $C_p^*$ | Diffuser pressure coefficient | [-] |
| $c_p$ | Specific heat at constant pressure | [J/kgK] |

| Symbol | Definition | Unit |
|---|---|---|
| $D_{cool}$ | Cooling drag | [N] |
| $D_{ext}$ | External cooling drag | [N] |
| $D_{int}$ | Internal cooling drag | [N] |
| $D_{press}$ | Pressure drag | [N] |
| $D_{visc}$ | Viscous drag | [N] |
| $D_h$ | Hydraulic diameter | [m] |
| $F_h$, $F_p$ | Fin height and pitch in FTHX model | [m] |
| $f$ | Fanning friction factor | [-] |
| $f_A$ | Area ratio factor; $A_{wet}/A_{max}$ | [-] |
| $f_D$ | Darcy friction factor | [-] |
| $f_{spill}$ | Spillage sensitivity factor used in the surrogate external drag model | [-] |
| $f_1$, $f_2$, $f_3$, $f_4$ | Design sensitivity factors used in the surrogate external drag model | [-] |
| $G$ | Mass momentum | [kg/m$^2$s] |
| $h$ | Height or heat transfer coefficient | [m] or [W/m$^2$K] |
| $h_{cr}$ | Cruise altitude | [ft] |
| $h_{lip}$ | Diverter height; defined as the distance between wall and lower inlet lip | [m] |
| $h_{max}$ | Maximum protrusion height of duct cowling | [m] |
| $j$ | Colburn heat transfer factor | [-] |
| $K_c$ | Contraction loss factor | [-] |
| $K_e$ | Expansion loss factor | [-] |
| $K_\theta$ | Tilt factor | [-] |
| $k$ | Thermal conductivity | [W/mK] |
| $k_U$ | Utilization coefficient | [-] |
| $L_a$, $L_p$, $L_h$ | Louver angle, pitch and height in FTHX model | [°], [m] and [m] |
| $L_{diff}$ | Diffuser length | [m] |
| $L_{duct}$ | Duct length | [m] |
| $L_f$ | Duct forebody length | [m] |
| $L_{noz}$ | Nozzle length | [m] |
| $l_f$ | Fin length | [m] |
| $l_{lip}$ | Inlet lip length | [m] |
| $\ell_s$ | Fin strip length in PFHX | [m] |
| $M$ | Mach number | [-] |
| $m'$ | Fin efficiency parameter for FTHX | [-] |
| $m\ell$ | Fin efficiency parameter for PFHX | [-] |
| $\dot{m}$ | Mass flow rate | [kg/s] |
| $NTU$ | Number of transfer units | [-] |
| $Nu$ | Nusselt number | [-] |
| $n_f$ | Nr. of fins in the heat exchanger for a given stream | [-] |
| $n_{HX}$ | Nr. of heat exchangers over which the heat load is distributed | [-] |
| $n_{pass}$, $n_{layers}$ | Nr. of flow passage layers; either air side or refrigerant side | [-] |
| $n_{strips}$ | Nr. of fin strips per layer for a given stream | [-] |
| $n_{tubes}$ | Nr. of tubes for refrigerant in FTHX | [-] |
| $P$ | Electrical power output | [W] |
| $P_{tube}$ | Tube inner perimeter | [m] |
| $Pr$ | Prandtl number | [-] |
| $p$ | Pressure | [Pa] |
| $p_f$ | Fin pitch for PFHX | [m] |
| $p_i$ | Inlet pressure | [Pa] |
| $p_t$ | Total pressure | [Pa] |

| Symbol | Definition | Unit |
|---|---|---|
| $\dot{Q}$ | Heat transfer rate | [W] |
| $q$ | Dynamic pressure | [Pa] |
| $q_\infty$ | Free-stream dynamic pressure | [Pa] |
| $R$ | Specific gas constant | [J/kgK] |
| $R_{tube}$ | Outer tube edge radius | [m] |
| $Re$ | Reynolds number | [-] |
| $T$ | Temperature | [K] or [°C] |
| $T_i$ | Inlet temperature | [K] or [°C] |
| $T_{off}$ | Atmospheric temperature offset | [K] or [°C] |
| $t_f$, $t_{fin}$ | Fin material thickness | [m] |
| $t_{lip}$ | Lip thickness | [m] |
| $UA$ | Combined heat exchanger heat transfer coefficient and reference area | [W/K] |
| $u$ | Flow velocity through heat exchanger core | [m/s] |
| $u_*$ | Friction velocity | [m/s] |
| $V$ | Velocity | [m/s] |
| $V_\infty$ | Free-stream velocity | [m/s] |
| $w$ | Width | [m] |
| $y_m$ | Width margin of the duct cowling with respect to the heat exchanger | [m] |
| $z_m$ | Height margin of the duct cowling with respect to the heat exchanger | [m] |
| $\alpha$ | Ramp angle | [°] |
| $\epsilon$ | Heat exchanger effectiveness | [-] |
| $\eta$ | Isentropic efficiency | [-] |
| $\eta_{FC}$ | Fuel cell efficiency | [-] |
| $\eta_f$ | Fin efficiency parameter for straight fins | [-] |
| $\eta_o$ | Fin efficiency parameter | [-] |
| $\theta$ | Flow-relative inclination of the heat exchanger | [°] |
| $\theta_{geom}$ | Geometric inclination of the heat exchanger | [°] |
| $\mu$ | Dynamic viscosity | [kg/ms] |
| $\nu$ | Kinematic viscosity | [$m^2$/s] |
| $\rho$ | Density | [kg/$m^3$] |
| $\sigma$ | Ratio of free flow area to frontal area of heat exchanger for a given stream; $A_{tot,pass}/A_{fr}$ | [-] |
| $\tau_w$ | Wall shear stress | [Pa] |
| $\phi$ | Diffuser mid-line angle | [°] |

# 1

# Introduction

Recent developments in the aerospace sector show a clear interest of established conglomerates as well as emerging players to develop aircraft with electric powertrains. The energy for these systems can be stored directly in electric batteries or in hydrogen, which is carried on-board and from which electricity is gained in a fuel-cell. Besides the weight penalty that is incurred by either system, the fuel-cells, batteries and other power electronics generate large amounts of heat, which need to be dissipated to avoid premature degradation of components or in the worst case, catastrophic failure by, for instance thermal runaway of batteries. While turbofans and turboprops also carry systems which may require thermal management, the scale at which heat needs to be actively rejected on electric aircraft is gravely different, as the engines on traditional aircraft naturally reject heat through their exhaust.
Therefore, future aircraft require the installation of heat exchangers, using the ambient air in flight as a terminal heat sink. Of course, this process is expected to cause aerodynamic drag, as the heat exchanger presents an obstacle for the cooling air and the ducting surrounding the installation increases the parasitic drag of the airframe. Having the right tools to both estimate the cooling drag as well as to optimize the installation of a ducted ram-air heat exchanger can bring great value to engineers, as initial assessments on cooling drag can influence design choices down the line.

A leading company in the field of electric aviation is *Pipistrel*, famous for developing and selling the first certified fully-electric aircraft, the Velis Electro. The research and development department of *Pipistrel*, *Pipistrel Vertical Solutions* or PVS, conducts research on how to better assess the performance of battery-electric and hydrogen fuel-cell aircraft and therefore has proposed *"Cooling Drag Estimation for Ducted Ram-Air Heat Exchangers"* as a thesis topic for the student. Hence, the thesis took place in strong collaboration with *Pipistrel Vertical Solutions* and under the guidance of Jernej Pirnar, who is an aerothermal researcher at PVS.

The thesis structure is kept simple. A literature review in chapter 2 introduces the reader to the subject of thermal management, focusing on the role of heat exchangers in thermal management systems and their possible integration on-board aircraft. Furthermore, an overview of existing cooling drag estimation models is compiled upon which a research objective along with research questions and a strategy to tackle those is presented. Chapter 3 presents the methodology generated by the thesis student to assess cooling drag from an early stage of the aircraft design process. Part of this is a python tool which assesses the internal drag of the ducted ram-air heat exchanger installation. A simple method to generate conformal duct cowlings is devised, leading to a tangible representation of the HX installations and the possibility to assess external drag in a CFD simulation or a surrogate model.
A set of results that help answer the research questions is revealed in chapter 4 through the use of an optimizer and a thorough sensitivity analysis of the tools. The different parts of the tools are validated and verified in chapter 5, providing a critical assessment of the results and points for improvement. Chapter 6 draws the main conclusions of this work. One-by-one the research questions are answered before finally assessing if the research objective of the thesis has been fulfilled. At last, the work is rounded off in chapter 7 by recommending further developments to improve and extend the generated tools as well as additional research work in the field.

# 2

# Literature Review

This chapter first introduces the reader to thermal management systems (TMS) by presenting the working principle of two types of circulating cooling systems, a liquid-based cooling system and a pumped-two-phase cooling system. Thereafter, in section 2.2 and section 2.3 the role of heat exchangers (HX) in TMS is elaborated more precisely and three varieties of aerospace application heat exchangers are presented. Various concepts to integrate HX on board aircraft are discussed in section 2.4 to give the reader an idea of possible solutions. A preview of the drag analysis is provided in section 2.5 where the cooling drag is broken down into its various contributions and an overview of existing cooling drag models found in literature is compiled in section 2.6. The research objective, the research questions and the planned research activities round off this chapter before the chosen methodology is presented in chapter 3.

## 2.1. A Brief Introduction to TMS

The relevance of effective thermal management in electric propulsion systems for aircraft can hardly be overstated. Both battery-electric and hydrogen-fuel-cell aircraft carry components that generate large amounts of heat while at the same time having a limited range of temperatures within which they should operate to prevent premature degradation or even failure (e.g. thermal runaway in batteries). Unlike in traditional aircraft power-plants, such as turbojets and turboprops, the heat generated in these novel propulsion systems, mentioned above, is not expelled through the exhaust and would accumulate to significantly raise the temperature of components, unless actively dissipated through a dedicated system. This section serves as an introduction to commonly found Thermal Management System (TMS) architectures and to the design of aerospace heat exchangers and their integration in aircraft designs.

Nearly all TMS are based on the principle of rejecting the generated heat into the ambient. Thereby the heat balance struck in Equation 2.1 where the generated heat equals the rejected heat must be maintained to keep the component temperature level. For a hydrogen fuel cell (FC), the efficiency of electricity generation is around 52% [1]. Given that fact, a nearly equal amount of waste heat is generated for each required unit of electric power. As will be seen later on in section 2.4, the FC power outputs of hydrogen FC aircraft concepts range from 600 kW to 5 MW. Hence, a considerable amount of waste heat is expected.

$$\dot{Q}_{gen} = \dot{Q}_{rej}, [W] \tag{2.1}$$

There are systems where thermal mass is introduced in the form of phase change materials (PCM) or the tanked fuel (mostly for hybrid-electric aircraft) and used as an, at least temporary, heat sink. An increase in thermal mass slows down the increase in component temperature, allowing for undersizing the TMS. Being a passive solution, it does however not provide the needed operational flexibility as a stand alone TMS.

For aircraft using liquefied hydrogen as their fuel, part of the heat generated in the electric components can be used to condition the hydrogen before it enters the fuel cell.

### 2.1.1. Liquid Cooling Systems

Liquid cooling is a technology that is already widely used for cooling batteries in electric cars and chips in data centers. Liquid cooling systems (LCS) work by having a fluid circulate between the heat source and the heat exchanger, thereby transferring the heat from the source to the sink. The most rudimentary liquid cooling systems have 4 main components: 1. A thermal interface between the liquid and the heat source (often in the form of a cold plate), 2. a pump that drives the fluid through the circuit, 3. a radiator that dumps the heat into the ambient by using ram-air and 4. the connecting pipes and hoses. Figure 2.1 shows the diagram of a simple LCS with the components listed above. A coolant which is commonly found in LCS is a mixture of water and ethylene-glycol. The circulating coolant tends to be pressurized, as this allows the saturation temperature to be increased, and thus offers some operational margin.

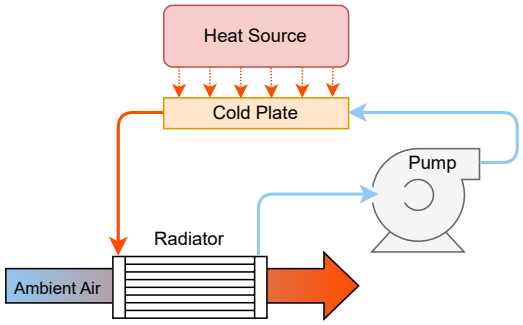


**Figure 2.1:** A diagram for a simple LCS

Due to it's comparative simplicity, a LCS such as in Figure 2.1 is more reliable and easily designed than other TMS. However, it also suffers from a lack in operational flexibility, especially owed to the fact that the heat rejection rate in the radiator is largely dictated by the ambient temperature. For batteries, which have their upper temperature limit around $40°C$, this can mean that on a hot day, the TMS does not dissipate any or insufficient heat for operation.
If that is the case, the liquid circuit can be coupled to a vapour compression cycle (VCC) which has good cooling capabilities even at higher ambient temperatures, as it exploits the saturation temperature gap of a refrigerant at various pressures. One way to implement the VCC is pictured in Figure 2.2, where the heat is transferred to the VCC via the plate heat exchanger (HX) and then rejected to the ambient solely through the VCC condenser.

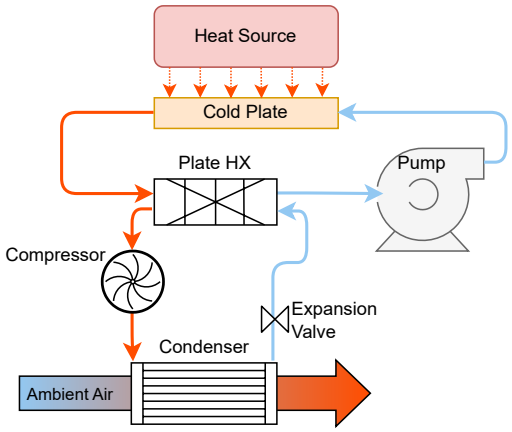


**Figure 2.2:** The diagram showing a LCS coupled to a VCC

### 2.1.2. Pumped 2-Phase Cooling Systems

While LCS already show good cooling performance compared to direct air cooling regarding the amount of heat that can be dissipated, the fact that the temperature of the liquid changes along the channels of the cold plate leads to an uneven temperature gap between the liquid and the heat source and thus the cold plate. As the rate of heat transfer is proportional to the temperature gap between the refrigerant and the cold plate (Equation 2.2), a temperature gradient along the heat source becomes apparent.

$$\dot{Q} = h \cdot A \cdot (T_{cp} - T_{ref}) \tag{2.2}$$

Pumped 2-phase cooling systems (P2P) exploit the latent heat that specialized refrigerants have to maintain a constant temperature gap between the refrigerant and the component. There are two main advantages of this: 1. A promise of better cooling quality through a more constant heat rejection along the cold plate channels and 2. A lower demand for pumping power, since the fluid is allowed to circulate at lower mass flow rates than in an LCS. Simultaneously, P2P are more complex than LCS, as they require accumulator tanks to allow for the refrigerant to expand, as it evaporates, and need to be carefully tuned to prevent dry spots along the cooling channels or leakage of potentially harmful refrigerants. Typical refrigerants in P2P TMS and VCC are R134A and R1233zd.

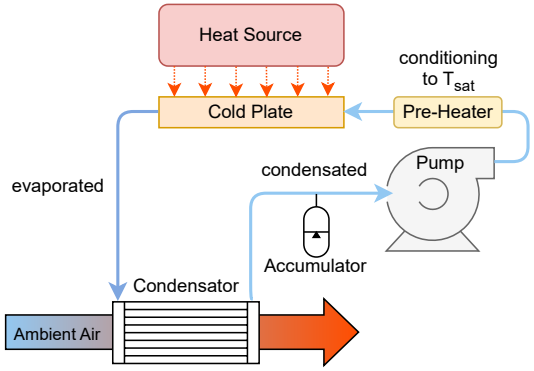


**Figure 2.3:** A simple P2P, analogous to the LCS from Figure 2.1

Figure 2.3 shows a P2P, analogous to the LCS shown in Figure 2.1 where the evaporated refrigerant is condensated in a condensator instead of being cooled down in a radiator, although both these parts are very similar. Moreover, an accumulator tank is added to allow the fluid to freely expand and a pre-heater precedes the cold plate, to ensure that the refrigerant is near saturation.
The P2P pictured in Figure 2.3 suffers from the same limitations as the LCS in Figure 2.1, as it can only provide cooling to components, as long as the ambient is colder than the heat source. Nevertheless, by coupling the P2P to a VCC, similarly to what was done in Figure 2.2, the P2P can be made more operationally flexible.

## 2.2. Role of HX in TMS

The working principles of the two TMS types that may be considered throughout the thesis are presented in section 2.1. The commonality of these TMS, that shall become the focus of this work, is the heat exchanger (HX), either a radiator or a condenser, which rejects the heat taken up within the refrigerant circuit to the ambient. Heat exchangers have a large impact on TMS design and integration as they add weight, are rather bulky and require a supply of ambient air, which generates drag and brings up the need for ducting. While the HX mass and volume are easily estimated through proven sizing methods, the drag contributions made by HX are more difficult to quantify and stem from a variety of sources, both internal (ducting loss and pressure drop through HX) and external (wetted area friction drag and pressure drag due to separation).
The output of aerospace research in TMS for (hybrid-) electric and hydrogen fuel cell aircraft and the

particular issue of cooling drag estimation has recently gained momentum. Still, the models used for cooling drag estimation use different concepts and yield sometimes widely diverging results. An overview is provided in section 2.6. This leads to the problematic issue that cooling drag estimates at early design stages have a very high uncertainty and can lead to aircraft designers making misguided decisions down the line.
Notably, methods that successfully combine the internal and external contributions to drag are hardly found in open literature. Moreover, they barely provide flexibility regarding the impact that changing HX dimensions have on the drag or guidelines on how to best integrate a large HX within the overall aircraft design. In that light, research question 1 can already be formulated.

**Research Question 1**

How does one best integrate HX into an aircraft to ensure good TMS operation and minimal burden on aircraft performance?

A preliminary discussion on approaches to research question 1 (RQ) can be found in section 2.4. Prior to that, section 2.3 looks at the different types of HX that come into question for the remainder of this work.

## 2.3. Choice of HX

In an abstract sense, the variety of HX that exist is infinite, as any device that transfers heat from the refrigerant circuit to the ambient acts as a HX. Nevertheless, accounting for performance, there are only a handful of HX types that can truly be considered viable for aerospace applications and even more specifically, to act as ducted ram-air HX that are part of a TMS. Sundén [2] mentions two design requirements to account for when choosing a thermal management HX:

- **Compactness and lightweight**: The HX should be space efficient and use light materials, such as aluminium alloys.
- **High effectiveness and minimum pressure loss**: The HX surfaces and flow paths should maximize the ratio between thermal conductance and pressure losses. This counts for both streams passing though the HX.

For the expected coolant flow rates of a TMS on a (hybrid-) electric or hydrogen fuel-cell aircraft, one is realistically only given the choice between 3 types of HX. Plate-fin HX (PFHX), flat tube finned HX (FTHX), and microtube HX ($\mu$HX). Each of these HX types are discussed in further detail in their dedicated section below.
Upfront, the PFHX and FTHX are most promising to be used in the subsequent works, as sizing methods are mature and well proven models and experimental data to determine pressure losses and heat transfer are available. The definitive choice between the two remains open and the developed methodology shall be kept flexible enough to perform analyses of both HX types.

### 2.3.1. Plate-Fin HX

Plate-fin HX (PFHX) are a type of heat exchanger commonly made of aluminum, where layers of the heat exchanging fluid streams (refrigerant and air) are sandwiched and separated by plates. Within these layers, flow channels are provided by folded plates that enhance heat transfer between the fluids. Figure 2.4 shows a common kind of cross flow PFHX with a triangular strip fin structure. Figure 2.5, next to it, presents a variety of fin-types which can moreover be incorporated to enhance fluid mixing and thereby heat transfer.

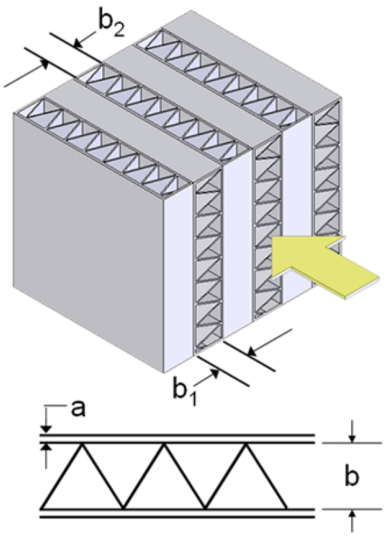


**Figure 2.4:** A crossflow PFHX. Illustration taken from [3].

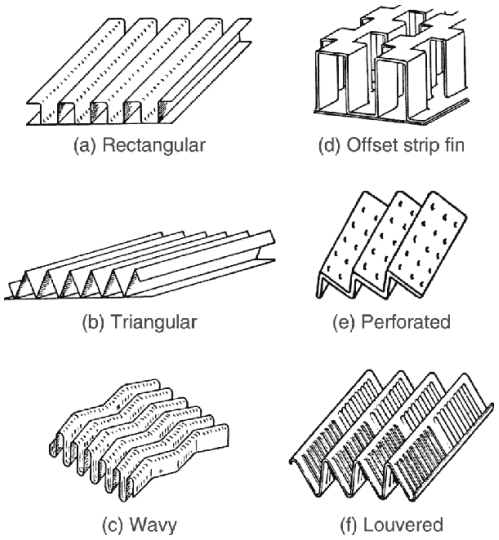


**Figure 2.5:** Different fin-types. Illustration taken from [4].

According to research by Hao [5], the typical range for channel heights of offset strip fin PFHX is between 2-3 mm whereas the fin pitch can be 1.5-5 mm. Fins typically have a thickness of 0.15-0.2 mm and separating plate thicknesses of 0.5 mm and above are common.

### 2.3.2. Flat Tube HX

Flat tube finned HX (FTHX) are very similar to the PFHX and essentially share the same key characteristics regarding flow interactions and the heat transfer mechanisms, as well as materials. However, the key difference lies in the proportional dimensions of the air side passages compared to the fluid passages. Figure 2.6 shows the parts that make up a FTHX. Meanwhile, Figure 2.7 gives a more detailed look at the flow passage cross section of a FTHX with louvered fins. The louvers promote mixing of the air, enhancing the heat transfer properties.

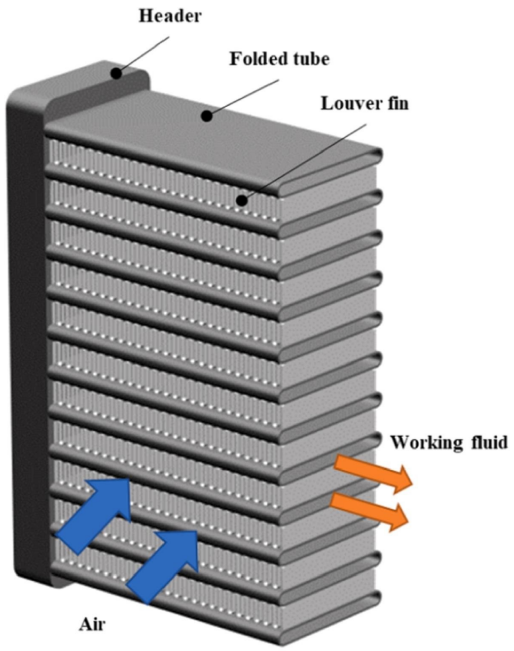


**Figure 2.6:** A side-cut view of a common FTHX. Illustration taken from [6].

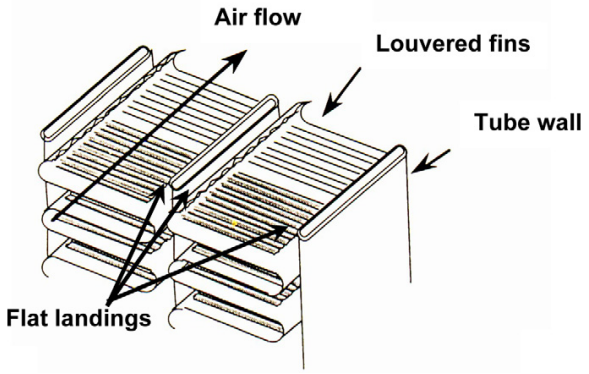


**Figure 2.7:** A cross section of the flow passages of a louvered fin FTHX. Illustration taken from [7].

### 2.3.3. $\mu$HX

Microtube HX ($\mu$HX) have recently gained traction in the world of aviation. The promise of a radical increase in the volumetric and gravimetric heat dissipation density could gravely reduce the impact that TMS have on aircraft design and performance. This is achieved by tremendously increasing the heat exchange surface by conducting the refrigerant through fine tubes, which have a diameter in the range of micrometers [$\mu$m] (which is why they are referred to as $\mu$HX). However, the difficult manufacturing techniques involved in producing this type of HX leads to only few suppliers on the market and a relatively unproven level of technology readiness.
Two companies that develop and manufacture $\mu HX$ for aerospace applications are/were *Intergalactic* and *Reaction Engines*, whose products are displayed in Figure 2.8 and Figure 2.9, respectively.

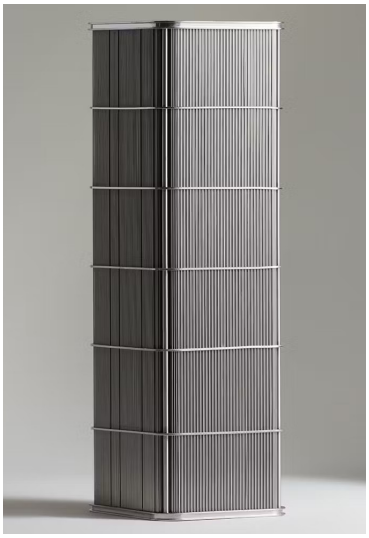

**Figure 2.8:** A straight channel microtube HX from *Intergalactic*

**Figure 2.9:** A curved channel microtube HX from *Reaction Engines*

At this point it is important to note that any significant advancement in thermal management and thereby the entirety of the shift to less polluting aircraft propulsion is highly dependent on the employment of such advanced HX tech onboard aircraft. Simultaneously, one should not rely on the implementation of $\mu$HX in the TMS, since it could delay the entry into service of aircraft, if the technology proves difficult to integrate.

## 2.4. Integration into Aircraft Design

The integration of the TMS into overall aircraft design is quite flexible and case dependant. Nevertheless, a few things should be considered to arrive at a harmonious and streamlined design.

- **Source-Sink proximity:** keeping the heat source, like the power electronic, and heat sink, in this case the HX, closeby reduces the piping length. Otherwise, pressure drops within the coolant loop rise with tube length which calls for a pump with more power, thereby increasing power consumption and mass. Moreover, more piping implies that more coolant volume is within the system, which also raises the TMS mass.
- **Space for piping and ducting:** When designing the TMS, compactness should be kept in mind. Yet, the need to connect components through piping and to supply air (either for a HX or a Fuel-cell) should be remembered at all stages of the design. Specifically, in the case of this work, it translates to accounting for the coolant supply into and out of the HX as well as the ducting through which ram-air is guided from the air inlet to the HX and rejected through the air outlet.
- **Maintainability:** While striving for an easily maintainable TMS, which may also allow for the removal of fuel cells and batteries for inspection or replacement, is positive, it should not necessarily be the focus of the design. The same goes for the integration of the HX. Accessibility for inspection, for instance to detect foreign object debris ingestion (FOD), is desirable but not the main target of the design philosophy.

The general setup of a ducted ram-air HX, is depicted in Figure 2.10. It furthermore includes the presence of a puller fan, aft of the HX, which can generate an airstream through the duct if the ambient airspeed is insufficient when standing or taxiing.

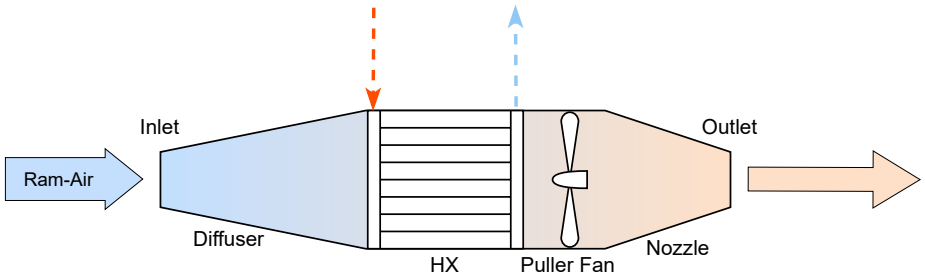


**Figure 2.10:** A general diagram showing a ducted ram-air heat exchanger.

The placement of this duct and the HX can in principle be freely chosen, but a few examples from existing hydrogen FC aircraft concepts are presented in the subsections below. Moreover, a few considerations and guidelines for HX installation are presented in Küchemann's book on the aerodynamics of propulsion [8].

### 2.4.1. Unifier19

The Distributed Electric Propulsion (DEP) concept of Unifier19 [1] envisions the heat exchanger of the LCS for the Fuel-Cell system to be placed in the top section of the wing. There are two duct inlets, at each junction of the shouldered wing with the fuselage which merge towards a single outlet at the top of the fuselage. In Figure 2.11, the inlet and outlet areas are colored in black and best visible in the front and side view, respectively. The FC stack is intended to output around 600 kW of electric power.

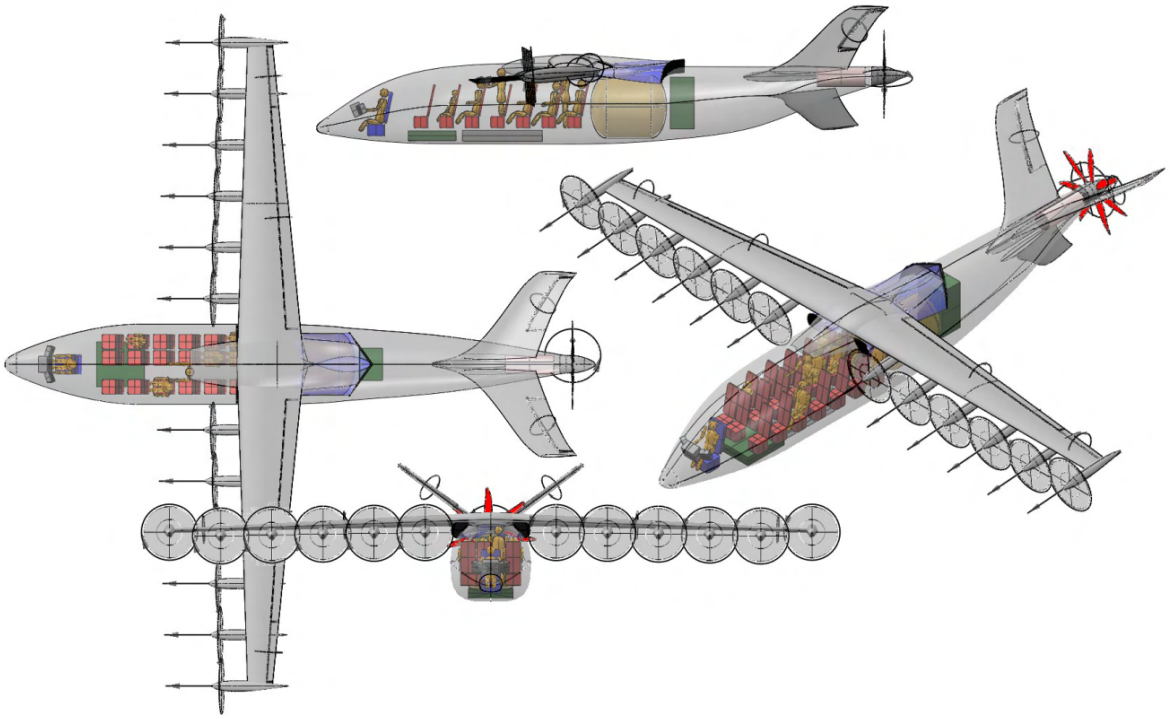

**Figure 2.11:** The Unifier19 concept proposes the installation of the ducted ram-air heat exchanger on the top of the fuselage. Image taken from [1].

### 2.4.2. Universal Hydrogen

Universal Hydrogen was a company, aiming to retrofit turboprop aircraft to be hydrogen fuel-cell compatible. The main HX is split in 2 and mounted to each side of the engine nacelle. Figure 2.12a shows, the cowling that envelopes the HX while Figure 2.12b shows the same installation bare. Two things are very noteworthy: 1. the HX is highly tilted, which increases the pressure drop that the air experiences through the HX and 2. piecing together the inlet area, the cowling shape and the HX tilted height, the internal duct seems to maintain a very constant flow area throughout, with little diffusion taking place. The FC stack is intended to output 800 kW of power, powering only one of the two engines.


**(a)** Cowled HX. Image taken from [9].

**(b)** Stripped HX. Universal Hydrogen via Twitter [10].

**Figure 2.12:** The HX installation on Universal Hydrogen's modified De Havilland Canada Dash-8

### 2.4.3. ZeroAvia

ZeroAvia follows an approach to developing a hydrogen FC aircraft much like Universal Hydrogen, where existing aircraft are retrofitted instead of coming up with a clean sheet design. Figure 2.13a shows the testbed aircraft that ZeroAvia uses to test their propulsion system where one engine runs on a conventional turboprop and the other engine is powered electrically, with a 600 kW FC stack as the power source. The concept pictured in Figure 2.13b is meant to be powered by a modular 2-5 MW system, hence a much larger output than seen in other examples.


**(a)** The retrofitted Dornier-228 that ZeroAvia operates. Encircled is the air inlet, presumably used for FC air supply and cooling.

**(b)** ZeroAvia's concept for a retrofitted ATR-72. The FC stack and TMS are located in the nacelle of the engine.

**Figure 2.13:** Two concepts from the ZeroAvia family. Images taken from [11].

### 2.4.4. Project Newborn

Project Newborn aims to develop an LH2 FC propulsion system on the 1 MW scale. The rendering in Figure 2.14 shows the system arrangement with the FC stack, in turquoise, right aft of the cabin. The TMS would be located in the vicinity of it, with fuselage-bound HX. The batteries for intermediate power management and storage are located next to the engines.

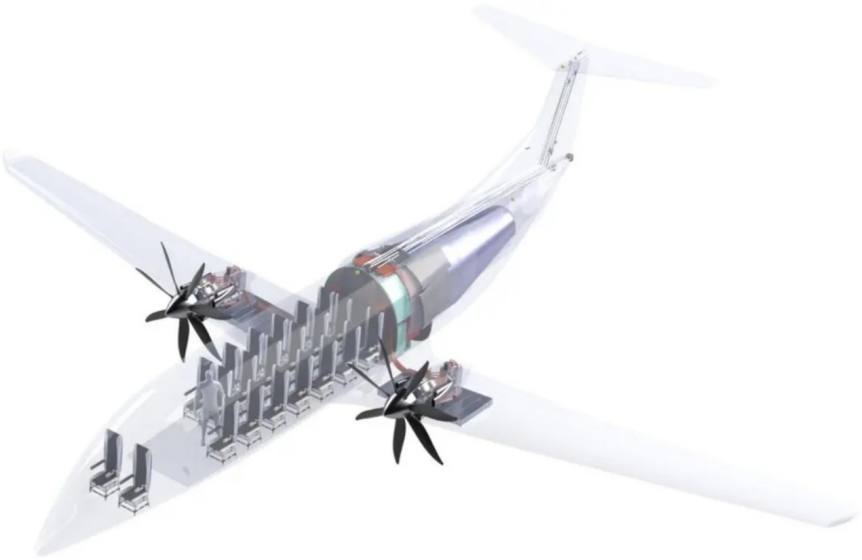

**Figure 2.14:** The concept of Project Newborn, with the FC stack and TMS installed behind the cabin. Image taken from [12].

### 2.4.5. H2Fly

There is not a lot of valuable information present regarding the power output of the system that H2Fly envisions to implement on their concept aircraft depicted in Figure 2.15. However, due to the size of the aircraft, it is presumably in the range of multiple MW, similar to Figure 2.13b. The large size of the intakes at the aircraft belly serves as a great indicator of how important TMS design and therefore also TMS performance and the resulting cooling drag is for LH2 aircraft.


**Figure 2.15:** The H2Fly concept with very noticeable belly-intakes, presumably for FC cooling. Image taken from [13].

## 2.5. Cooling Drag Accounting

In order to successfully quantify the drag that arises from cooling, the various sources should be understood and accounted for properly. In general, the drag can be divided into 2 types; the internal and the external drag. There are various sources that contribute to drag, however, which will be discussed one-by-one in this chapter in subsection 2.5.1 and subsection 2.5.2. Finally, section 2.6 aims to compile a comprehensive overview of the cooling drag models that are found in scientific literature.

As can be seen in the schematic representation in Figure 2.16, the captured air passes through a diverging diffuser section before passing the HX, followed by a contracting nozzle. The diffuser helps slow down the air, which reduces pressure losses in the HX, and builds up additional static pressure that acts counter to the pressure loss in the HX. The subsequent nozzle re-accelerates the flow to build up momentum and reduce drag and lowers the static pressure back to the ambient pressure. Under the right conditions, this functions as a sort of Brayton cycle, without the turbine driven compressor, and generates thrust from the waste heat.

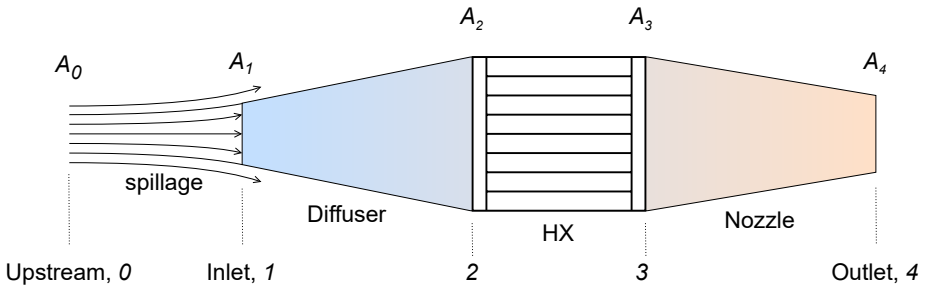


**Figure 2.16:** The ducted ram-air HX with defined stations

### 2.5.1. Internal Drag

Internal drag arises due to the change in momentum that the mass of air flowing through the duct and crossing the HX experiences. The internal drag can be classified into 3 kinds according to Meredith [14]. Skin friction drag, pressure drag due to separation from a surface and drag due to expansion losses not accounting for separation. It is generally expressed by the momentum loss equation in Equation 2.3.

$$D_{int} = \dot{m}_1 \cdot (V_0 - V_4) \tag{2.3}$$

The local convention from the schematic representation found in Figure 2.16 should prevail to denote the relevant stations in the model. In this model, the mass flow of air from the inlet to the outlet (1-4) remains constant but due to spillage at the inlet, the ratio of $\dot{m}_0$ to $\dot{m}_1$ is defined according to Equation 2.4, where $A_1$ is the inlet area and $A_0$ is the area of the captured streamtube upstream. Figure 2.17 visualizes these definitions once more.

$$\frac{\dot{m}_0}{\dot{m}_1} = \frac{A_0}{A_1} \tag{2.4}$$

When spillage occurs, a forward acting lip suction force is present, which offsets some of the cowling drag. Figure 2.16 shows the spillage as the air that is not captured by the inlet, despite being within the projected surface of the inlet upstream. Instead, as the inlet is running at reduced mass flow, some air is said to spill to the sides, such that the streamtube captured by the inlet is in fact contracting as one goes upstream. Hence, with the notation defined in Figure 2.16, the area ratio $A_0/A_1$ is smaller than unity. Under the condition that the area ratio $A_0/A_1$ is equal to unity, the inlet is said to run full and no spillage is observed.
The lip suction force is visualized in Figure 2.17 and offsets some of the pre-entry intake drag. The spillage rate is determined by a pressure feedback loop from the outlet to the inlet which is explained in subsection 3.3.4.

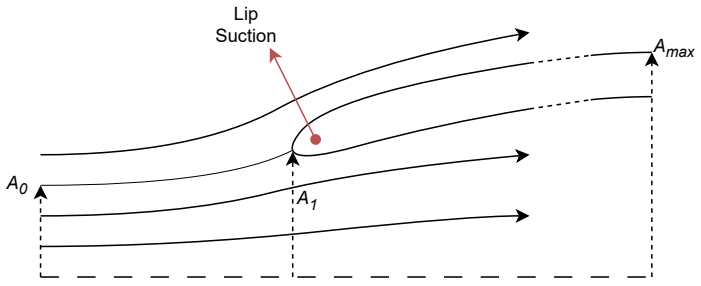


**Figure 2.17:** Lip suction force that occurs on a spilling intake. Reproduced from [15].

In the diffuser, drag is caused by the friction between the boundary layer (BL) and the internal surface area of the diffuser, and expansion losses. Moreover, in ducts where the expansion occurs too abruptly,

the presence of pressure drag due to internal separation of the ram-air leads to excessive additional drag and can cause the HX to receive an inconsistent supply of air. In a final design, diffusers need to be carefully designed such that flow separation is avoided. Simultaneously, designers need to keep in mind that a more gradual expansion by means of a longer diffuser leads to more friction drag.[14] Effectively, an optimal middle ground must be struck.
According to Küchemann [8], a so-called streamlined diffuser represents the most efficient solution for a straight two-dimensional diffuser. The trumpet-shape streamline diffuser is plotted in Figure 2.18 next to a commonly found sine-shaped diffuser. From experimental results included in [8], it is found that the streamline diffuser has a much better pressure recovery than a normal diffuser and an oblique HX diffuser.

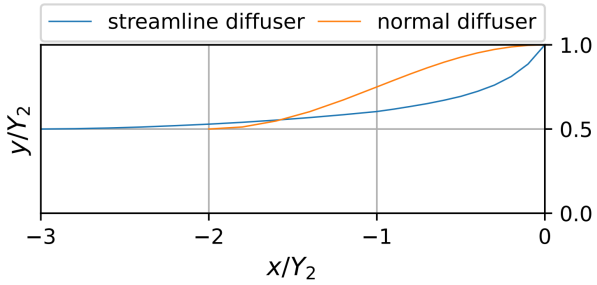


**Figure 2.18:** Single wall of axi-symmetric streamlined and normal diffuser with the same expansion ratio. X-axis represents line of symmetry. (Reproduced from Küchemann.[8])

While an optimized diffuser may be relevant for more mature design work in the field, assuming a rectilinear or conical diffuser shape at this stage would be a more conservative choice. Luckily, pressure recovery models and design guidelines for such diffusers are widespread in literature and therefore easily implementable in any parametrized model. Pittaluga's [16] work on pressure recovery correlations presents a more flexible version of the correlations first laid out by Sovran and Klomp [17] and can be implemented in an analysis tool.

The HX's role in the drag model is two-fold. Primarily, it represents an obstacle for the air flow, which inevitably leads to pressure losses as the exposed HX surface needed for heat transfer causes friction and channel contractions, as well as louvers or other fin modifications to promote flow mixing cause additional resistance. Moreover, the effective contraction and expansion created by the, for the air impermeable, fluid-side channels cause small scale flow separation.
At the same time, the HX adds heat and thereby energy to the air stream, which can be turned into useful work at the outlet nozzle. Ideally, this can lead to offsetting some of the drag or, if the amount of heat is sufficient and the system well designed, even generate additional thrust. This offsetting of the internal drag is commonly known as the "Meredith effect", named after F.W. Meredith.
For the pressure drop and the heat transfer rate in the HX, a key relation to the flow state (i.e. the Reynolds number $Re$) is worth being aware of. While flow turbulence promotes convective heat transfer by mixing the boundary layer, transition from laminar to turbulent BL also increases the friction coefficient dramatically. This is represented by the friction factor $f$ and the Colburn $j$-factor, which is a measure of the heat transfer.
Küchemann [8] further proves this point by defining the utilization coefficient $k_U$ which relates the heat transfer coefficient $k_H$ to the pressure drop coefficient $k_P$ (as noted in Equation 2.5). A higher $k_U$ indicates that the pressure drop is being used more efficiently for heat transfer. Simultaneously, $k_U$ values for a given heat exchanger system remain roughly constant with $Re$ and only change significantly, when the geometry, roughness or waviness is altered.

$$\frac{k_H}{k_P} = k_U = const. \tag{2.5}$$

As already alluded to in subsection 2.4.2, the HX integrated in the duct may be tilted, in order to reduce the external drag. Naturally, this tilt is expected to have two adverse effects. First and foremost, one

expects the pressure drop to rise significantly. Imagine the flat coolant passages impermeable to the ram-air to act as airfoils, which deflect the flow. At high angles of attack, thus high HX tilt, these airfoils, namely the tubes, experience flow separation, causing a loss of momentum in the air, which translates to a pressure drop. Naturally, this effect is dependent on the shape of the coolant passages as well, where rounded edges are more favorable to avoid edge separation.[8].
The other concern of a tilted HX would be that the tilt leads to a pronounced non-uniformity in the air flow, such that certain coolant passages of the HX don't transfer sufficient heat. Thankfully though, research conducted by Nichols [18] shows that neither of these effects is very concerning up to tilt angles of 70 degrees.

The losses that occur in the nozzle are considered to be very small. This is because the negative pressure gradient means that flow separation is improbable and therefore, unlike in the diffuser, the trade off between pressure drag and internal friction is less delicate. Generally, nozzle losses in a ducted ram-air HX installation are expected to be as low as to become negligible [19]. Isentropic loss values found in literature exist exclusively for turbomachinery nozzles and range from 5% to 2% [20]. However, these engine nozzles operate under very different conditions than a ducted ram-air HX and sometimes include diverging sections promoting losses.
Keep in mind that the nozzle area $A_4$ is key to how much of the cooling drag can be offset. With an ideal nozzle area, the flow can be accelerated such that it produces thrust and, given the heat input of the HX, offsets some of the cooling drag. Since the ideal nozzle area depends on the freestream conditions and the HX heat rejection rate, a variable nozzle geometry would be the best solution and will be considered in this work.

### 2.5.2. External Drag

With all sources of internal drag summed up, external drag shall be treated in this section. The two sources of external drag are pressure drag and friction drag. While friction drag largely scales with the wetted area of the installation, the pressure drag is shape-dependent and caused by flow separation. As indicated in the discussion on diffuser drag, there exists a trade-off between the minimization of friction drag and pressure drag. This is also valid for the external drag of the duct installation. On top of that, the internal and external shape of the duct cannot be considered independent, such that any modifications made on internal components (diffuser, HX, nozzle) translate to a change in the external profile of the installation. So far, current literature seems to have neglected this interaction, perhaps relying on the idea that the installations can be integrated flush into the aircraft fuselage, thereby only incurring minimal external drag from the inlet. Unfortunately, the prospect of the large HX being integrated completely within the fuselage seems unlikely, as other components such as fuel cells, batteries and other power-electronics and TMS components take up space needed for ducting.

One way of quantifying the external drag is found in Hoogerdijk's work [21], and replicated by Niehuis [22], which uses a static drag coefficient for wing mounted nacelles derived by Hoerner [23]. This method is however, as the authors admit, neither perfectly applicable [21] nor do the values carry satisfactory accuracy [23]. Supposing that the model used in [21] reflects a proper order of magnitude, the contribution of external sources to the cooling drag represents about 30 %, thus underlining that it is indeed a significant contributor. Supporting the interest in better modeling the external drag of the installation, is van Dongen's [24] recommendation to put more weight on the analysis of external drag contributions as current methods insufficiently reflect the impact that the external drag has on overall cooling drag.
Given that duct design can take on very specific shapes, it would be advantageous to explore the external drag caused by a ducted ram-air HX installation with a more flexible method than a static drag coefficient, as was done in the presented methods. A thought that comes to mind may be to employ potential flow solvers or even CFD simulations in the determination of external drag. Particularly panel methods can be very promising as they are computationally inexpensive and easier to set up than a complex 3D CFD simulation requiring meshing around the object. Yu's [25] work may provide help in choosing an appropriate low fidelity flow solver. At last, the final selection of the flow solver is discussed in detail in section 3.5.

## 2.6. Cases in Literature

There are a few attempts to quantify cooling drag in literature. The methods used by each source are tabulated below (Table 2.1) and serve as a review of the current state of research in varying complexity. It should be noted that many more models exist in literature which aren't included as they either oversimplify the quantification of cooling drag or appear outright wrong. Also, models listed below have some disadvantages but it should be remembered that a great portion of the studies conducted which include cooling drag estimation models only have developed these as a side-note, in a more wide-scope research on TMS in general. [19, 26, 21]

**Table 2.1:** An overview of selected papers and theses, which lay out their approach to cooling drag quantification for a ducted ram-air HX.

| Authors | Year | Model Description | Notes |
|---|---|---|---|
| Kellermann[27] | 2021 | Momentum loss with semi-empirical correlations for internal drag: Spillage drag from Malan [28], Diffuser model from Pittaluga [16], Nozzle efficiency from Walsh [29] | No external drag model, HX pressure drop is a design-variable in the optimization |
| Habrard[26] | 2023 | Inlet drag from ESDU86002 [30] | Inlet as only contributor to drag, Receives very low values, Has a mass estimation model for inlet from Roskam [31] |
| Hoogerdijk[21] | 2023 | Momentum loss for internal drag: Diffuser and Nozzle modeled with invariable isentropic efficiency, HX pressure drop from Shah [32], External drag coefficient from Hoerner [23] | Only shape dependent source is HX, External drag scales with inlet area, No spillage drag |
| Scoccimarro[19] | 2023 | Inlet drag from ESDU86002 [30], Diffuser model from Sovran [17], HX pressure drop from Manglik [33], Nozzle modeled with isentropic flow relations and no pressure losses | Inlet drag is external drag |
| Collares[34] | 2024 | Momentum loss with semi-empirical correlations for internal drag: Diffuser losses from Katzoff [35], HX pressure drop from Kays [36], Nozzle efficiency from Walsh [29] | No external drag model, No spillage drag included, Assumes ideal nozzle expansion throughout mission |
| van Dongen[24] | 2024 | Inlet drag from ESDU86002 [30] 2D CFD for diffuser and nozzle, HX pressure drop from Shah [32], HX tilt modeled with CFD and Nichols [18] Nozzle efficiency from Mattingly [37] | No external drag model, Recommends working on one |
| Niehuis[22] | 2024 | Momentum loss for internal drag with isentropic flow relations and assumed isentropic efficiencies and HX pressure drop model, Puller fan in nozzle; External drag with fixed drag coefficient | No spillage |

## 2.7. Path for Research Phase

The purpose of this chapter is to state the overall research objective of the thesis work. In connection to that objective, a series of research questions arise, listed in subsection 2.7.1, which are meant to reflect on the knowledge gaps that are present in the current state of research. Lastly, achieving the formulated objective can only happen if certain research activities are carried out. The planned research activities are therefore laid out in subsection 2.7.2.

### 2.7.1. Research Definition

**Research Objective**

*Develop a model/ method which estimates cooling drag for ducted ram-air heat exchangers on a base of influential parameters.*

**Research Question 1**

How does one best integrate a HX into an aircraft to ensure good TMS operation and minimal burden on aircraft performance?

**Research Question 2**

How does cooling drag scale with the ambient temperature and flight conditions?

**Research Question 3**

How do internal and external drag sources scale with each other?

**Research Question 4**

What balance between internal and external drag is the best to improve aircraft performance? (i.e., is an internally streamlined design at the cost of external losses advantageous or vice versa?)

**Research Question 5**

Which type of HX is the most provides the best drag performance? PFHX or FTHX?

**Research Question 6**

What HX shape provides the best drag performance? Thin and wide or thick and compact?

### 2.7.2. Research Activities

The research objective will be achieved using a reference 1 MW FC conceptual 19-seater with fuselage-bound HX as a case to develop a methodology to estimate the cooling drag. For this, three distinct parts of a tool are developed and later combined in an optimization strategy.
First, a method to assess the internal drag based on the momentum deficit of the captured air is developed. This includes two detailed heat transfer and pressure drop models for the FTHX and the PFHX. The external drag is to be determined with an appropriate method that should not be too computationally expensive. If computational expenses are high, a surrogate model should be constructed which interpolates the external drag for a certain duct shape. This also necessitates that the external shapes

of the ducts are modeled in a CAD software, such as *OpenVSP*.
Hence, the three tool parts are the internal drag calculator, the shape transfer function to generate appropriate duct designs, and the determination of the external drag, either through a direct computation or a surrogate model.

As the analysis is carried out, a cooling drag estimation tool-box is generated. The ultimate goal is that the methodology that is developed is fully reproducible and versatile enough to be applied to other aircraft, if desired by a user of the toolbox. Moreover, the lessons learned by assessing the cooling drag of the 1 MW reference case should answer the research questions in a manner that they apply to other aircraft and TMS as well.

# 3

# Methodology

This chapter explains how the research activities were executed. In order to make the findings of this work reproducible and fulfill the main research objective that was formulated in chapter 2 subsection 2.7.1, the majority of the methodology is implemented in a python tool, under the name of **DRAX**, standing for "**D**ucted **R**am-**A**ir heat e**X**changer". The drag model is split up into two parts - internal and external. In order to convert the abstract model from Figure 3.9 used in the internal drag calculation (section 3.3) into a tangible duct cowling used in the external aerodynamic drag analysis (section 3.5), a set of geometric functions and design rules was devised under the umbrella of a dedicated function. This function, called "Translation of Shapes" (**TOS**), is elaborated in section 3.4. The tools can be used individually or combined, either in a single sequential evaluation or in an optimization. The optimization method has been applied in order to answer some of the more nuanced research questions, which is laid out in section 3.6. However, before diving into the drag estimation and design guidelines, the methodology starts by presenting a major part constituting **DRAX** in section 3.1 and section 3.2, that is the HX heat transfer and pressure drop models.

## 3.1. Heat Transfer Models

There are two compact cross-flow HX types implemented in **DRAX**, namely a louvered fin and flat tube HX (FTHX) and a plate fin HX with offset strip fins (PFHX), imaged in Figure 3.2. The advantage of the former is that they are easy to mass produce (which is not necessarily a requirement for aviation) and can easily be manufactured into more adaptive shapes, as illustrated in Figure 3.1. However, the latter can dissipate more heat for the same HX core volume and is therefore, as was already discussed in chapter 2, the conventionally preferred option for aerospace applications [2].

**Figure 3.1:** Example of how finned tube HX can be easily customizable. Image taken from [38]

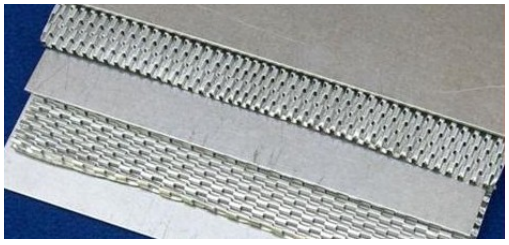

**Figure 3.2:** A cross-cut of an offset strip plate fin HX, as included in **DRAX**. Image taken from [39]

For the heat transfer in both the FTHX and the PFHX, the $\epsilon - NTU$ method is employed. Information on this method can be found in various books. To name some, Incropera et al. [40] and Shah and Sekulić [32] provide well structured overviews of how to apply this method in general.
The heat transfer rate $\dot{Q}$ in the HX is related to the inlet temperature gap between the hot refrigerant and the cold air, the lower heat capacity rate of either stream $C_{min}$ and the effectiveness $\epsilon$ of the HX.

This general relation is noted in Equation 3.1.

$$\dot{Q} = \epsilon \cdot C_{min} \left(T_{ref,i} - T_{air,i}\right) \tag{3.1}$$

$$C_{air} = \dot{m}_{air} c_{p,air} \tag{3.2}$$

$$C_{ref} = \dot{m}_{ref} c_{p,ref} \tag{3.3}$$

$$C_{min} = \min\left(C_{air}, C_{ref}\right) \qquad C_{max} = \max\left(C_{air}, C_{ref}\right)$$

For a single-pass cross-flow HX with unmixed fluids, which applies to both implemented models, $\epsilon$ can be determined with Equation 3.4, as given by Incropera et al.[40].

$$\epsilon = 1 - \exp\left[\left(C_{max}/C_{min}\right) \cdot NTU^{0.22} \cdot \exp\left[-\left(C_{min}/C_{max}\right) \cdot NTU^{0.78}\right] - 1\right] \tag{3.4}$$

The number of transfer units $NTU$ is a dimensionless parameter which can be derived from the inverse of the overall HX heat transfer coefficient and reference area $UA$ and $C_{min}$, as below. In its full form the overall heat transfer coefficient of the HX (see Equation 3.6) consists of five terms. Two being the heat transfer coefficient $h$ and the heat transfer area, as well as a fin efficiency parameter $\eta_o$ of each fluid stream. Two more to account for fouling on each fluid side of the HX, with the fouling factor $R_f^{''}$ and lastly the thermal resistance of the wall represented by $R_w$.
According to Incorpera [40] two assumptions can be made to simplify Equation 3.6 to Equation 3.7. For one, we validly assume that for a well-maintained and new HX, the fouling effects are negligible and, moreover, we can assume that for our HX, a material with large thermal conductivity is used along with very thin walls, making $R_w$ negligible in magnitude. Beyond that, the obvious step can be made to designate air as the cold stream and the refrigerant as the hot stream.

$$NTU = \frac{UA}{C_{min}} \tag{3.5}$$

$$\frac{1}{UA} = \frac{1}{\left(\eta_o h A\right)_c} + \frac{R_{f,c}^{''}}{\left(\eta_o A\right)_c} + R_w + \frac{R_{f,h}^{''}}{\left(\eta_o A\right)_h} + \frac{1}{\left(\eta_o h A\right)_h} \tag{3.6}$$

$$\frac{1}{UA} = \frac{1}{\left(\eta_o h A\right)_{air}} + \frac{1}{\left(\eta_o h A\right)_{ref}} \tag{3.7}$$

The derivation of the remaining terms in Equation 3.7 varies greatly for different types of HX and different types of fins. Therefore, they will be discussed individually for the FTHX and PFHX and their respective streams in the subsequent sections.

### 3.1.1. FTHX Model

The air side properties for the FTHX model, hence the louvered fins, are determined with a model by Dong et al. [41] which provides the Colburn $j-$ and the Fanning $f-$factor for the fins. The variables of Equation 3.8 and Equation 3.38 are, besides the louver-specific $Re$, the design parameters of the fins and louvers, which are illustrated in Figure 3.3 and noted in Table 3.1.

$$j = 0.26712 Re_{L_p}^{-0.1944} \left(\frac{L_a}{90}\right)^{0.257} \left(\frac{F_p}{L_p}\right)^{-0.5177} \left(\frac{F_h}{L_p}\right)^{-1.9045} \left(\frac{L_h}{L_p}\right)^{1.7159} \left(\frac{L_d}{L_p}\right)^{-0.2147} \left(\frac{t_f}{L_p}\right)^{-0.05} \tag{3.8}$$

$$Re_{L_p} = \frac{u L_p}{\nu} \tag{3.9}$$

The louver-specific $Re$, denoted as $Re_{L_p}$, uses the louver pitch $L_p$ as the characteristic length and the air velocity at the louvers $u$. Thus, the effect of blockage of the flat tubes must be taken into account when finding $u$.

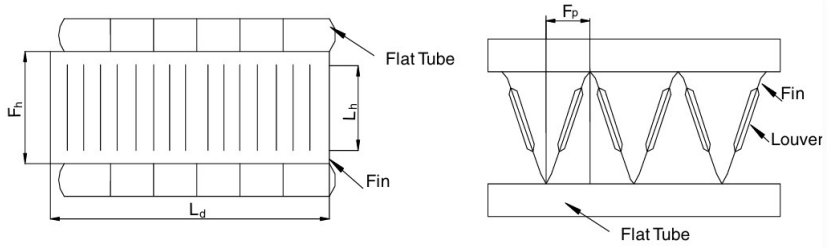


**(a)** Definition of the geometrical parameters for a multi-louvered fin HX.

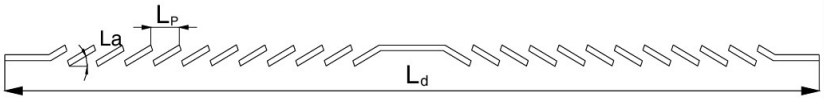


**(b)** Cross section of a multi-louvered fin geometry.

**Figure 3.3:** Fin and louver design parameters. Figures taken from Dong et al. [41]

**Table 3.1:** List of parameters from Dong et al. [41]

| Symbol | Explanation |
|---|---|
| $L_a$ | Louver angle |
| $F_p$ | Fin pitch |
| $L_p$ | Louver pitch |
| $F_h$ | Fin height |
| $L_h$ | Louver height |
| $L_d$ | Louver depth |
| $t_f$ | Fin thickness |

Once $j$ is determined, the air-side heat transfer coefficient $h_{air}$ for Equation 3.7 can be obtained through Equation 3.10. The specific heat at constant pressure $c_{p,air}$ and the Prandtl number $Pr_{air}$ are fluid properties and are obtained in **DRAX** through the CoolProp fluid library for Python [42]. $G$ is the mass momentum of the flow in the passages and is a measure often used in HX analysis. It can be derived from the mass flow as in Equation 3.11 or the maximum flow velocity $u$ and the density $\rho$.

$$h_{air} = j\frac{Gc_{p,air}}{Pr_{air}^{2/3}} \qquad (3.10) \qquad\qquad G_{air} = \frac{\dot{m}_{air}}{A_{tot,air,pass}} = u_{air} \cdot \rho_{air} \qquad (3.11)$$

The wetted heat transfer area on the air side $A_{air,ht}$ can be divided into two parts, the plate area $A_{air,plate}$ and the fin area $A_{air,fin}$. Equation 3.13 and Equation 3.14 show the sub-components of $A_{air,plate}$ and $A_{air,fin}$, respectively. The assumption is made that the top and bottom rows of the HX are fin passages, not tubes.
$B_W$ and $B_D$ are the HX width and depth, which correspond to the tube length and width, respectively. $n_{tubes}$ and $n_{fins}$ are the total number of tubes and the number of fins per row, respectively. Hence, $n_{fins} \cdot (n_{tubes}+1)$ is the total number of fins on the HX, keeping in mind that the definition of a fin follows Figure 3.3a, with the fin pitch $F_p$ delimiting one fin. Note that this definition is not always universally applied in research with some papers defining what is here denoted as $2 \cdot F_p$ as one fin. The fin length $l_f$ can be derived geometrically and is the length of a single fin, as per the definition of the fin pitch $F_p$ in Figure 3.3.

$$A_{air,ht} = A_{air,plate} + A_{air,fin} \qquad (3.12)$$

$$A_{air,plate} = \underbrace{2n_{tubes} \cdot (B_W B_D)}_{\text{top/bottom of tubes}} + \underbrace{2n_{tubes} \cdot (B_W h_{tube})}_{\text{front/back of tubes}} + \underbrace{2\,(n_{tubes}+1) \cdot (B_D F_h)}_{\text{sides of air passage rows (header bars)}} \qquad (3.13)$$

$$A_{air,fin} = 2(\underbrace{B_D l_f}_{\text{fin face}} + \underbrace{t_f l_f}_{\text{fin edge}})n_{fins}(n_{tubes}+1) \qquad (3.14)$$

The last parameter needed for the air side in Equation 3.7 is the total fin surface efficiency $\eta_o$ which is constituted by the fin efficiency for straight fins $\eta_f$ as well as the ratio of the fin heat transfer area $A_{air,fin}$ from Equation 3.14 to the total air side heat transfer area $A_{air,ht}$. The fin efficiency parameter $m'$ uses the heat transfer coefficient from Equation 3.10 along with the thermal conductivity of the fin material $k_f$ and the fin thickness $t_f$.[43]

$$\eta_o = 1 - \frac{A_{air,fin}}{A_{air,ht}}\,(1-\eta_f) \quad (3.15) \qquad \eta_f = \frac{\tanh\,(m' F_h/2)}{(m' F_h/2)} \quad (3.16) \qquad m' = \sqrt{\frac{2h_{air}}{k_f t_f}} \qquad (3.17)$$

The fin efficiency on the refrigerant side is simply set to $\eta_{o,ref} = 1$, as no fins are submerged in the refrigerant stream. The heat transfer area for the refrigerant $A_{ref,ht}$ is calculated by Equation 3.18 under observation of the definitions in Figure 3.4.

$$A_{ref,ht} = \underbrace{n_{tubes} \cdot B_W \left\{2\left[(B_D - 2R_{tube}) + (h_{tube} - 2R_{tube})\right] + 2\pi\left(R_{tube} - t_{tube}\right)\right\}}_{\text{flat tube inside perimeter}} + \underbrace{2\left(F_h B_D\right) \cdot \left(1 + n_{tubes}\right)}_{\text{sides of air passage rows (header bars)}} \tag{3.18}$$

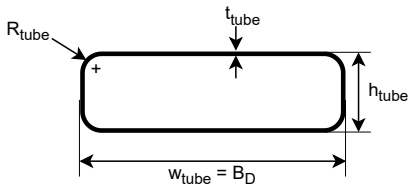


**Figure 3.4:** Definition of the geometrical parameters of a flat tube of the FTHX.

In order to obtain a heat transfer coefficient for the refrigerant side $h_{ref}$, a different method is used than for the air side. Instead of deriving it over the Colburn $j-$factor, $h_{ref}$ is obtained via the Nusselt number $Nu$ as in Equation 3.19, with $k_{ref}$ being the refrigerant specific accessed through CoolProp in **DRAX**. Following the method used by Ng et al. [43], a flow-regime-dependent procedure for $Nu$ is established and summarized in Equation 3.20. The tube-specific Reynolds number $Re_{tube}$ and the tube hydraulic diameter $D_h$ are noted in Equation 3.21 and Equation 3.22, respectively. $A_{ref,pass}$ denotes the flow area per tube for the refrigerant, not the total passage area, while $P_{tube}$ is the inner perimeter of the tube.
For transitional and fully turbulent flow, Ng et al. [43] use the Gnielinsky and Petukhov equations, implementing a formulation of the Darcy friction factor $f_D$ in Equation 3.23, also devised by Petukhov [44].

$$h_{ref} = \frac{k_{ref} Nu}{D_{h,tube}} \tag{3.19}$$

$$Nu = \begin{cases} 3.66 + \frac{0.0668 \cdot \frac{D_{h,tube}}{B_W} Re_{tube} Pr_{ref}}{1 + 0.04\left(\frac{D_{h,tube}}{B_W} Re_{tube} Pr_{ref}\right)^{2/3}} & \text{Hansen equation if laminar } Re_{tube} \leq 2,300 \\ \frac{\frac{f_D}{8}\left(Re_{tube} - 1000\right) Pr_{ref}}{1.07 + 12.7\sqrt{\frac{f_D}{8}}\left(Pr_{ref}^{2/3} - 1\right)} & \text{Gnielinsky equation if transitional } 2,300 < Re_{tube} < 10^4 \\ \frac{\frac{f_D}{8} Re_{tube} Pr_{ref}}{1.07 + 12.7\sqrt{\frac{f_D}{8}}\left(Pr_{ref}^{2/3} - 1\right)} & \text{Petukhov equation if turbulent } Re_{tube} \geq 10^4 \end{cases} \tag{3.20}$$

$$Re_{tube} = \frac{u D_{h,tube}}{\nu} \quad (3.21) \qquad D_{h,tube} = 4\frac{A_{ref,pass}}{P_{tube}} \quad (3.22) \qquad f_D = \left(0.79 \log\left(Re_{tube}\right) - 1.64\right)^{-2} \quad (3.23)$$

### 3.1.2. PFHX Model

The PFHX model is adopted from the section on offset strip fin HX in the book *"Fundamentals of Heat Exchanger Design"* by Shah and Sekulić [32], which use a Colburn $j-$factor and a Fanning friction $f-$factor model developed by Manglik and Bergles [33]. The data gathered for the $j$ and $f$ correlations was performed with air. However, the authors specifically note that the correlations should be valid for $0.5 < Pr < 15$, which applies to air, water and a large variety of common refrigerants.

$$\begin{aligned} j =& 0.6522\, Re_{cell}^{-0.5403} \left(\frac{w_{cell}}{h_{fin}}\right)^{0.1541} \left(\frac{t_{fin}}{\ell_s}\right)^{0.1499} \left(\frac{t_{fin}}{w_{cell}}\right)^{-0.0678} \\ & \times \left[1 + 5.269 \times 10^{-5}\, Re_{cell}^{1.340} \left(\frac{w_{cell}}{h_{fin}}\right)^{0.504} \left(\frac{t_{fin}}{\ell_s}\right)^{0.456} \left(\frac{t_{fin}}{w_{cell}}\right)^{-1.055}\right]^{0.1} \end{aligned} \tag{3.24}$$

$$Re_{cell} = \frac{uD_{h,cell}}{\nu} \quad (3.25) \qquad D_{h,cell} = \frac{4A_{0,\text{cell}}}{A_{\text{cell}}/\ell_s} = \frac{4w_{cell}h_{fin}/\ell_s}{2(w_{cell}\ell_s + h_{fin}\ell_s + h_{fin}t_{fin}) + w_{cell}t_{fin}} \quad (3.26)$$

The cell-specific $Re$, denoted as $Re_{cell}$ uses the hydraulic diameter of one offset strip fin cell $D_{h,cell}$. Since the implemented PFHX model uses rectangular offset strip fins for both the air and refrigerant side and the specified fluid range of applicability of the model by Manglik and Bergles, the $j-$ and $f-$factor can be used for both streams. Then, as for the FTHX, Equation 3.10 can be used in combination with Equation 3.24. The heat transfer area, which is needed in Equation 3.7 is split into two contributions, the plate area ($A_{air,plate}$ in Equation 3.27) and the fin area ($A_{air,fin}$ in Equation 3.28), as was done for the air side in Equation 3.12.

$$\begin{aligned} A_{air,plate} = &\underbrace{2B_D B_W n_{air,layers}}_{\text{total plate area}} - \underbrace{2t_{fin,air}B_D n_{f,air}}_{\text{fin base area covering plates}} + \underbrace{2h_{fin,air}B_D n_{air,layers}}_{\text{sides of air passage rows (header bars)}} \\ &+ \underbrace{2\left(h_{fin,ref} + 2t_{plate}\right) n_{ref,layers} B_W}_{\text{area of plates and header bars of other fluid at core inlet and outlet faces}} \end{aligned} \quad (3.27)$$

$$\begin{aligned} A_{air,fin} = &\underbrace{2h_{cell,air}B_D n_{f,air}}_{\text{fin height area}} + \underbrace{2h_{cell,air}t_{fin,air}n_{strips,air}n_{f,air}}_{\text{fin edge height area}} \\ &+ \underbrace{w_{cell,air}t_{fin,air}\left(n_{strips,air} - 1\right)n_{f,air} + 2p_{f,air}t_{fin,air}n_{f,air}}_{\text{fin edge width area}} \end{aligned} \quad (3.28)$$

Then, reformulating the above for the refrigerant side to obtain Equation 3.29 and Equation 3.30

$$\begin{aligned} A_{ref,plate} = &\underbrace{2B_W B_D n_{ref,layers}}_{\text{total plate area}} - \underbrace{2t_{fin,ref}B_W n_{f,ref}}_{\text{fin base area covering plates}} + \underbrace{2h_{fin,ref}B_W n_{ref,layers}}_{\text{sides of air passage rows (header bars)}} \\ &+ \underbrace{2\left(h_{fin,air} + 2t_{plate}\right) n_{air,layers} B_D}_{\text{area of plates and header bars of other fluid at core inlet and outlet faces}} \end{aligned} \quad (3.29)$$

$$\begin{aligned} A_{ref,fin} = &\underbrace{2h_{cell,ref}B_W n_{f,ref}}_{\text{fin height area}} + \underbrace{2h_{cell,ref}t_{fin,ref}n_{strips,ref}n_{f,ref}}_{\text{fin edge height area}} \\ &+ \underbrace{w_{cell,ref}t_{fin,ref}\left(n_{strips,ref} - 1\right)n_{f,ref} + 2p_{f,ref}t_{fin,ref}n_{f,ref}}_{\text{fin edge width area}} \end{aligned} \quad (3.30)$$

The multitude of geometric parameters included in the calculation of $A_{air,ht}$ and $A_{ref,ht}$ is illustrated in Figure 3.5

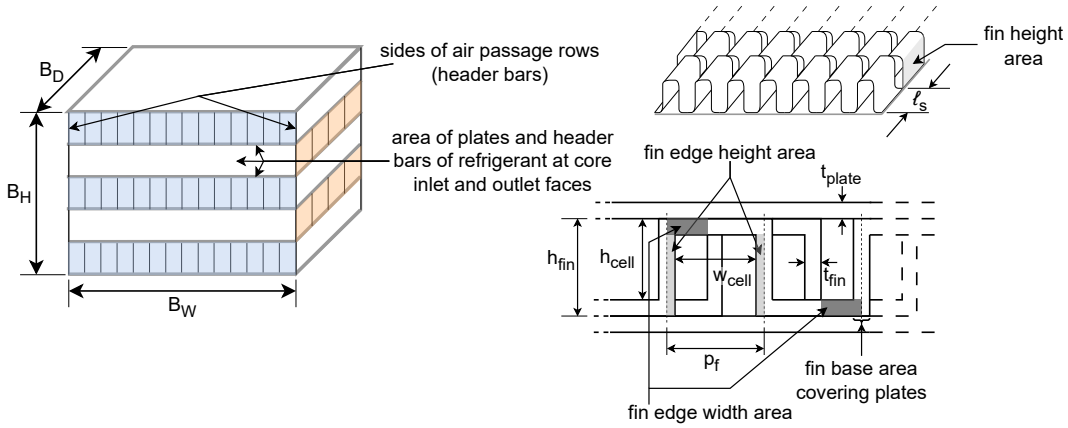


**Figure 3.5:** The PFHX dimensions as used in **DRAX**. Left: An exemplary PFHX block with air (blue) and refrigerant (orange). Top right: Offset strip fin layer of the PFHX. Bottom right: Offset strip fin cross section with 2 strips. Figures produced according to "*Fundamentals of Heat Exchanger Design*" [32].

Lastly, the fin efficiency parameter $\eta_0$ can be found with Equation 3.17 and an expression for the straight fin efficiency $\eta_f$, which is derived through Shah and Sekulić [32]. The parameter $k_{fin}$ in Equation 3.32 describes the thermal conductivity of the fin material.

$$\eta_f = \frac{\tanh m\ell}{m\ell} \qquad (3.31) \qquad m\ell = \sqrt{\left[\frac{2h_{fin}}{k_{fin}t_{fin}}\left(1+\frac{t_{fin}}{\ell_s}\right)\right]}\left(\frac{h_{fin}}{2}-t_{fin}\right) \qquad (3.32)$$

## 3.2. HX Pressure Drop Model

Generally, the pressure loss in a heat exchanger can stem from four sources. Friction, contraction and expansion losses as well as momentum losses. The latter plays a major role in two-phase heat exchangers, where the inlet and outlet density greatly vary. For single phase cases, such as the heat exchanger models implemented in **DRAX**, momentum losses may be neglected, which results in Equation 3.33 for the relative pressure drop. The first and last term in Equation 3.33, which describe the pressure drop and recovery due to the blockage as $\pm(1-\sigma^2)$ and the losses due to small scale separation at the entrance and exit, $K_c$ and $K_e$ respectively, can be reduced to only the loss factors in Equation 3.34. To account for pressure losses due to tilting the HX, an amplification factor $K_\theta$ is introduced, which is further discussed in subsection 3.2.4.

The pressure drop on either side of the HX can be found by using Equation 3.34 where the subscript $i$ stands for inlet conditions (station 2 for the air and a value stemming from the TMS for the refrigerant, typically around 2-3 bar). The channel length $L$ for air is the core depth $B_D$ while for the refrigerant, it is the core width $B_W$. The friction factor $f$ used here is the Fanning friction factor which four times smaller than the Darcy friction factor $f_D$.

$$\frac{\Delta p}{p_i} = \frac{G^2}{2\rho_i p_i}\left[\underbrace{1-\sigma^2+K_c}_{\text{contraction effect}} + \underbrace{f\frac{4L}{D_h}}_{\text{core friction}} - \underbrace{\left(1-\sigma^2-K_e\right)}_{\text{expansion effect}}\right] \times \underbrace{K_\theta}_{\text{HX tilt}} \qquad (3.33)$$

$$\frac{\Delta p}{p_i} = \frac{G^2}{2\rho_i p_i}\left[K_c + f\frac{4L}{D_h} + K_e\right] \times K_\theta \qquad (3.34)$$

### 3.2.1. Contraction and Expansion Losses

The contraction and expansion loss factors $K_c$ and $K_e$ have been determined experimentally by Kays and London [36] for various fin profiles. Their data is plotted in Figure 3.6 against the HX core area ratio $\sigma$, which is defined as the ratio of total passage area $A_{tot,pass}$ to the full frontal area of the core $A_{fr}$, such as in Equation 3.35. The total passage area is found geometrically for each fluid stream and does not need to be elaborated.

$$\sigma = \frac{A_{tot,pass}}{A_{fr}} \qquad (3.35) \qquad A_{fr,air} = B_W \cdot B_H \qquad (3.36) \qquad A_{fr,ref} = B_D \cdot B_H \qquad (3.37)$$

The flat tubes of the FTHX obtain their contraction and expansion loss coefficients from Figure 3.6a, while the louvered fins are approximated as the triangular fins of Figure 3.6b. The rectangular offset strip fin passages obtain their loss coefficients from Figure 3.6c. In **DRAX**, for the flat tubes and the offset strip fins, the values of $K_c$ and $K_e$ at a specified $\sigma$ are determined through a linear interpolation function for their hydraulic diameter-specific $Re_{D_h}$, where $Re_{tube}$ and $Re_{cell}$ from section 3.1 are used. If $Re_{tube}$ or $Re_{cell}$ is smaller than 2,000, the laminar data in the charts is picked. If $Re_{tube}$ or $Re_{cell}$ is larger than 10,000, the data for $Re = \infty$ in the charts is picked.

For the louvered fins, it is assumed that the louvers mix the flow such that the flow can be assumed fully turbulent. Hence, $Re = \infty$ is chosen by default in Figure 3.6b, instead of the louver-pitch-specific $Re_{L_p}$.

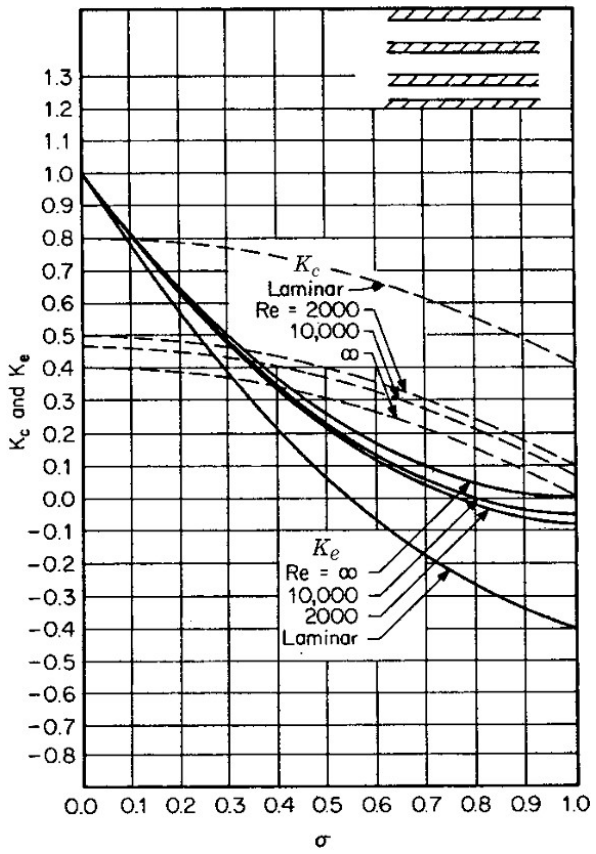


**(a)** $K_c$ and $K_e$ for flat tubes.

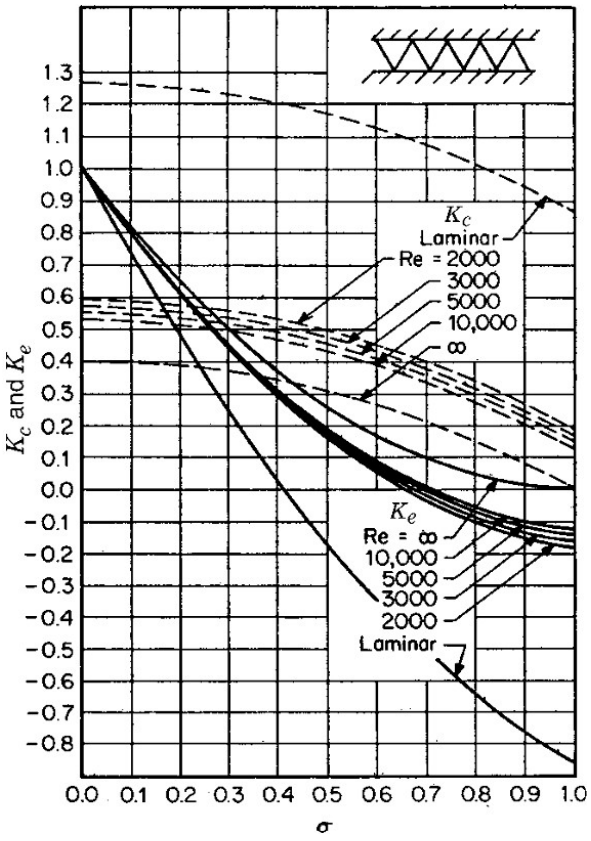


**(b)** $K_c$ and $K_e$ for louvered fins.

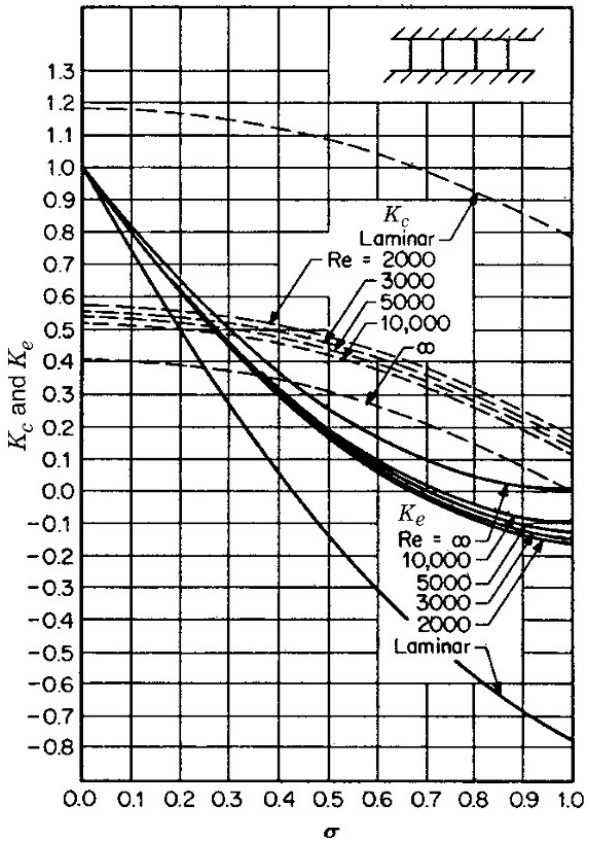


**(c)** $K_c$ and $K_e$ for offset strip fins.

**Figure 3.6:** $K_c$ and $K_e$ plotted against the blockage ratio $\sigma$ of the core for various flow regimes. Data from Kays and London [36].

### 3.2.2. FTHX Core Losses

For the air side of the louvered fin flat tube heat exchanger, Equation 3.38 from Dong et al.[41] is utilized, respecting the $Re_{Lp}$ from Equation 3.9 and the geometric definitions from Table 3.1.

$$f_{air} = 0.54486 Re_{L_p}^{-0.3068} \left(\frac{L_a}{90}\right)^{0.444} \left(\frac{F_p}{L_p}\right)^{-0.9925} \left(\frac{F_h}{L_p}\right)^{0.5458} \left(\frac{L_h}{L_p}\right)^{-0.2003} \left(\frac{L_d}{L_p}\right)^{0.0688} \tag{3.38}$$

The refrigerant losses in the flat tubes are covered by two $f-$factor relations, noted in Equation 3.39. As was stated before, the friction factor $f$ here is not the same as $f_D$ used in the Gnielinsky and Petukhov equation in Equation 3.20 as the Darcy friction factor $f_D$ relates to the Fanning friction factor $f$ by a multiplier of 4. When going through literature, attention should be paid regarding which definition of the friction factor is used.
The equation for $f_{ref}$ for transitional and turbulent flow implemented in **DRAX** is the same. That is because transitional flow is both hard to predict and not very well understood, such that, due to the lack of an appropriate correlation, the equation for fully developed turbulent flow was extended into the transitional domain. Due to the very large aspect ratio of the flat tube cross section, the expression for $f$ in fully developed laminar flow in rectangular tubes with infinite aspect ratio from Shah and Sekulić [32] is taken. For the transitional and fully developed turbulent flow, Petukhov's expression for $f_D$ from Equation 3.23 is converted to $f$.

$$f_{ref} = \begin{cases} \frac{24}{Re_{tube}} & \text{for fully developed laminar flow, } Re \leq 2,300 \\ \frac{1}{4}\left(0.79 \log\left(Re_{tube}\right) - 1.64\right)^{-2} & \text{for transitional and fully developed turbulent flow, } Re > 2,300 \end{cases} \tag{3.39}$$

### 3.2.3. PFHX Core Losses

The friction factor for the PFHX can be derived for both fluid streams with Equation 3.40. As was discussed in subsection 3.1.2, the range of applicability of the $j$ and $f$ factor correlations developed by Manglik and Bergles [33] should in theory include both the air and refrigerant side of the PFHX.

$$\begin{aligned} f =& 9.6243\, {Re_{cell}}^{-0.7422} \left(\frac{w_{cell}}{h_{fin}}\right)^{0.1856} \left(\frac{t_{fin}}{\ell_s}\right)^{0.3053} \left(\frac{t_{fin}}{w_{cell}}\right)^{-0.2659} \\ &\times \left[1 + 7.669 \times 10^{-8}\, {Re_{cell}}^{4.429} \left(\frac{w_{cell}}{h_{fin}}\right)^{0.920} \left(\frac{t_{fin}}{\ell_s}\right)^{3.767} \left(\frac{t_{fin}}{w_{cell}}\right)^{0.2369}\right]^{0.1} \end{aligned} \tag{3.40}$$

### 3.2.4. HX Tilt Factor

Clearly, tilting the HX with respect to the incoming flow will have the advantage of reducing the flow-relative frontal area of the core, leading to a more compact nacelle, which lowers the external part of the cooling drag. However, this benefit on one side comes at a cost on the other side as the tilt also causes a larger internal flow deviation for the ram-air, which in turn increases the internal resistance that the HX has in the duct. Kuechemann [8] establishes the valid analogy that to the incoming air, the tilted refrigerant passages act such as airfoils, or guidance vanes. Naturally, if their angle of deflection is too extreme, the flow separates and large air-side pressure losses must be accepted. Luckily, tilting the HX within the considered range of tilt angles $\theta$ (up to 70°) has a negligible influence on the heat exchange [45], such that no amendments need to be made to section 3.1.
To quantify the effects of tilting the HX, the tilt factor $K_\theta$, based on data gathered by Nichols [18] is used. It's apparent that the data is quite dated (1942) and that nuances, such as the sharpness of passage rows (i.e. the tubes on a FTHX) are not accounted for. Moreover, Nichols' tests look at a straight outflow after the core outlet that is aligned with the core, as illustrated in Figure 3.8. That condition is not given in the ducts modeled in this study, as the flow needs to be redirected into the duct nozzle. Therefore, it would be recommended to gather data for ducted HX designs that are more relevant today.
Nevertheless, the findings of Nichols serve as a good basis to implement a more notional function for $K_\theta$. Nichols performed tests on an intercooler constructed similarly to the FTHX model implemented in

**DRAX** oriented horizontally and vertically. When oriented horizontally, the flat tubes redirect the flow. Vertically, it is the fins on the air side that redirect the flow. The flat tubes are more effective at redirecting the flow than the fins and therefore, losses remain lower for a large domain of $\theta$ and the inflection point at which $K_\theta$ becomes very large is slightly delayed, when compared to the vertical setup ($\theta = 70°$ vs. $\theta = 66°$).
The function for $K_\theta$, implemented in **DRAX** is plotted below. The asymptotic behavior exhibited by the tilt factor $K_\theta$ in Nichols' results is approximated by two piece-wise linear functions, as can be seen in Figure 3.7. The default HX orientation in **DRAX** is horizontal but can be changed by the user if desired.

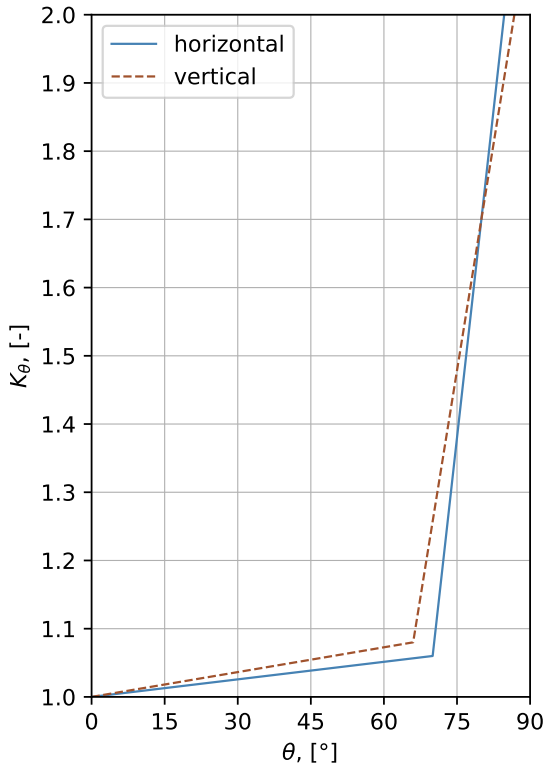


**Figure 3.7:** The tilt factor functions implemented in **DRAX**. Approximated data from Nichols [18].

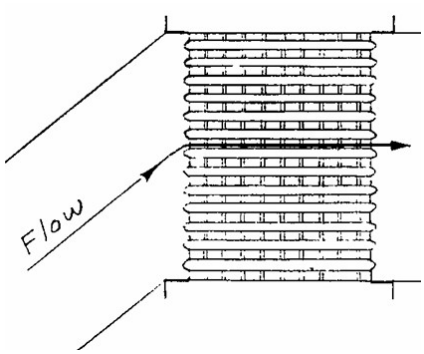


**(a)** The horizontally oriented HX test setup.

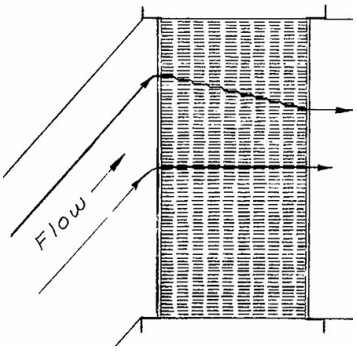


**(b)** The vertically oriented HX test setup.

**Figure 3.8:** The test setups of Nichols [18] with a straight outflow condition.

## 3.3. Internal Drag Model

The internal model can be considered as a very abstract representation of the actual ducted HX, as illustrated in Figure 3.9. The noted numbering for stations along the captured streamtube of air that passes through the duct and the HX will be used as the convention throughout this work. The model resources for the diffuser and the HX, which were found in chapter 2, need to be implemented robustly under consideration of their declared range of applicability.

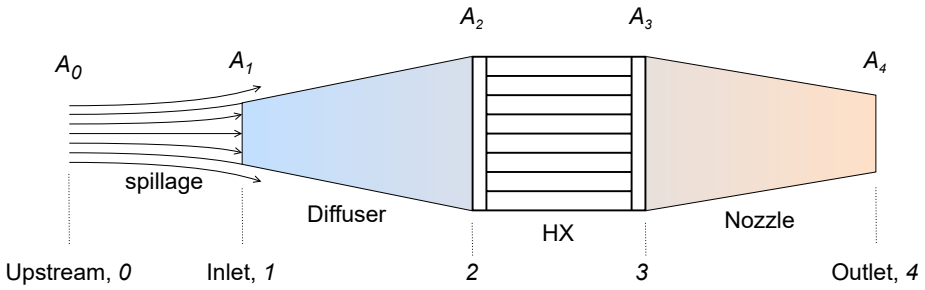


**Figure 3.9:** Abstract model

The methodology to assess internal drag, as it is laid out in this work, starts at station 1, hence the duct inlet. The reason for starting there instead of the upstream point 0 will become apparent in subsection 3.3.4, where the idea of an iterative method to assess spillage is introduced which encloses the system from station 0 to 4.

### 3.3.1. Diffuser (1-2)

The diffuser is assumed to have straight walls and is quasi-2D. Figure 3.10 shows the geometric parameters needed to assess the area ratio $AR = A_2/A_1$, which directly controls the static pressure rise through the diffuser. The assumption is made that for the tilted HX, $AR$ can be assessed such that the frontal area of the HX ($A_{fr,air} = B_W \cdot B_H$) is projected orthogonally to the diffuser midline. That is, the straight line connecting the inlet center to the center of the HX face. This relation is noted in Equation 3.41. It is important to note that since the diffuser midline may not be horizontal, the flow-relative HX inclination $\theta$ is not equal to the geometric inclination $\theta_{geom}$.

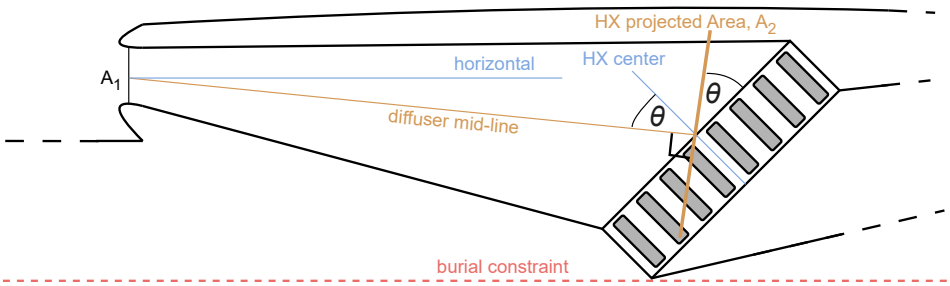


**Figure 3.10:** The geometry of the diffuser with the flow-relative inclination of the heat-exchanger $\theta$.

$$AR = \frac{A_2}{A_1} = \frac{A_{fr,air}}{A_1} \cdot \cos\theta \tag{3.41}$$

The diffuser model generated by Pittaluga [16] is implemented in the diffuser part of DRAX as an adaptation of the original model. The correlations belonging to Equation 3.42 are valid in a limited geometric domain for the expansion ratio ($AR$), that is, between 2 and 4.
Figure 3.11 shows the static pressure rise and the isentropic efficiency of the diffuser for an exemplary flow at cruise ($M_{cr} = 0.3$, $h_{cr} = 5500$ m). The dashed lines in the plot show the original model from Equation 3.42 being applied throughout the entire range of diffuser expansion ratios. It is easy to see that if one were to implement Pittaluga's model at $AR < 2$ going towards 1, it would result in a nonphysical response of the model, where the diffuser isentropic efficiency is larger than 1, thereby adding work to the flow without any mechanical input.

To fix this, the implemented model assumes that for a straight diffuser, akin to a constant cross-section duct, losses are nil and interpolates the losses at $1 < AR < 2$. While expansion losses would surely not be present if no expansion occurs, this also assumes that viscous losses due to friction between the flow boundary layer and the duct wall are zero at $AR = 1$. Admittedly, this is optimistic, but prescribing a value to frictional losses without tests or another empirical model would be hard to substantiate. Moreover, it will be shown later on that the $AR$ values that are attained in duct designs are around 2 and above. If the model was not corrected, any unbound optimizer would seek to exploit values of $AR$, where the diffuser appears to energize the flow.
Likewise, for $AR > 4$, the static pressure rise through the diffuser is assumed to no longer grow. Unlike the unbounded version of Pittaluga's model, there is not a significant increase in losses above $AR = 4$. In most cases, $AR > 4$ is only attained if the HX is not tilted or some other unlikely condition is set and therefore not really relevant to this work or any realistic use case of **DRAX**.

$$C_p^* = g_1 \cdot g_2 \cdot \left\{ 1 - \frac{1.03 \cdot (1 - B_1)^2}{\overline{AR}^2 \left[ 1 - 0.820 \cdot \overline{AR}^{0.07} \cdot B_1^{1/(2\overline{AR}-1)} \right]^2} \right\} \tag{3.42}$$

$$g_1 = \begin{cases} 1 + 0.1 \cdot (AR - 3), & \text{if } M_1 < 0.4 \\ [1 + 0.1 \cdot (AR - 3)] \cdot [1 + 0.203\,(M_1 - 0.4)] \cdot \left[1 - (M_1 - 0.4)^4\right], & \text{if } 0.4 \leq M_1 \leq 0.8 \end{cases}$$

$$g_2 = \begin{cases} \left[Re_1 \cdot 10^{-5}\right]^{0.02(1-3B_1)}, & \text{when } Re_1 \leq 250,000 \\ \left[250,000 \cdot 10^{-5}\right]^{0.02(1-3B_1)}, & \text{when } Re_1 > 250,000 \end{cases}$$

$$\overline{AR} = AR \cdot 1.9 \frac{2AS - 0.3}{AS \cdot [1 + 3.6\,(B_1 - 0.07)]}$$

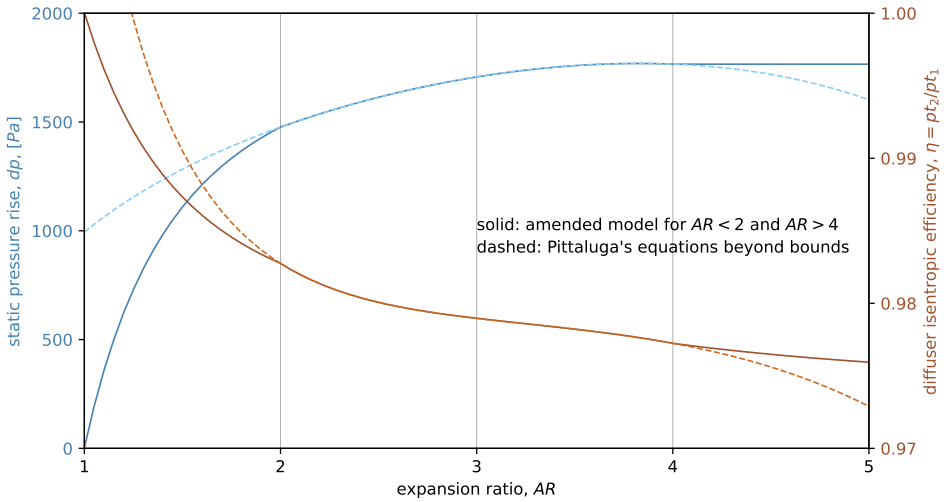


**Figure 3.11:** The variation in static pressure rise and isentropic efficiency of the diffuser with the expansion ratio. Comparison of the original model and the amended model beyond the bounds designated by Pittaluga [16]. Cruise conditions ($M_{cr} = 0.3$, $h_{cr} = 5500$ m, ISA)

After evaluating the static pressure at station 2 with Equation 3.43 and Equation 3.44, the density and temperature of the air before passing through the HX are determined with Equation 3.45 and the ideal gas law in Equation 3.46.

$$\Delta p_{diff} = C_p^* \cdot \frac{1}{2} \overline{u}_1^2 \rho_1 \quad (3.43) \qquad p_2 = p_1 + \Delta p_{diff} \quad (3.44)$$

$$\rho_2 = \left(\frac{p_2}{p_1}\right)^{1/\gamma} \cdot \rho_1 \quad (3.45) \qquad T_2 = \frac{p_2}{\rho_2 R} \quad (3.46)$$

### 3.3.2. HX Pressure Drop (2-3)

The exact method for how to determine the pressure drop in the HX is presented in section 3.2. The air properties at the HX outlet (station 3) are changed as noted in Equation 3.47 to Equation 3.50.

$$p_3 = p_2 - \Delta p_{HX} \quad (3.47) \qquad T_3 = T_2 + \Delta T_{HX} \quad (3.48)$$

$$\rho_3 = \frac{p_3}{R T_3} \quad (3.49) \qquad V_3 = \frac{\dot{m}_{air}}{\rho_3 A_3} \quad (3.50)$$

### 3.3.3. Nozzle (3-4)

The nozzle is by far the most simplified part of **DRAX**. Two factors lead to the omission of a more elaborate model for the nozzle, which is at the current stage, resolved with 1D isentropic flow equations. Primarily, there is a lack of appropriate resources. While some authors [27, 24, 34] of works developing a model for cooling drag resort to work on turbomachinery [29, 37] for a model that quantifies nozzle losses, it was decided that those models likely pose little relevance to the duct model in **DRAX**.

The second point is that the losses in the nozzle are very small compared to other parts of the duct. Since the air experiences a favorable pressure gradient in the converging nozzle, losses due to separation are not present and might only occur at the location where the air exiting the HX is directed into the main flow direction of the nozzle. Friction losses are present in the nozzle and, in order to provide the option of implementing some control over losses, **DRAX** includes the nozzle isentropic efficiency $\eta_{noz}$, by default set to 1 but which can be readily varied by the user. The role of $\eta_{noz}$ is simply put in Equation 3.51.

$$p_{t4} = \eta_{noz} p_{t3} \tag{3.51}$$

As will be discussed in section 3.6, **DRAX** has multiple modes of employment. This is particularly important for the nozzle, as the nozzle area controls the outlet conditions and how much air is spilled at the duct inlet. Depending on which mode of employment is used, either the specified inlet condition (e.g. 0 spillage) controls the outlet area, making $A_4$ an easy to solve explicit equation, or a specified outlet area leads to an implicit equation for the outlet mach number $M_4$, which needs to be solved iteratively from station 0 to 4. The latter process is complex and relevant enough that it has been reserved its proper place in this thesis, in subsection 3.3.4.
If $A_4$ is being sized such that the flow is expanded perfectly into the freestream ($p_4 = p_0$) and therefore solved explicitly, Equation 3.52 is used in combination with the connoted equations.

$$M_4 = \sqrt{\left[\frac{p_{t4}}{p_4}^{(\gamma-1)/\gamma} - 1\right]\frac{2}{\gamma-1}} \tag{3.52}$$

$$\rho_4 = \left(\frac{p_4}{p_3}\right)^{1/\gamma} \rho_3 \tag{3.53}$$

$$T_4 = \frac{p_4}{\rho_4 R} \tag{3.54}$$

$$V_4 = M_4\sqrt{\gamma R T_4} \tag{3.55}$$

$$A_4 = \frac{\dot{m}_{air}}{\rho_4 V_4} \tag{3.56}$$

If, on the other side, the exit area $A_4$ is already known, for example if an existing design is being analyzed, then the root of Equation 3.57 needs to be solved for numerically with $M_4$ being the variable. In **DRAX**, this is done with a newtonian scheme from the *scipy.optimize* library[46]. Then, the pressure at station 4 is found with the isentropic relation noted in Equation 3.58 and the density and temperature from Equation 3.53 and Equation 3.54, respectively. The outlet velocity $V_4$ is derived from $M_4$ and $T_4$ through Equation 3.55.

$$\frac{A_3}{A_4} = \left[\frac{\left(1+\frac{\gamma-1}{2}{M_3}^2\right)^{(\gamma+1)/(2(\gamma-1))}}{M_3}\frac{M_4}{\left(1+\frac{\gamma-1}{2}{M_4}^2\right)^{(\gamma+1)/(2(\gamma-1))}}\right] \tag{3.57}$$

$$p_4 = p_{t4}\left[1+\frac{\gamma-1}{2}{M_4}^2\right]^{-\gamma/(\gamma-1)} \tag{3.58}$$

### 3.3.4. Spillage Determination (0-4)

The system that is depicted in Figure 3.9 is a closed one, meaning that the condition is imposed that the pressure at the duct outlet equals the ambient pressure. Hence, $p_4 = p_0$. Hoerner [23] finds that the scavenging effect at the outlet is minimal and therefore it can be imposed that this condition needs to be met. If the outlet pressure is lower than the ambient, it means that the nozzle is under-expanded and the resistance in the duct is too high. The result is a back pressure effect coming from the rear. Effectively, this resistance is transferred to the duct inlet which results in spillage. The graph in Figure 3.12 visualizes well how spillage nearly directly controls that the outlet condition $p_4 = p_0$ can be met.
Spillage is a diffusion effect taking place before the inlet (0-1) and, just like the actual diffuser between stations 1 and 2, builds up the pressure head needed to push the air through the ducted HX. Section 3.3.3 touched upon the different modes of employment in **DRAX**, noting that if the design is already predefined, Equation 3.58 is used to obtain the outlet pressure. If $p_4$ is too low, the pressure at the inlet $p_1$ needs to be increased, meaning that spillage is assumed. In **DRAX**, this is done by Equation 3.59 where $p_{1,0}$ is the inlet pressure of the previous iteration, equal to $p_0$ when the iteration is first initiated. A damping factor or $0.2$ is included as using **DRAX** under different conditions has shown that

sometimes, if the outlet pressure is much too low, an undamped iteration causes the updated $p_1$ to exceed the total pressure in the flow. Besides being unphysical, the condition of $p_1 > p_{t,0}$ causes **DRAX** to crash. The calculations from station 1 to 4 are re-performed and the new $p_4$ is obtained. This cycle is repeated until the outlet condition is met. The updated mass flow through the duct $\dot{m}_{air}$, dependent on $p_1$ is calculated according to Equation 3.60 until Equation 3.63, assuming ideal efficiency between 0 and 1. The spilled air mass flow $\dot{m}_{spill}$ can then be found with Equation 3.64 and the spillage rate $SR$, in percent, is calculated as in Equation 3.65. A note on the subscripts; the area $A_0$ is the area of the contracted streamtube, theoretically infinitely far upstream of the inlet. When calculating the mass flow $\dot{m}_0$, which signifies the maximum mass intake possible for the inlet, $A_1$ must be projected, instead of $A_0$.

$$p_1 = p_{1,o} + 0.2 \cdot (p_0 - p_4) \tag{3.59}$$

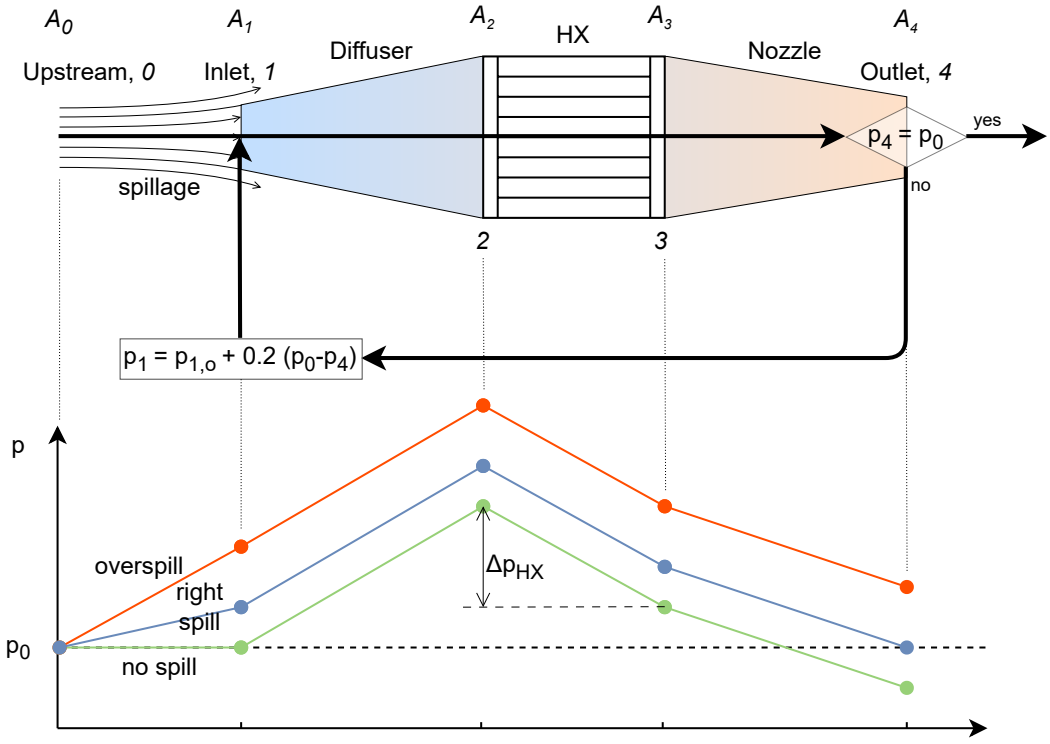


**Figure 3.12:** A visualization of the influence that spillage has on the outlet pressure along with simplified layover of the spillage iteration loop, implemented in **DRAX**.

$$\rho_1 = \left(\frac{p_1}{p_0}\right)^{1/\gamma} \rho_0 \tag{3.60}$$

$$T_1 = \frac{p_1}{\rho_1 R} \tag{3.61}$$

$$M_1 = \sqrt{\frac{2}{\gamma - 1}\left[\left(\frac{p_0}{p_1}\right)^{(\gamma-1)/\gamma}\left(\frac{\gamma - 1}{2}{M_0}^2 + 1\right) - 1\right]} \tag{3.62}$$

$$\dot{m}_{air} = \dot{m}_1 = \rho_1 A_1 M_1 \sqrt{\gamma R T_1} \tag{3.63}$$

$$\dot{m}_{spill} = \dot{m}_0 - \dot{m}_1 = \rho_0 A_1 V_0 - \dot{m}_{air} \tag{3.64}$$

$$SR = \frac{\dot{m}_{spill}}{\rho_0 A_1 V_0} \tag{3.65}$$

At this stage, the internal drag can be computed by looking at the momentum deficit that the captured streamtube experiences between station 0 and 4. The formula is analogous to the one used when

calculating the thrust in jet engine cycles and is noted in Equation 3.66. Since the condition that $p_4 = p_0$ must be met by spillage, as the lengthy discussion above should by now have clarified, no pressure differential term is included in the internal drag.

$$D_{int} = \dot{m}_{air} \left( V_0 - V_4 \right) \tag{3.66}$$

The presence of spillage creates a lip suction effect, which was presented in subsection 2.5.1. Depending on the design of the inlet lip and the duct forebody, this lip suction assumes different strengths which offset some of the pre-entry drag that occurs when the incoming air is slowed down prior to entering the duct. In this work, the lip suction effect is resolved not by the internal model but by the external one, as the lip suction is generated by the outer stream tube of air that evades the duct. The spillage effect on the external drag is quantified in subsection 3.5.5.

## 3.4. Translation of Shapes

The abstract model depicted in Figure 3.9 and Figure 3.12 has so far served as a map of the internal parts of the duct, sufficient for the 1D calculation of the internal drag. In order to eventually turn this into a tangible shape, an intermediate function is required that generates a duct housing for a HX. Furthermore, this duct housing needs to be constructed in a CAD modeling software in order to generate a 3D shape to be used in the external drag analysis of the model. This is a rather tricky task given that the scope of this study is not to generate an intricately detailed design for a ducted HX, but rather to give a good estimate of the cooling drag with **DRAX** and possibly reach guidelines or best-practice-advice for integrating and designing a ducted HX for an electric propulsion aircraft.
The first part of this section (subsection 3.4.1) will therefore attempt to generate a set of design rules for the integration of the HX in a fuselage bound duct. These design rules are implemented into the function **TOS** (for **T**ranslation **O**f **S**hapes), a part of **DRAX**, in order to predefine the duct geometry and yield inputs for the CAD model. Finally, the method used to generate the duct shapes in *OpenVSP*, the chosen CAD software, is laid out such that it can be reproduced (subsection 3.4.2).

### 3.4.1. Design Rules

Section 2.4 touched upon the guidelines to be followed in HX integration, identifying 2 chief considerations. Primarily, the heat source, a FC or battery, should be close to the heat sink, being the HX, in order to minimize piping mass and losses in the TMS. Therefore, taking into account the projects that *Pipistrel* has been or is working on, namely the Unifier 19 and the Newborn projects, presented in subsection 2.4.1 and subsection 2.4.4, respectively, the choice for a fuselage-bound ducted HX was made.
Next to that and quite obviously, the cowling not only needs to provide housing for the diffuser, the HX and the nozzle, but also needs to cover the piping leading to the HX, more specifically the header bars that distribute the refrigerant into the the HX channels. This leads to the design choice that in the duct, the HX shall be arranged and tilted horizontally, as in Figure 3.13, under consideration of the tilting effect in subsection 3.2.4. That way, the protrusion height, that is depicted in Figure 3.13 can be minimized.

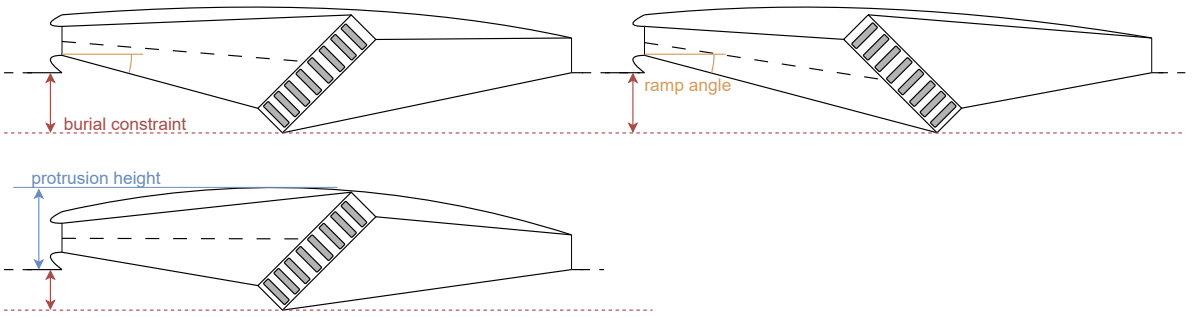


**Figure 3.13:** Three variations of the same HX installation (same frontal area and absolute tilt angle). Top row: same burial constraint but opposite direction of tilt. Bottom: same tilt direction as top left but tighter burial constraint, leading to a larger protrusion height.

Figure 3.13 shows three variations of the same HX installation with the same HX tilt angle and the same HX frontal area. The purpose of the top drawings is to show that even though both HX have the same absolute geometric tilt angle in the installation, the direction of tilt depicted on the right leads to a more severe flow relative tilt angle in the diffuser as well as a more severe ramp angle, which is the angle of the lower diffuser wall. If this angle becomes too large (according to literature it should be limited to $8° - 10°$ [17]) the flow separates and losses in the diffuser excess unnecessarily.
The lower drawing in Figure 3.13 depicts the direct relation between burial constraint and the duct cowling protrusion height, which is sought to be minimized. On top of that, if the burial constraint becomes too stringent, both the top and bottom ramp angle can turn critical. In that case, the diffuser needs to be lengthened to taper the angle.

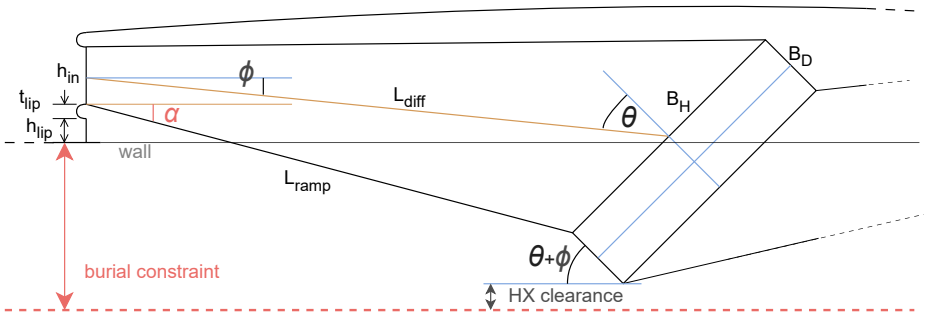


**Figure 3.14:** The definition of the diffuser and inlet geometry.

Figure 3.14 shows the definition of the diffuser and inlet geometry as it is determined in **TOS**. The symbols marked in Figure 3.14 are listed in Table 3.2

**Table 3.2:** List of parameters used in the geometric diffuser and inlet definition.

| Symbol | Explanation |
|---|---|
| $h_{in}$ | Inlet height |
| $h_{lip}$ | Diverter height; lip rise |
| $t_{lip}$ | Inlet lip thickness |
| $B_H$ | HX core height |
| $B_D$ | HX core depth |
| $L_{diff}$ | Diffuser length |
| $L_{ramp}$ | Lower ramp length |
| $\phi$ | Diffuser mid-line angle |
| $\alpha$ | Lower ramp angle |
| $\theta$ | Flow-relative HX tilt |

In order to minimize the protrusion height, **TOS** aims to bury the HX as far as possible into the fuselage, simplified as a flat wall. The ramp angle $\alpha$ and burial constraint act as design constraints in this regard and neither one can be exceeded. **TOS** solves the system of equations below by initially assuming that the lower ramp angle is fixed to its maximum bound and thereby checks if the burial constraint is exceeded (Equation 3.67 and Equation 3.68).
If the burial constraint is exceeded, hence if the burial depth $b$ is larger than the constraint, then $\alpha$ is decreased incrementally until the burial constraint is no longer violated. Lastly, **TOS** checks if the upper wall angle is too severe, namely by solving the system noted in Equation 3.69. Normally, this should not occur but if it does, $L_{diff}$ is lengthened incrementally until the upper ramp angle matches the constraint. These checks and adaptations are shown in Figure 3.15.
The systems in Equation 3.67 and Equation 3.69 are non-linear with the unresolved variables underlined in the equations. In **TOS**, they are solved using the *nsolve()* function from the *Sympy* package

$$\sum_{x,y} \begin{cases} x : L_{diff} \cos\left(\underline{\phi}\right) & = \underline{L_{ramp}} \cos\left(\alpha\right) + \frac{B_H}{2} \cos\left(\underline{\phi} + \theta\right) \\ y : L_{diff} \sin\left(\underline{\phi}\right) + \frac{B_H}{2} \cos\left(\underline{\phi} + \theta\right) & = \frac{h_{in}}{2} + \underline{L_{ramp}} \sin\left(\alpha\right) \end{cases} \tag{3.67}$$

$$b = -\left[h_{lip} + t_{lip} - L_{ramp} \sin\left(\alpha\right) - B_D \sin\left(\phi + \theta\right)\right] \tag{3.68}$$

$$\sum_{x,y} \begin{cases} x : L_{diff} \cos\left(\phi\right) + \frac{B_H}{2} \sin\left(\phi + \theta\right) & = \underline{L_{top,ramp}} \cos\left(\underline{\alpha_{upper}}\right) \\ y : -L_{diff} \sin\left(\phi\right) + \frac{B_H}{2} \cos\left(\phi + \theta\right) & = \frac{h_{in}}{2} + \underline{L_{top,ramp}} \sin\left(\underline{\alpha_{upper}}\right) \end{cases} \tag{3.69}$$

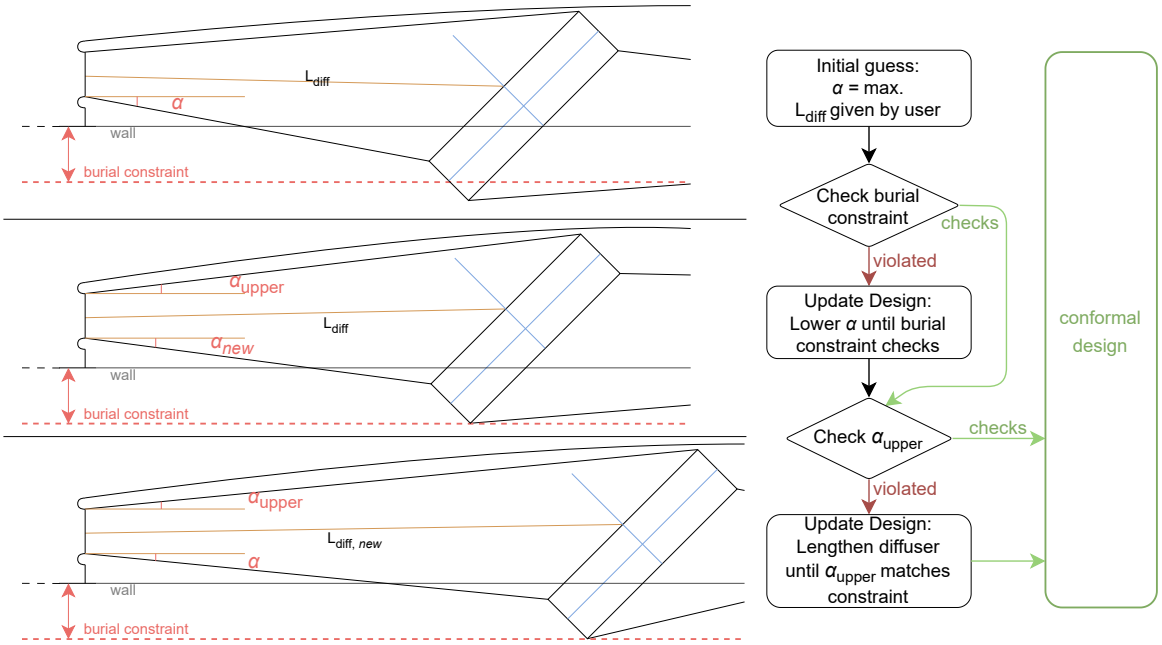


**Figure 3.15:** The design loop performed by **TOS** in a case, where a tight burial constraint leads first to lower ramp angle $\alpha$ reduction and then to diffuser lengthening in order to meet the diffuser wall angle constraint on the upper wall $\alpha_{upper}$.

Naturally, it is unlikely that the final design of a ducted ram air HX looks exactly as is shown in Figure 3.13 or any of the other shown drawings with perfectly straight inner walls. In fact, this would probably add unnecessary losses, for instance in the kinked connections between the diffuser, the HX and the nozzle. Therefore, it should be repeated that the methods laid out in this section serve to give a solid idea of the arrangements of the system and a generic, yet sensible aerodynamic shape for the cowling, not a detailed design. This becomes particularly apparent when generating the CAD model in subsection 3.4.2, where the inlet must be designed, a diverter is added and the cowling is shaped. A short preview on the methods and the reasoning is presented below.

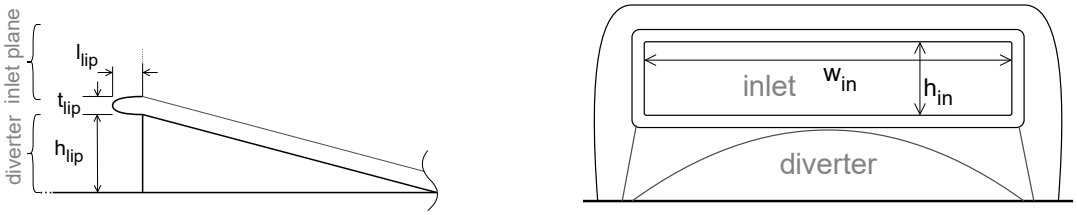


**(a)** Definition of the inlet lip and the diverter presence.

**(b)** Front view sketch of the inlet and semi-elliptical diverter.

**Figure 3.16:** Sketches of the inlet lip and notional diverter geometry.

The values for the inlet design, more specifically the lip and the highlight, are determined visually or by replicating typical designs found in the ESDU86002 engineering handbook on inlets[30]. Generically, the lip thickness $t_{lip}$ has a default value of 1 cm and the lip length $l_{lip}$, which defines the distance from the inlet plane to the highlight, being the front-most extremity, is by default also 1 cm. The result is a simple, yet realistic lip geometry which serves its purpose for this study.
The lower inlet lip-rise $h_{lip}$ is added in order to avoid flow blockage due to the fuselage's boundary layer. Since the flow speed in the boundary layer is reduced, it locally lowers the mass momentum, analogous to blocking part of the inlet plane, thus reducing the ingested air mass flow $\dot{m}_{air}$. Figure 3.16 shows the definition of the geometrical parameters belonging to the inlet lip and the role of the diverter. The diverter is added in order to dissipate the air that would accumulate between the inlet and the wall in a streamline manner. An initial external aerodynamic analysis of the cowling, without a diverter, resulted in significant separation zones at the cowling-wall junction, which can effectively be mitigated by even a simple diverter geometry. Section 3.4.2 gives a more concrete image of the diverter design.

### 3.4.2. CAD Model

*OpenVSP* offers various shapes and geometries that could be used to model the duct. While there even is a dedicated "Duct" class, it is more akin to the geometry of a turbofan cowling and is hollow in its center, like a donut. Contrary to that, the aim in modeling the duct cowling that houses the HX is not actually to generate a hollow shell, but rather to generate a closed body with subsurfaces for the inlet and outlet on which boundary conditions can be imposed - depending on the flow rate through the duct that is determined with **DRAX**.
Under that consideration, the "Stack" class in OpenVSP is ideal, as it allows the user to, as the name tells, stack cross sections on top of each other and connect them with a smooth surface. This makes shaping the duct cowling to be somewhat aerodynamic an easy task. The cross sections used to model the duct are rounded rectangles, with a varying radius. In OpenVSP, the user must specify $(x, y, z)$ coordinates and rotations for each cross section, relative to the prior cross section in the stack. Naturally, the width, height and edge radius of the rounded rectangle must also be provided. **TOS** automates the calculation of all these parameters and outputs them to the user, if desired. It would also be possible to fully automate the generation of these ducts by using the OpenVSP Python API. However, it was decided that implementing this step would be more time consuming than manually inputting the parameters into a pre-existing reference model, since the volume of tested ducts was kept comparatively small within this work.

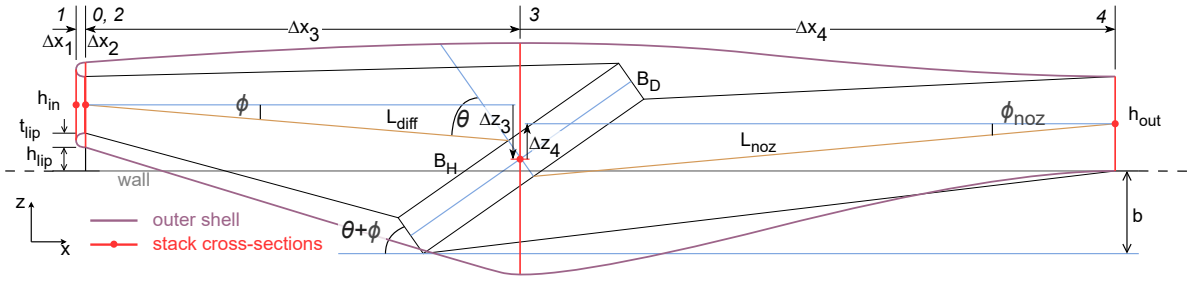


**Figure 3.17:** The stack cross sections that yield the outer shell enveloping the duct and HX.

Figure 3.17 portraits how the stack cross sections are positioned through the duct and how the generated surface envelops the ducted HX. Each duct cowling is made up of 5 stations, with indexing in OpenVSP starting at 0. Stations 0, 1 and 2 define the inlet and the lip. Station 3 coincides with the HX center and is sized according to the HX size. The outlet is defined by station 4. The angle at the outlet is set to be 0 degrees in order to merge the flow that is attached to the cowling with the outflow of the duct. The set of equations that **TOS** uses to calculate the relative stack positions is listed in Table 3.3, with Equation 3.70 used to determine the nozzle mid-line angle $\phi_{noz}$.
In Figure 3.17, the generated shell clips the lower extremity of the HX and the lower nozzle wall, despite the vertical margin $z_m$ that is in place at station 3. This is not an issue as those parts are buried within the wall anyway. In all the OpenVSP models that **TOS** generated for this study, clipping of the upper part of the HX or duct never occurred. Remember the second design guideline brought up in subsection 3.4.1. In order to provide sufficient space for the refrigerant supply to the HX, a margin beyond the width of the HX needs to be put in place. This margin is denoted as $y_m$ and has a default value of 8cm, modifiable by the user. The vertical margin $z_m$ has a default value of 5cm and serves to provide sufficient space for any structural reinforcement of the installation needed between the duct, HX and the outer cowling. It should be noted that the values of these margins are not thoroughly substantiated and if a well defined HX is provided or to be analyzed, changing $y_m$ and $z_m$ to the known value is certainly recommended.

$$\phi_{noz} = \arcsin\left(\frac{(b + \frac{h_{out}}{2} - \frac{B_H}{2}cos(\theta + \phi))}{L_{noz}}\right) \tag{3.70}$$

**Table 3.3:** Duct station position inputs for the OpenVSP stacked geometry.

| | **1** | **2** | **3** | **4** |
|---|---|---|---|---|
| $\Delta x =$ | $-l_{lip}$ | $l_{lip}$ | $L_{diff}\cos(\phi) + \frac{B_D}{2}\cos(\phi+\theta)$ | $\frac{B_D}{2}\cos(\phi+\theta) + L_{noz}\cos(\phi_{noz})$ |
| $\Delta y =$ | 0 | 0 | 0 | 0 |
| $\Delta z =$ | 0 | 0 | $-\left[L_{diff}\sin(\phi) + \frac{B_D}{2}\sin(\phi+\theta)\right]$ | $L_{noz}\sin(\phi_{noz}) - \frac{B_D}{2}\sin(\phi+\theta)$ |

**Table 3.4:** Duct station cross section inputs for the OpenVSP stacked geometry.

| | $h =$ | $w =$ |
|---|---|---|
| **0** | $h_{in}$ | $w_{in}$ |
| **1** | $h_{in} + t_{lip}$ | $w_{in} + t_{lip}$ |
| **2** | $h_{in} + 2t_{lip}$ | $w_{in} + 2t_{lip}$ |
| **3** | $B_H\cos(\phi+\theta) + B_D\sin(\phi+\theta) + 2z_m$ | $B_W + 2y_m$ |
| **4** | $h_{out}$ | $w_{out}$ |

The diverter is modeled as a stacked geometry with 2 ellipses. The width of the ellipses should be around the width of the intersection line of the cowling and the wall and the depth should be around

two times the distance of that intersection line to the stack plane 2. The process of making the diverter is manual.
The subsurfaces on which the inflow and outflow are specified in the external aerodynamic analysis are defined under the ”Sub” tab in the geometry card in OpenVSP. They are simply defined as the area before section 0 for the inlet and after 4 for the outlet. In order to later identify these subsurfaces in the object files during meshing, they are given the intuitive names ”InletContour” and ”OutletContour”.

The model constructed in OpenVSP, which later on serves as a reference or base design, is depicted in Figure 3.18 in its take-off condition. An explanation of what the take-off and cruise conditions of the duct are, is provided in section 3.6. In order to generate a viable design, a system is first manually sized using DRAX, with the TMS critical operating condition as the starting point. In this case, it is assumed that the critical condition is at take off and that the system outputs 1MW of electrical power. If the resulting heat load is spread over two radiators, the $\dot{Q}$ per radiator is 461.5kW, assuming a fuel-cell efficiency of 52% [1]. An initial sizing using a FTHX core with a 50-50 water to ethylene-glycole mixture results in the core dimensions listed in Table 3.5 with the key duct dimensions noted along.
The inlet and outlet areas are assumed to have an aspect ratio of 4. The lip rise is set to 10 cm, since that is marginally larger than the estimated boundary layer thickness halfway down the Unifier19 fuselage, which represents a likely location for a fuselage bounded HX.

**Table 3.5:** The TMS input values and the accordingly sized FTHX dimensions for the base case with 1 MW power output.

| Symbol | Explanation | Value |
|---|---|---|
| **TMS inputs** | | |
| $P$ | Electrical output | 1 MW |
| $n_{HX}$ | Number of HX | 2 |
| $\dot{Q}$ | Heat rejection per HX | 461.5 kW |
| $T_{ref,i}$ | Refrigerant inlet temperature | 100 °C |
| $p_{ref,i}$ | Refrigerant inlet pressure | 2 bar |
| $\dot{m}_{ref}$ | Refrigerant mass flow rate | 8.3 kg/s $\equiv$ 492.3 l/min |
| $h_{TO}$ | Take-off altitude | 0 ft |
| $T_{off}$ | Atmospheric temperature offset | +15 °C |
| $V_{TO}$ | Take-off speed | 54.5 m/s |
| **FTHX dimensions** | | |
| $B_D$ | FTHX core depth | 0.15 m |
| $B_W$ | FTHX core width | 1.00 m |
| $B_H$ | FTHX core height | 0.712 m |
| $n_{tubes}$ | Number of parallel tubes | 64 |
| $\theta$ | Flow relative HX inclination | 65 ° |
| **Duct dimensions** | | |
| $h_{lip}$ | Lip rise; diverter height | 0.1 m |
| $A_{in}$ | Inlet area | 0.152 $m^2$ |
| $A_{out}$ | Outlet area | 0.3344 $m^2$ |
| $L_{diff}$ | Diffuser length | 1.5 m |
| $L_{noz}$ | Nozzle length | 2 m |
| $L_{duct}$ | Total duct length (external) | 3.55 m |
| $b$ | Burial depth | 0.1 m |

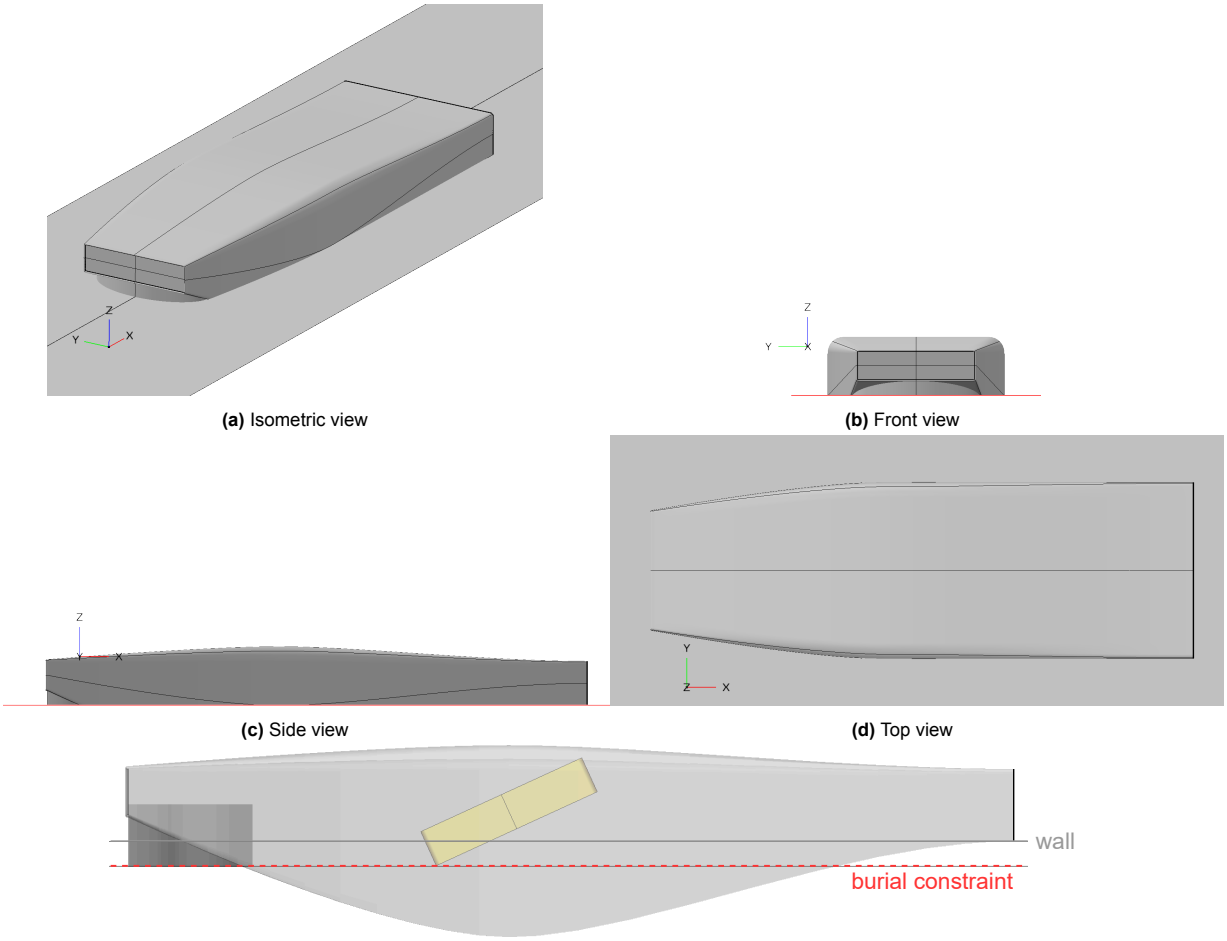


**(a)** Isometric view

**(b)** Front view

**(c)** Side view

**(d)** Top view

**(e)** Hollow side view with slanted HX

**Figure 3.18:** The reference base duct that is used later on, as it is modeled in OpenVSP. Sized for a 1MW power output fuel cell, requiring 461.5kW heat rejection per 2-split radiator.

## 3.5. External Drag

What sets the drag estimation model presented in this work apart from existing models is the attempt to more accurately and also variably compute the external drag. Existing studies that implement an external model use invariable drag coefficients [21, 22] generated for radiator housings of a much smaller scale [23], in particular WW2 piston engine fighters, as their designers were largely occupied with dissipating the heat of their large, powerful but inefficient engines.

Although the lessons learned from that era still hold value, the problem faced today by FC- and battery electric aircraft has another dimension - literally. The envisioned HX installations bear little resemblance to the intercooler on a P-51 Mustang or the Bf-109. In fact, one estimate in the Unifier19 study puts the required combined (for all power electronics) HX frontal area at 2.07 $m^2$ [1]. Figure 3.19 illustrates how large the combined HX frontal area is in relation to the fuselage. As the figures in section 3.4 show, the HX cannot simply be buried anywhere in the fuselage but must be integrated such that a uniform air supply can be established, necessitating space for the diffuser and the outlet nozzle. The resulting cowling is expected to generate an amount of parasitic drag, that should not be underestimated but accurately represented by means of simulation.

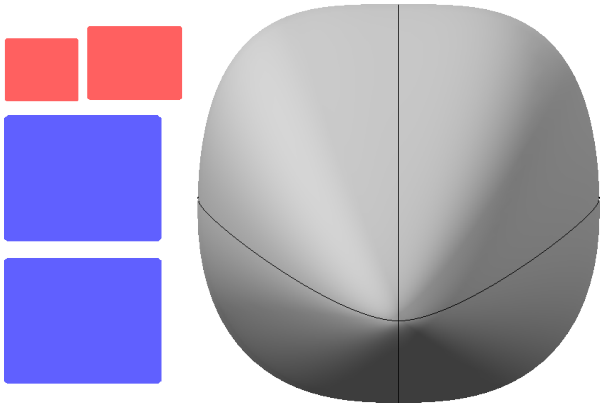

**Figure 3.19:** The Unifier19 DEP fuselage from the front with the HX frontals next to it. Blue for FC TMS; Red for main electric powertrain TMS. Values taken from Unifier19 final report [1]. Figure produced in OpenVSP.

A wide choice of simulation tools was considered in order to compute the external drag. *Pipistrel*, being a stakeholder of this thesis, urged for the use of open-source software only. Simultaneously, a tool that strikes a compromise between easy use, low computational cost and an appropriate level of accuracy is required by the student. A list of contenders, considered in the final selection is provided below. In the end, the choice fell on OpenFoam. Less so out of a particularly strong desire to work with the software but rather because the other options incurred a disqualifying argument or were deemed too unhandy to work with.

- **VSPAero**: OpenVSP contains its own aerodynamic solver, VSPAero. The panel method is handy to use and would allow for a fast analysis of the model, minimizing overhead as everything is integrated in OpenVSP while solving the flow quickly. Unfortunately, this option was discarded as there is no way to impose boundary conditions for the inlet and outlet of the duct, essentially modeling 100% spillage at the inlet, distorting the results.
- **Cart3D:** This is an high-fidelity inviscid CFD analysis tool, developed by NASA. There are examples of it being used in combination with OpenVSP, also developed by NASA, in order to impose inlet and outlet conditions on engine ducts. Cart3D is only available with a license, which is not distributed to users outside the United States of America. Hence, it is discarded.
- **VSAero:** Not to be confused with VSPAero from above, VSAero is another software, which combines potential flow with boundary layer models. It seemingly allows for manually imposed boundary conditions for in- and outflow. However, it is dated and has less documentation than more recent software. Therefore, it is a less preferred option.
- **PANAIR:** Another panel aerodynamic solver, initially considered attractive due to the low computational cost, discarded rather quickly as it is antiquated.
- **MachLine:** Developed as a modern implementation of PANAIR, this tool offers more user friendliness. However, it is not widely used, particularly not for the needed application. Hence, its validity is hard to substantiate.
- **FlightStream:** A very attractive panel solver with proven use and available documentation. It is, however, only available under paid license and thus discarded.
- **OpenFoam:** Very versatile open-source CFD software with many different solvers, integrated meshing, an extensive up-to-date documentation and a large community. Being a finite volume method, it is more computationally expensive than a panel method but it allows for the implementation of inlet and outlet boundary conditions.

The method employed to determine the external drag component with the simpleFoam Reynolds Averaged Navier-Stokes (RANS) simulation within OpenFoam is presented in the following sections. First, the computational domain and the creation of a computational mesh are summarized along with the imposed boundary conditions in subsection 3.5.2. Thereafter, subsection 3.5.4 presents the choice of the specific solver within OpenFoam along with some more detailed settings to make the simulation run and extract the desired results. Lastly, this section presents a key aspect of this work, namely the

development of a surrogate model, which emulates the CFD results at a much lower computational cost.

### 3.5.1. Assumptions

Several assumptions are made in the external drag analysis. They are mentioned and defended throughout the following subsections but separately stated here for clarity. First, and most importantly, flow interferences of other parts of the aircraft are neglected. This means that the duct cowling is resolved independently of the effect of the fuselage on the flow and does not account for any boundary layer generated by other bodies.
Due to the choice of the flow solver, the flow is assumed incompressible and adiabatic in the simulations. The temperature increase of the outlet flow is also not recognized due to the limitations posed by simpleFoam.
Lastly, the far field flow is always assumed to be perfectly aligned with the duct axis, neglecting any effects that the angle of attack or the yaw angle might have in flight.

### 3.5.2. OpenFoam: Meshing

By nature, running a successful simulation in a finite volume solver, such as OpenFoam, depends on the quality of the mesh. Particularly when assessing forces on a body, if one starts off with a bad mesh, one might as well guess the result of the simulation. This subsection will focus on 3 key aspects of meshing - the computational domain, the refinement zone and the wall inflation layers.

The far field domain can be described as the box that surrounds the body of interest within it. Smartly choosing what to resolve within the domain can save many hours of computational effort. A progression of what is analyzed within the performed simulations is depicted in Figure 3.20. Initially including the full fuselage and ducts (red in Figure 3.20), the domain can be minimized by only resolving one half of the body. Dividing the model and imposing a symmetry boundary condition on the splitting plane effectively halves the computational domain (orange in Figure 3.20). For the purpose of this study, resolving interaction effects between the duct and other parts of the aircraft - mostly the fuselage - is deemed superfluous given its disproportionate computational penalty. Thus, the model is simplified to a wall-bound duct (green in Figure 3.20), as it presented in section 3.4, particularly subsection 3.4.2. The duct in turn is again split along its plane of symmetry with a symmetry boundary condition. Since no transient asymmetric aerodynamic phenomena, such as vortex shedding, are expected or resolved, this split is sensible.

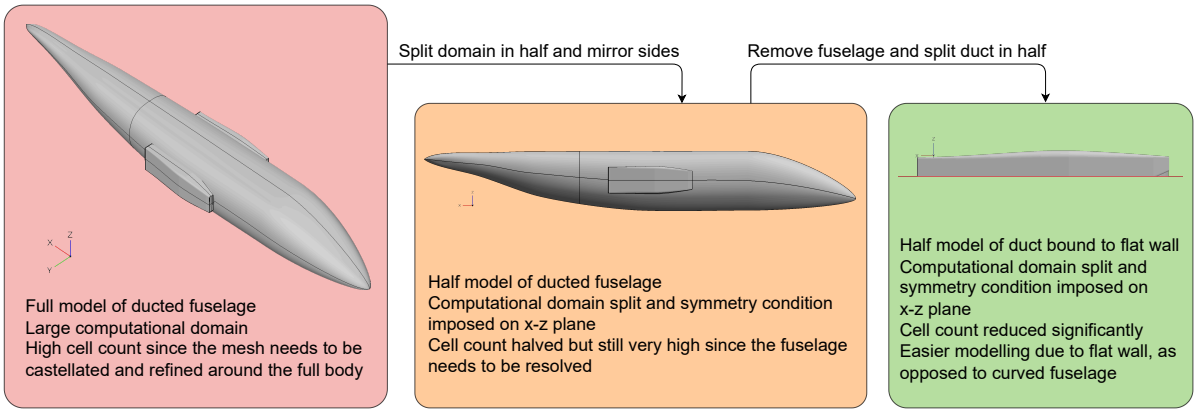


**Figure 3.20:** The progression of the computational domain from full ducted fuselage to the wall bound duct.

The mesh is generated in 3 steps that each focus on one of the meshing aspects noted in the leading paragraph of this subsection. First, the computational domain is generated with the *blockMesh* function in OpenFoam. Thereafter, the refinement regions and the duct are resolved with the *castellatedMesh* functionality in *snappyHexMesh* (SHM). Lastly, SHM is used once more with the *addLayers* functionality turned on in order to control the $y+$ values on the duct.

The far field domain is sized according to the duct dimensions of the reference model depicted in

Figure 3.18. It needs to be large enough to leave space for pressure fluctuations to dampen out and not oscillate and diverge. On top of that, the wake region of the duct must be large enough before hitting the boundary condition at the domain outlet, that is the downstream wall of the domain, not the duct outlet.
Figure 3.21 shows the dimensions of the farfield domain. The domain is sized according to the duct dimensions, with all the farfield dimensions being a multiple of the duct length $L_{duct}$. By far the largest dimension is in the flow direction, with a wake region extending to roughly 12 times the duct length, or 40 meters. The upstream length, as well as the height and width of the domain are roughly 6 times the duct length, or 20 meters. These lengths are more than sufficient, given that the duct has little effect on the flow field in the z and y directions. The far field cells have a unit size of 1 cubic meter. This is particularly handy when applying mesh castellation in SHM, as the base cells are halved per refinement level, thereby making the cell size for a given refinement level easy to calculate.

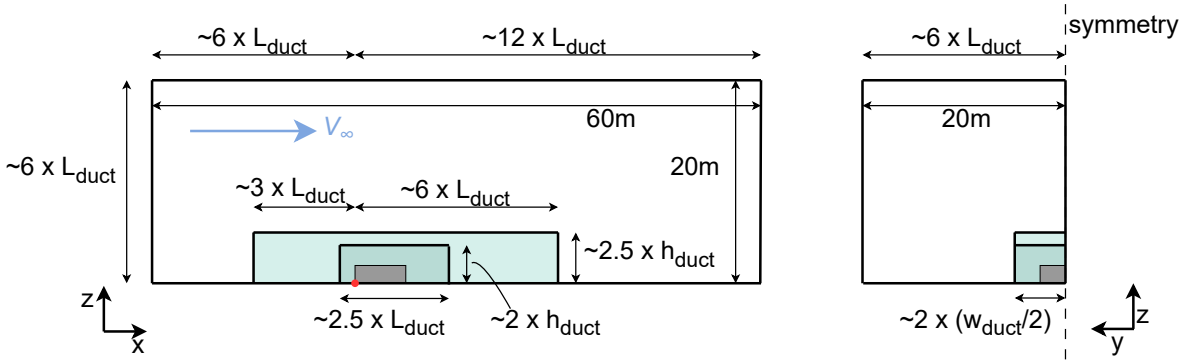


**Figure 3.21:** The computational far field domain with the two refinement regions (blue-green) surrounding the duct (gray). The red dot represents the origin of the domain as well as of the duct. The reference dimensions are $L_{duct}$=3.55 m, $h_{duct}$=0.38 m, $w_{duct}$=0.58 m

The far field domain generated in Figure 3.21 already shows the presence of a refinement region surrounding the duct. This refinement region is specified in SHM as a box with chosen refinement level under the *refinementRegions* sub-dictionary. The outer box is given a refinement level of 4 and the inner box a refinement level of 5. Hence, the cubic cells in the outer box have an edge length of $6.25cm$ while the ones in the inner box are refined to $3.125cm$. As a side note, the refinement is not abrupt, but gradual and such that the specified refinement leads up to the borders of the refinement box. That means that at the border of the outer box, refinement level 4 is already reached.

The cell refinement at the surface is achieved by first refining the surface during castellation and then adding layers. Object surfaces can be prescribed a distinct refinement level in the *refinementSurfaces* sub-dictionary in SHM. After testing, a uniform refinement level of 8 over the surface has been deemed the best, as it allows the mesh to resolve the duct sufficiently well while keeping the cell count within reason. At a refinement level of 8, features are resolved with an accuracy of $3.9mm$. At the inlet lip, this leads to a rather choppy mesh. However, a higher refinement incurs two problems; If applied over the entire duct surface, it unreasonably increases the computational effort and, if applied locally (only the lip region), it leads to issues with collapsing cell layers in the inflation layer process down the line. After the mesh castellation and initial surface refinement is performed with SHM, the *addLayers* functionality in SHM is applied over the output mesh. This move could theoretically be combined into a single execution of SHM. The decision was, however, actively made to run SHM on two separate occasions in order to apply different mesh quality constraints for the castellation and layer addition processes. The cells generated by SHM need to have a sufficiently low thickness, as they need to be in a certain range of $y+$ values. This tends to generate very flat cells with a high aspect ratio which would fail the quality constraints put in place for mesh castellation and thus not be generated. Other quality constraints, such as the maximum non-orthogonality of cells also need to be relaxed when adding layers. With this strategy, a high quality castellated mesh as well as full coverage of the body with inflation layers can be ensured.

If one seeks to achieve the best level of accuracy for the RANS simulation, the large velocity gradients within the boundary layer need to be resolved. For this, the wall-bound cell should be sized such that a $y+$ value of 1 is obtained. In the given simulation, this would require a cell thickness on the nanometer scale. Besides demanding a very large number of layers near the wall to ensure that the cell size difference from the inflation layer to the castellated mesh is not too abrupt, this is also practically impossible to uniformly achieve with SHM, which frankly tends to do a poor job at applying thick and uniform inflation layers. At this point, the use of a wall function is very attractive as it can model the near-wall region with $y^+ > 1$ at a low computational cost.
To summarize the law of the wall, the boundary layer can be divided into three regions - the viscous sublayer, the buffer layer and the log-law region. The viscous sublayer extends from $0 < y^+ < 5$ and describes the part near the wall, where viscous effects dominate. The velocity profile within the viscous sublayer is linear. The log-law region is typically recognized to extend from $30 < y^+ < 300$ and is the part within the boundary layer, where the aforementioned law of the wall holds, meaning that the velocity profile follows a logarithmic shape. The upper limit of 300 is widely used as a rule of thumb in CFD but technically, the upper limit of the log-law region is $Re$-dependent. Situated inbetween is the buffer layer ($5 < y^+ < 30$), where neither law is applicable and applying one or the other leads to considerable error.
The most convenient solution is to use a wall function that is applicable throughout the three regions of the boundary layer. Spalding [47] devised a single formula for the law of the wall, which holds for $0 < y^+ < 300$. Figure 3.22 shows the law of the wall described above and the Spalding wall function within it. Assuming that the results from direct numerical simulation (DNS) are ground truth, Spalding's wall function represents the flow very well.

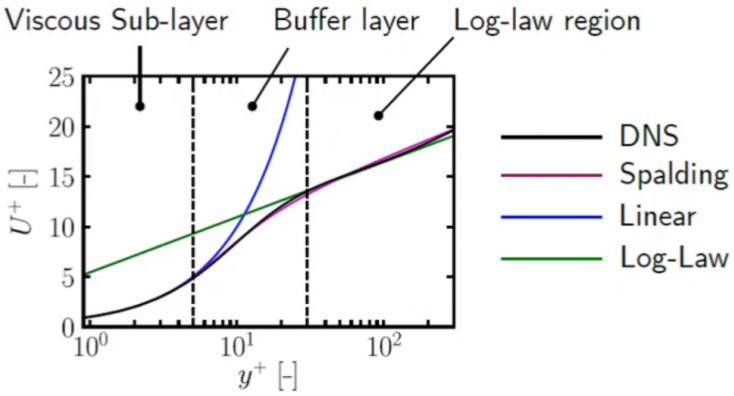


**Figure 3.22:** The three sublayers of the boundary layer. The Spalding wall function closely follows results obtained by direct numerical simulation (DNS) throughout $0 < y^+ < 300$. Figure taken from [48].

With the wall function chosen, the dimensions of the inflation layers can be defined. Using Spalding's wall function, the goal is to keep the $y^+$ value on the duct surface within $1 < y^+ < 300$. As was already explained, SHM does a poor job at applying a uniform inflation layer which is why, to be sure, a mean $y^+$ of around 150 is aimed for. The height of the wall bound cell $y$ is calculated by Equation 3.74 with the Schlichting skin-friction coefficient $C_f$, the wall shear stress $\tau_w$ and the friction velocity $u_*$. $Re$ uses $L_{duct}$ as the characteristic length, here.

$$C_f = [2\log_{10}(Re) - 0.65]^{-2.3} \tag{3.71}$$

$$\tau_w = C_f \cdot \frac{1}{2}\rho V_\infty^2 \tag{3.72}$$

$$u_* = \sqrt{\frac{\tau_w}{\rho}} \tag{3.73}$$

$$y = \frac{y^+ \mu}{\rho u_*} \tag{3.74}$$

Using take-off conditions for the reference case, a cell height $y$ of 1.2 mm is chosen which leads to a $y^+$ of 153. With the near-wall mesh consisting of 6 layers at an expansion rate of 1.2 in between, the last cell of the inflation layer has a thickness of 3 mm. This is conveniently close to the 3.9 mm cell dimension resolved by the surface refinement during castellation, which leads to a smooth transition in the mesh from the inflation layer to the castellated mesh.

### 3.5.3. OpenFoam: Boundary Conditions

The boundary conditions of the domain are recorded in Figure 3.23. The top and distant side bounds of the domain are specified to be slip walls, hence frictionless walls. In a smaller domain, one could expect this to lead to blockage effects, such as in wind tunnels, but the bounds are considered far enough that the walls have no effect on the forces acting on the duct.
More open for discussion is the implementation of a slip wall on the bottom of the domain, which is the wall to which the duct is bound. Looking back to Figure 3.20, the duct is initially expected to be fuselage bound. In that light, it would be sensible to reflect the effect that the fuselage boundary layer has on the duct by implementing a no slip wall in a zone surrounding the duct. Admittedly, this would be beneficial for the quality of the results for a specific fuselage bound duct. However, it can be assumed that the length of the fuselage (here Unifier19) is at least 5 times the length of the duct. In order to resolve the fuselage boundary layer effects, a thick inflation layer would therefore need to be applied over an area, that is large in comparison to the duct. The increased computational cost that arises from this addition of cells in the domain is considered disproportionate to the expected insights that the simulation exposes on duct-fuselage interaction. Beyond that, constricting the tool to only ducts bound to a fuselage at a certain distance from the nose could be viewed as a disadvantage.
The duct surface is naturally specified as a no slip wall. At the duct inlet and outlet, a fixed value boundary condition for the velocity is imposed which is generated with the internal model outputs of **DRAX**.
The domain inlet is given the velocity and pressure that are associated with the ambient, hence at the imaginary point $\infty$. The velocity at the domain outlet is not specified and left as an *inletOutlet* type boundary condition prohibiting backflow, which stabilizes the simulation from initial large fluctuations. The pressure boundary condition at the outlet is specified as a *zeroGradient* type, assuming that the wake has stabilized downstream.
Note that when referring to pressure in simpleFoam, in fact the density-normalized pressure with units [$m^2/s^2$] is meant. Throughout the domain, the actual pressure is normalized by the ambient density $\rho_\infty$.

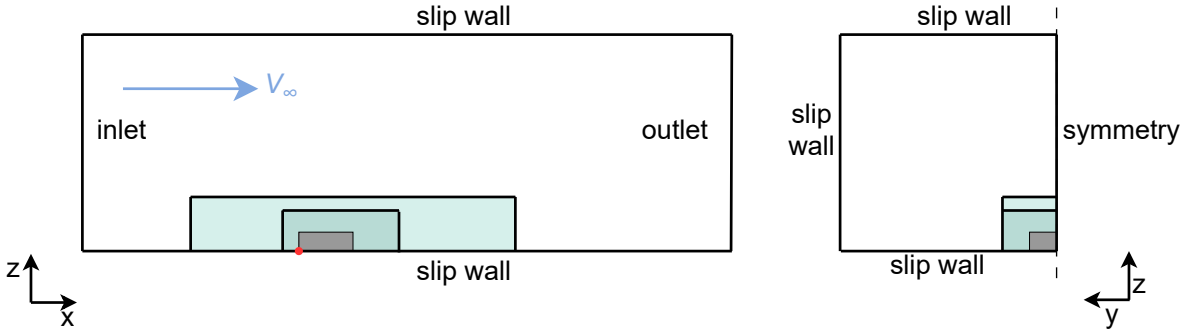


**Figure 3.23:** The boundary conditions of the simulation domain.

### 3.5.4. OpenFoam: Solver

As mentioned before, the simulations were performed with simpleFoam, an incompressible RANS solver. While the use of a compressible solver, such as rhoSimpleFoam would have been attractive as it could reflect the change in temperature of the air going through the duct, initial use of it was unsuccessful due to diverging pressure oscillations within the computational domain. The disregard of compressibility effects is however, not too detrimental, since the duct outlet air only affects the wake and the reference case aircraft provided by *Pipistrel* is expected to operate at the bound of the incompressible flow regime $M \leq 0.3$.
Within simpleFoam, the $k-\omega$ SST turbulence model developed by Menter [49] is used. This model has good flow separation prediction, which is interesting if the analyzed duct has a large hump, for instance due to a low inclination angle of the HX and if the duct nozzle is in a closed position, a state that will be explained in section 3.6. Additionally, it is rather inexpensive being a 2-equation model. [50]

The pressure component of the drag force on the duct is used as the convergence criterion. Once the average force over a range of preceding timesteps is within a certain deviation limit, the simulation stops.

This limit is set to a cumulative deviation of 0.1% over 10 preceding timesteps. A typical convergence history for the duct drag force is shown in Figure 3.24. It shows that the duct drag force is stable already before the convergence criterion is fully met.

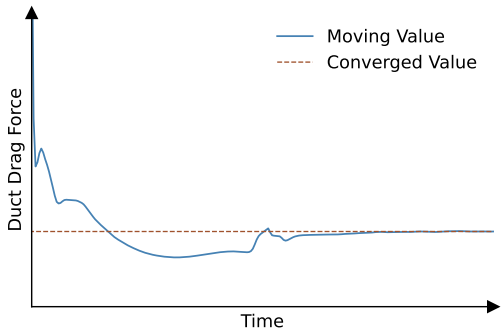


**Figure 3.24:** The typical convergence history of the external duct drag recorded during the simulation.

When assessing the force acting on the duct, the OpenFoam *forces* function is used. Importantly, the case that is being analyzed is quite special in that the value of the reference pressure $p_{ref}$ must be specified and cannot be assumed to be 0, which is the default. There are only two cases in which the reference pressure must be altered. One case is if the solver used is compressible (e.g. rhoSimpleFoam) and another, badly documented, case is if the the analyzed body is not closed. The latter applies to the duct, as the duct inlet and outlet are not part of the surface over which the force is assessed. Thus, the duct cowling is a hollow shell. The pressure differential between the inlet and the outlet is part of the internal model, which is already accounted for by **DRAX**.

### 3.5.5. Surrogate Model

Section 3.6 goes into how **DRAX** can be used to generate optimal duct and HX designs for given mission profiles and heat loads. In order to recurringly fetch values for the external drag of a particular duct design at a specific spillage rate $SR$ at the duct inlet, a surrogate model for the external drag must be established as running a CFD simulation for each iteration is unacceptably slow. Be aware that the time to obtain a converged solution for the reference case takes nearly 3 hours on a capable and top-of-the-line new workstation. This runtime may vary depending on the size of the duct since a smaller duct cowling can be resolved with fewer cells. Nevertheless, the order of magnitude of the runtime of simpleFoam cannot be radically reduced.

The aim of the surrogate model is to project the external drag of a duct centered around a base case that can already be considered well designed. Thereby, the effect of small design changes on the external drag can be predicted sufficiently well by polynomial interpolation and extrapolation. On top of that, the base case is modeled under different $SR$ to factor in the impact of spillage and the resulting lip suction effect.

Thus, the surrogate model is expected to output an external drag value $D_{ext}$ for an input of duct design parameters and $SR$. It is not simply possible to feed a CAD drawing into a function. Instead the duct design is first parametrized and normalized in order to make different designs comparable to each other. Choosing which design parameters are defining the duct is tricky but initially, an approach similar to airfoil design parametrization can be applied. Thereby, the thickness-to-chord ratio of an airfoil $(t/c)$ can be compared to the ratio of the protrusion height of the duct $h_{max}$ to the duct length $L_{duct}$. Likewise, the chordwise position of the maximum thickness $(x_t/c)$ can be compared to the ratio of the length of the frontal section of the duct $L_f$, leading up to $h_{max}$, over the duct length $L_{duct}$.

More duct-specific comparability parameters relate to the ratios of the lip rise $h_{lip}$ and the height of the outlet $h_{out}$ to the protrusion height $h_{max}$. The former quantifies the effect that the diverter has on the drag while the latter can be used to assess the drag for different nozzle opening states. The 4 comparability parameters are defined and listed beside Figure 3.25.

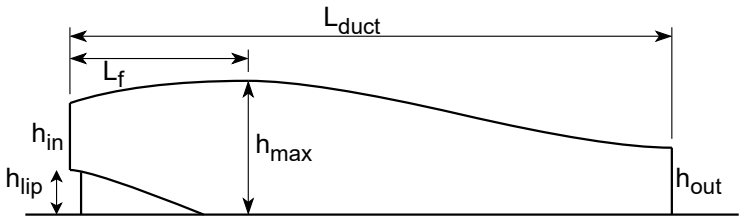


**Figure 3.25:** A simplified figure of the duct cowling with the relevant design parameters used in the surrogate model.

The strategy for calculating $D_{ext}$ of a duct cowling is to first divide the external drag into its two contributions - the pressure drag $D_{press}$ and the viscous drag $D_{visc}$. The factor $f_{spill}$ is then applied to the sum of $D_{press}$ and $D_{visc}$. Shown in Equation 3.76, $D_{press}$ is assumed to scale with the projected frontal area of the duct $A_{max}$ and a design-sensitive pressure drag coefficient $C_{D,press}$, as well as the dynamic pressure $q$. The viscous drag $D_{visc}$ in Equation 3.77 scales with a friction coefficient $C_f$ and the wetted area of the duct $A_{wet}$, along with $q$.

$$D_{ext} = f_{spill} \cdot (D_{press} + D_{visc}) \tag{3.75}$$

$$D_{press} = C_{D,press} \cdot q \cdot A_{max} \tag{3.76}$$

$$D_{visc} = C_f \cdot q \cdot A_{wet} \tag{3.77}$$

The variation of the pressure drag coefficient $C_{D,press}$ for a specific design is quantified in a one-factor-at-a-time approach. Thereby, the effect of each comparability parameter from above is assessed in isolation from varying other parameters. This is not ideal since there are almost certainly combined effects of varying multiple parameters simultaneously. However, a multi-variate approach requires much more data.

To make the point clearer; here, the effect of increasing and reducing each comparability parameter by a certain amount is assessed. Hence, for each comparability parameter, at least 2 variations are added around the median point adding up to 3 test points per parameter. If one wants to cross-test all the comparability parameters and generate a complex model that captures interference effects between comparability parameters, with 4 parameters one needs to test $3^4 = 91$ ducts. Given that the simulation time of the base duct is nearly 3 hours, this is unreasonable not only within the given timeframe, but also for the desired level of accuracy. Also keep in mind that a one-factor-at-a-time approach already represents a significant improvement from existing drag models, presented in chapter 2. The total number of test points needed for the chosen approach is 9, counting in the base duct. Thus, a tenth of the computational cost of the multi-variate alternative. On top of that, 3 more simulations are run to quantify the spillage effect.

In conclusion, each factor $f$ in Equation 3.78 quantifies the variation of one of the comparability parameters away from the base design, with pressure drag coefficient $C_{D,press,base}$.

$$C_{D,press} = C_{D,press,base} \cdot f_1 \cdot f_2 \cdot f_3 \cdot f_4 \tag{3.78}$$

The friction coefficient $C_f$ is assumed to be constant for all designs. However, the wetted area $A_{wet}$ cannot be assessed as easily as $A_{max}$, which can be found with **TOS**, under the assumption that station 3 in the stack geometry is where the largest cowling cross-section is found. To find the wetted area of the duct, the mesh surface of the duct in OpenFoam is determined with the surface integration tool in ParaView. Then, it is sought to derive $A_{wet}$ from $A_{max}$ via a transformation factor. It was found that ratio of $A_{wet}$ to $A_{max}$ only noticeably changes with the variation of one parameter, that is $(h_{max}/L_{duct})$. Therefore, a single transformation factor $f_A$ is used to derive $A_{wet}$ as in Equation 3.79.

$$A_{wet} = A_{max} \cdot f_A \tag{3.79}$$

A duct generator function, essentially **TOS** in reverse, generated the test ducts with the comparability parameters listed in Table 3.6. The variations from the base value were generally sought to amount to $\pm 30\%$. Needless to say, there are cases where varying the parameter to this extent leads to insensible designs. For instance, lowering the $(h_{max}/L_{duct})$ by 30% generates a duct with a slumped back, which

wouldn't make sense. Likewise, it was decided to cap the increase in $h_{out}$ to the value of $h_{max}$. For the diverter height, instead of lowering $h_{out}$ by 30% it was decided to test a case where the diverter is removed altogether and the lower lip is buried into the wall.

**Table 3.6:** The comparability parameter values of the base duct and the 8 variations, with their individual tag.

| Parameter | Smaller | Base | Larger | Factor |
|---|---|---|---|---|
| $(h_{max}/L_{duct})$ | 0.083 *Var1* | 0.108 | 0.144 *Var2* | $f_1$ $f_A$ |
| $(L_f/L_{duct})$ | 0.284 *Var3* | 0.43 | 0.572 *Var4* | $f_2$ |
| $(h_{lip}/h_{max})$ | 0 *Var5* | 0.259 | 0.493 *Var6* | $f_3$ |
| $(h_{out}/h_{max})$ | 0.496 *Var7* | 0.752 | 1 *Var8* | $f_4$ |

Figure 3.26 depicts the base duct, described by the center column of Table 3.6 from the side. The eight variations are shown from the same view in Figure 3.27.

**Figure 3.26:** The base duct viewed from the side.

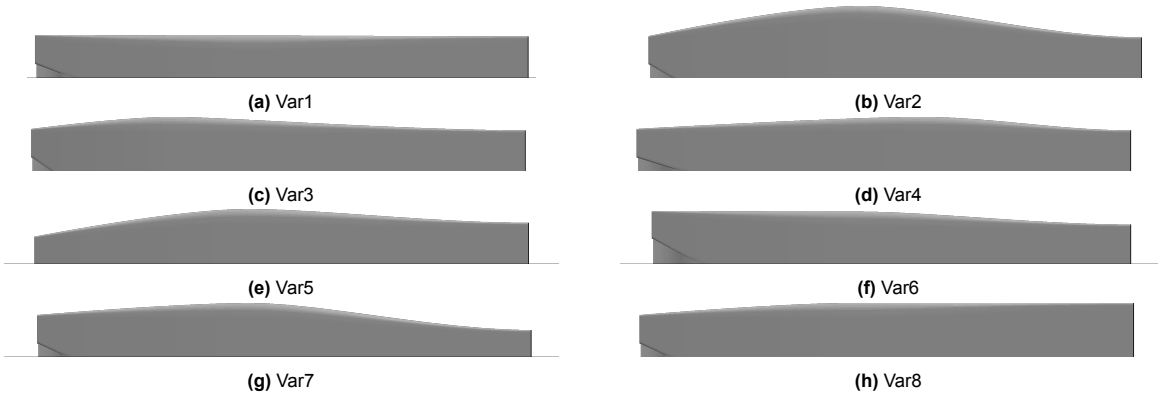


**Figure 3.27:** The design variations of the base duct, noted in Table 3.6, viewed from the side.

The data for the design variations was simulated for the take-off condition under the assumption of incompressible flow $M_{TO} = 0.16$ and a very small spillage of 2.5%. The various factors used in the surrogate model for Equation 3.78 and Equation 3.79 are plotted in Figure 3.28. Alongside, the second y-axis in Figure 3.28a, Figure 3.28b and Figure 3.28c shows the total external drag at take-off. In the generated results, no significant variation in drag between the base case and *Var3* and *Var4* was found, which is why $f_2$ is dismissed.
The interpolation function for $f_1$ is a cubic spline with clamped linear extrapolation (1st order derivative is 0) upwards and natural linear extrapolation (2nd order derivative is 0) downwards. As can be seen in Figure 3.28a, the trends for $C_{D,press}$ and $D_{ext}$ are not alike. That is because a larger protrusion height $h_{max}$ leads to a larger frontal area $A_{max}$. In this case, when increasing $h_{max}$, $A_{max}$ increases proportionally faster than $D_{ext}$ meaning that the drag coefficient goes down while the actual drag rises. Thus, the choice to clamp the boundary condition upwards does not mean that drag no longer rises when $(h_{max}/L_{duct})$ is increased but that the further rise in drag is attributed solely to the increase in the frontal area.
Surprisingly, the effect of the diverter height in Figure 3.28b appears nearly perfectly linear. Therefore,

the function for $f_3$ is a linear least squares function.
The remaining factor of Equation 3.78, $f_4$, is shown in Figure 3.28c. The interpolation function is a cubic spline with a clamped boundary condition (1st order derivative is 0) upwards and natural linear extrapolation (2nd order derivative is 0) downwards. A ratio $(h_{out}/h_{max})$ larger than 1 is not sensible, therefore the function is not further extended and it is assumed that the factor $f_4$ levels off at that point. In duct designs where the outlet height is higher than the height of the protrusion at station 3 in the geometry, this protrusion height is made to match $h_{out}$ such that $(h_{out}/h_{max})$ is 1 at most.
At last, the ratio of wetted area to frontal area $f_A$ is plotted in Figure 3.28d. The interpolation function is a least squares power curve fit which is extrapolated in both directions.

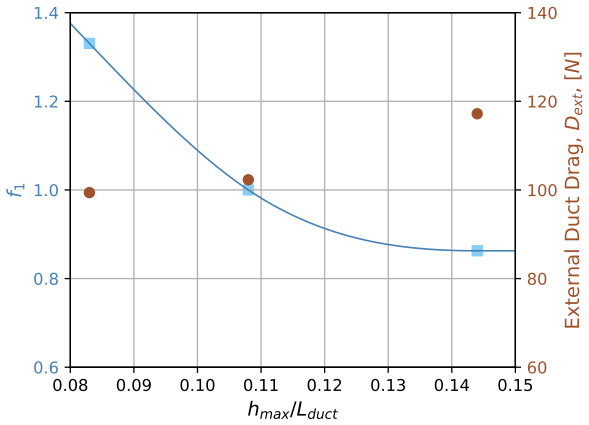


**(a)** Factor $f_1$, describing how the pressure drag coefficient changes with $(h_{max}/L_{duct})$.

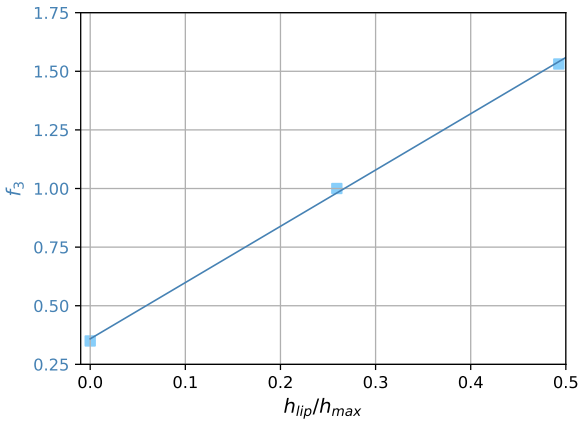


**(b)** Factor $f_3$, describing how the pressure drag coefficient changes with $(h_{lip}/h_{max})$.

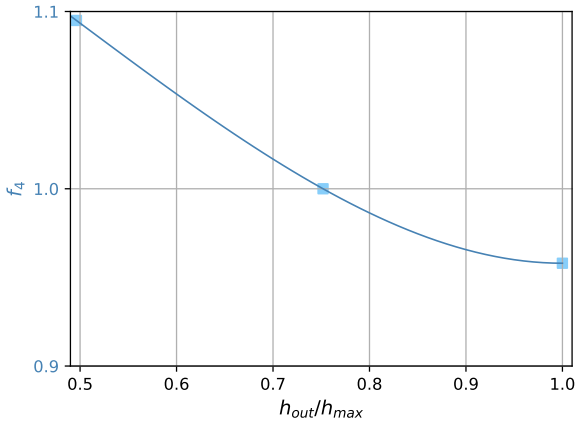


**(c)** Factor $f_4$, describing how the pressure drag coefficient changes with $(h_{out}/h_{max})$.

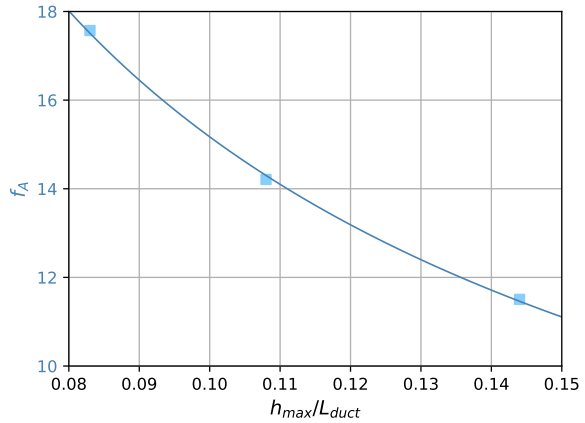


**(d)** Factor $f_A$, describing how the ratio of wetted area to frontal area scales with $(h_{max}/L_{duct})$.

**Figure 3.28:** The factors used to determine the pressure drag coefficient $C_{D,press}$ and the wetted area $A_{wet}$ of a duct design. The center point in the plots relates to the base design.

The factor $f_{spill}$, accounting for the lip suction effect is presented in Figure 3.29 and fitted with a second order polynomial. The variation is stark but the magnitude to which it acts is supported by literature [51, 15, 52] and will be revisited in chapter 5. It would be recommended not to apply this factor above spillage rates of 75% because the lip suction effect is likely to stagnate or even collapse at very excessive $SR$. In fact, the results show that these very high spillage rates do not occur within the tested boundaries of the tool, given that spillage is limited by how much air needs to be taken in to match the required heat transfer. Nevertheless, the polynomial curve of $f_{spill}$ is extended up to $SR = 100\%$ for lack of a better assumption at the present stage.

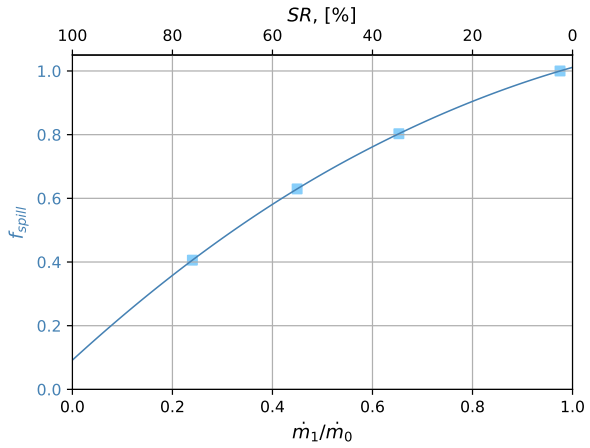


**Figure 3.29:** Factor $f_{spill}$, describing how the external drag changes with $SR$.

## 3.6. Design by Optimization

This last methodology section revolves around the use of an optimization algorithm to obtain a ducted ram-air HX design with the least cooling drag. For this, a sensible set of design variables is needed, the choice of which is elaborated in subsection 3.6.1. Section 3.6.2 looks at the constraints that are put in place to ensure a sensible design. Thereafter, the different points in a critical mission profile are observed to avoid oversizing or undersizing the system. Section 3.6.3 and subsection 3.6.4 show precisely how the take-off and cruise conditions are used as design and off-design conditions in this procedure. Finally in subsection 3.6.5, the various pieces are visually put together into an extended design structure matrix (XDSM) and the choice of a differential evolution optimization algorithm is defended.

### 3.6.1. Design Variables

The design variables are combined into a design vector $\vec{x}$, where each design variable represents one entry. If the problem is non-linear, the number of design variables can have a large influence on the time that it takes the optimization algorithm to converge. This should be at the back of ones mind when choosing the scope of the optimization.

Under consideration of the above-mentioned and, perhaps more importantly, remembering the research questions 1, 5 and 6 formulated in chapter 2, the choice is made not to focus on detailed HX design parameters or details pertaining to the design of the duct. To keep it simple, $\vec{x}$ only includes the block dimensions of the HX ($n_{pass}$, $B_D$, $B_W$) and its tilt angle $\theta$, as noted in Equation 3.80. The duct is sized as a consequence of the HX at the sizing criterion. Detailed design parameters of the HX such as the fin pitch and material thicknesses or even louver design features for the FTHX are taken from industry standards and papers.

$$\vec{x} = \begin{pmatrix} n_{pass} \\ B_W \\ B_D \\ \theta \end{pmatrix} \tag{3.80}$$

### 3.6.2. Design Constraints

There are several design constraints connected to the ducted ram-air HX. Some, such as the burial depth $b$ and the diffuser ramp angles $\alpha$ and $\alpha_{upper}$ are already implemented in **TOS**. One constraint that can have a big impact on TMS operation is the refrigerant pressure drop through the HX $\Delta p_{ref}$, discussed in subsection 3.3.2. A larger pressure drop results in more pumping power in the TMS, which increases both power consumption and can lead to requiring a larger pump, incurring more carried mass. A design that reduces cooling drag slightly but increases pumping power disproportionately is not actually better. Therefore, capping the refrigerant pressure drop to a certain value is important.

The refrigerant in a LCS is generally pressurized between 2-3 bars. Following design requirements set up by *Pipistrel*, the maximum refrigerant pressure drop is capped to 10% of the inlet refrigerant

pressure. If surpassed, the constraint is enforced by raising a disproportionately large drag penalty ($10^6$ N) in the evaluation of the cruise criterion.

### 3.6.3. Sizing Criterion: Take-Off

The two points of interest for designing and assessing the ducted ram-air HX in the typical mission profile of an aircraft are at take-off and during cruise. For this, *Pipistrel* has provided an exemplary mission profile of a 1 MW system that was used when sizing the base duct in subsection 3.4.2 and generating the surrogate model in subsection 3.5.5. View Table 3.5 to see the TMS inputs.
It is assumed that for a FC, which would generate the main heat load for a TMS, the power output and therefore also the heat output is constant throughout the mission. Since the environmental conditions change between take-off and cruise, there is however a difference in the amount of heat that the exact same installation would reject, unless a regulating mechanism is put in place. From the HX point of view, one option would be to lower the pumping speed of the refrigerant. However, the refrigerant mass flow rate $\dot{m}_{ref}$ is not dictated by the HX but by the heat source and must, as was alluded to above, remain constant within the mission.
The other option, which is the chosen one, is to regulate the air mass flow rate $\dot{m}_{air}$ by reducing the outlet area of the duct in cruise and thereby actively spilling air at the inlet. Go to subsection 3.3.4 to refresh on that topic.
The most critical point within the mission regarding cooling is assumed to be take-off since the airspeed is low, leading to lower $\dot{m}_{air}$ and the temperature gap between the refrigerant and the cooling air is also lowest. Therefore, it is assumed that at take-off, no air shall be spilled to ensure that the inlet runs at its maximum capacity. Thus, the outlet nozzle can be sized using the explicit formulation in subsection 3.3.3 that gives $p_4 = p_0$.
At the take-off condition, the inlet is iteratively sized to meet the heat rejection requirement. In each iteration, a new inlet area $A_1$ is found by multiplying the old inlet area $A_{1,o}$ by the ratio of required to actual heat rejection $\left(\dot{Q}_{TMS}/\dot{Q}_{HX}\right)$. This method is visualized in Figure 3.30 and leads to stable and quick convergence.

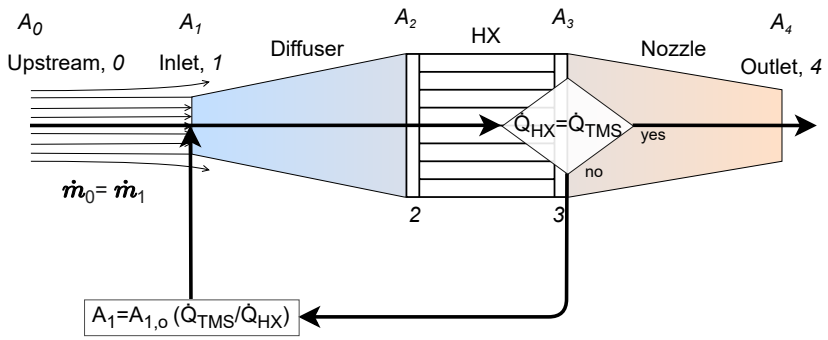


**Figure 3.30:** The iterative sizing method for the inlet area $A_1$ at the take-off condition.

The outlet is sized with a certain aspect ratio, by default 4, and a flap mechanism, the design of which is beyond the scope of this study. In the next subsection, the outlet maintains the same width, such that $h_{out}$ can be reduced by a simple flap mechanism. The inlet, diffuser and HX are invariable parts throughout the mission.

### 3.6.4. Evaluation Criterion: Cruise

After having designed the duct for take-off, it is assessed in cruise. The outputs of the sizing method are used to generate a standardized duct with **TOS**. The duct used for the evaluation criterion here is a copy of that duct with a different outlet height $h_{out}$. The method to appropriately obtain the new outlet area $A_4$ requires two nested iteration loops as is visualized in Figure 3.31. The outer loop sizes $A_4$ to match the needed heat rejection rate. The loop nested within adjusts the spillage rate that results from contracting the nozzle and works the same as in the standard **DRAX** design evaluation from Figure 3.12.
The reason why the cruise condition is used as the evaluation criterion is rather simple. Assuming that

the aircraft spends the majority of its flight time in cruise, this is the state where reducing cooling drag is the most impactful for power consumption and range. A more elaborate function that accounts for time spent in different mission phases could be used to generate a more representative sizing criterion. However, for the scope of this early-stage sizing tool and to demonstrate the methodology, only looking at cruise is sufficient.

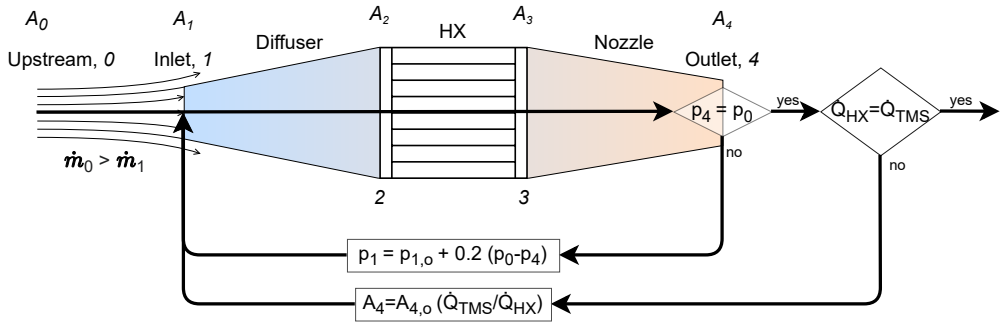


**Figure 3.31:** The iterative sizing method for the nozzle outlet area $A_4$ in cruise.

### 3.6.5. Optimization Algorithm

The employed optimization algorithm is a meta-heuristic differential evolution algorithm from the *scipy* optimization toolbox [53]. It works by generating a randomized set of points within the permitted design space that is defined by the design vector bounds. In this case, 15 points per generation. After evaluating all the points (design vectors) in a generation, the algorithm picks the best point and mutates it with other points in the generation. In the subsequent step, the new points are compared to their predecessors and depending on if they improve or degrade the solution, are selected for the next generation of points or discarded.

It has several advantages over conventional gradient based methods in this particular application. Firstly, it does not require an initial design vector from which it commences the iteration. Instead, the randomization of points allows for a wider exploration of the design space. This is very useful if the user of the optimization function does not have a good initial estimate of the HX dimensions and arrangement. If a pre-sized HX exists, the design vector bounds can be tightened to allow for faster convergence in a smaller design space around the original design.

Next to that, the HX model does not provide a continuous optimization space since the number of tubes or refrigerant flow layers can only be discrete. The differential evolution algorithm allows for integrality of parts of the design vector, such that only integer values are allowed for the number of refrigerant passages.

The extended design system matrix (XDSM) that describes the flow of information in the optimization algorithm is displayed in Figure 3.32. An amendment to the optimization strategy to better reflect the impact of the ducted ram-air HX by looking at the mass-added power consumption, beyond the scope of pure cooling drag, is discussed in chapter 7. In chapter 4, the optimization is performed with the total cooling drag, hence $D_{int} + D_{ext}$, as well as only the internal drag $D_{int}$ to portray how neglecting the external drag contribution leads worse overall drag performance as well as different design guidelines.

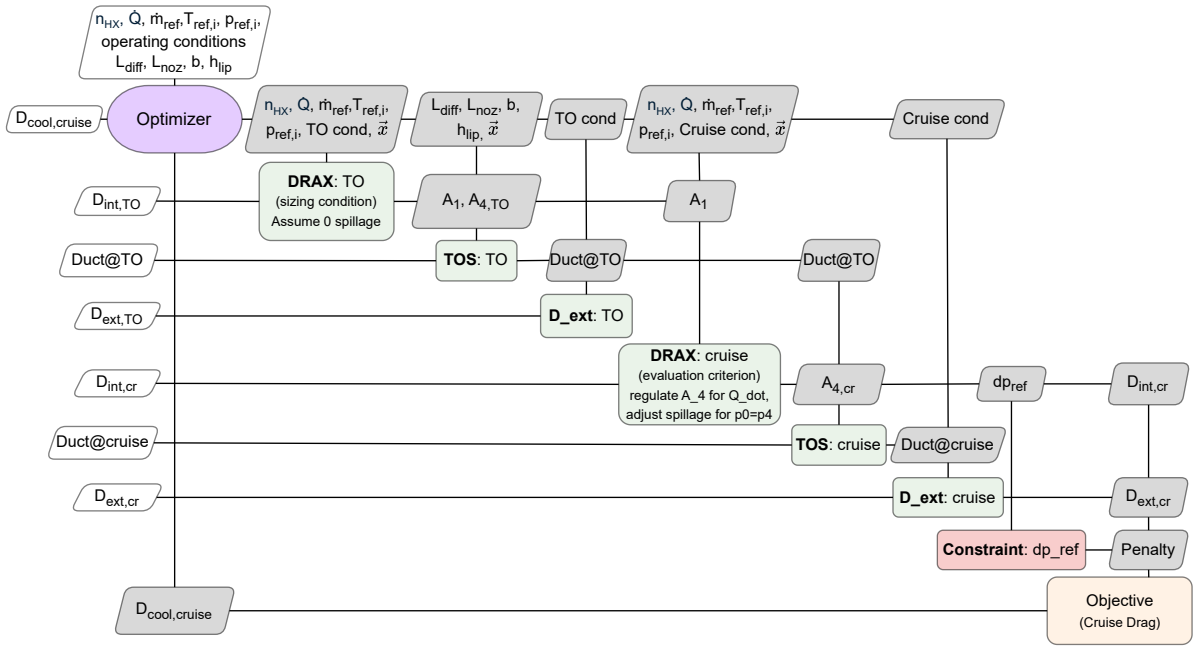


**Figure 3.32:** The extended design system matrix (XDSM) for optimizing the ducted ram-air heat exchanger.

# 4

# Results

This chapter presents the results that are obtained using the generated tools. By its end, it should be possible to answer all research questions expressed in chapter 2 to a level that the tool can reflect. First, section 4.1 presents the inputs used to generate the results corresponding to the base case. Using the optimization scheme from section 3.6, optimal FTHX and PFHX are designed under consideration of both the internal and external cooling drag in subsection 4.2.1. In subsection 4.2.2, the same optimization is performed considering only the internal contribution of cooling drag to showcase how an incomplete view on the cooling drag both skews the understanding of cooling drag and the HX design guidelines.
After comparing the output PFHX and the FTHX and the use of different optimization objectives, a sensitivity study on duct geometrical and performance parameters is performed by varying the fuselage burial constraint $b$ and the diverter height $h_{lip}$ as well as the isentropic nozzle efficiency. These findings are discussed in subsection 4.3.1 and subsection 4.3.2, respectively. Subsequently, subsection 4.3.3 and subsection 4.3.4 test the effect of TMS design constraints by varying the inlet temperature of the coolant $T_{ref,i}$ as well as the critical ambient temperature, used in the sizing criterion. Lastly, the effect of changing the cruise Mach number $M_{cr}$ on cooling drag is assessed in subsection 4.3.5.

## 4.1. Inputs for the 1MW Base Case

A comprehensive list of inputs for the steady TMS operation and the mission points used in the analysis of the 1 MW base case is compiled in Table 4.1. The heat load is split over two HX and the coolant inlet temperature is given to be 100 °C. Given the desired temperature gap of 15 °C throughout the FC, which is matched by the HX, the refrigerant mass flow rate comes out to 8.3 kg/s. The take-off and cruise conditions were picked for a conceptual 19-seater aircraft that falls under CS23. At take-off, an atmospheric temperature offset of 15 °C is implemented to size the ducted ram-air HX for a maximum ambient temperature of 30 °C.
In the fixed duct design parameters, the diffuser and nozzle length were chosen according to the reference design from Figure 3.18, to preserve a streamlined outer shape. The inlet aspect ratio as well as the outlet aspect ratio at take-off are set to 4, which yields sensibly looking designs. The burial depth is chosen very arbitrarily and is therefore also subject to the sensitivity study later on. It was chosen to set the burial constraint of the HX to 10cm into the fuselage for the reference case. The diverter height was chosen to be high enough to put the inlet outside of the boundary layer of the fuselage. Assuming that Prandtl's original flat plate formulations for the turbulent boundary layer are valid, one can estimate the boundary layer thickness of the fuselage. Taking the Unifier19 fuselage as an example, which has a total length of 18.44m, if the HX is placed somewhere half-way, it can be assumed that the downstream position of the duct inlet is $x = 8$ m. Then, at take off and cruise the thickness of the fuselage boundary layer is 9.6cm and 9.2cm, respectively.
The FTHX and PFHX details are assimilated with the test HX from Dong[41] and Hao[5], respectively.

**Table 4.1:** The TMS operational values for the base case with 1 MW power output.

| Symbol | Explanation | Value |
|---|---|---|
| **TMS inputs** | | |
| $P$ | Electrical output | 1 MW |
| $\eta_{FC}$ | FC efficiency | 0.52 |
| $n_{HX}$ | Number of HX | 2 |
| $\dot{Q}$ | Heat rejection per HX | 461.5 kW |
| $T_{ref,in}$ | Refrigerant inlet temperature | 100 °C |
| $p_{ref,in}$ | Refrigerant inlet pressure | 2 bar |
| $\dot{m}_{ref}$ | Refrigerant mass flow rate, per HX | 8.3 kg/s $\equiv$ 492.3 l/min |
| **Take-Off conditions** | | |
| $h_{TO}$ | Take-off altitude | 0 ft |
| $T_{off}$ | Atmospheric temperature offset | +15 °C |
| $V_{TO}$ | Take-off speed | 54.5 m/s |
| $M_{TO}$ | Take-off Mach | 0.16 |
| **Cruise conditions** | | |
| $h_{cr}$ | Cruise altitude | 18,000 ft |
| $V_{cr}$ | Cruise speed | 98.8 m/s |
| $M_{cr}$ | Cruise Mach | 0.31 |

**Table 4.2:** The set geometrical features of the base duct and the design details of the HX.

| Symbol | Explanation | Value |
|---|---|---|
| **Duct design** | | |
| $AS_{in}$ | Inlet aspect ratio | 4 |
| $AS_{out,TO}$ | Outlet aspect ratio at take-off | 4 |
| $L_{diff}$ | Diffuser length | 1.5 m |
| $L_{noz}$ | Nozzle length | 2 m |
| $b$ | Burial depth | 0.1 m |
| $h_{lip}$ | Diverter height | 0.1 m |
| **FTHX details** | | |
| $h_{tube}$ | Tube height | 3 mm |
| $t_{tube}$ | Tube material thickness | 0.2 mm |
| $R_{tube}$ | Tube edge radius | 0.2 mm |
| $L_a$ | Louver angle | 28 ° |
| $L_p$ | Louver pitch | 1.2 mm |
| $L_h$ | Louver height | $0.9 \cdot F_h$ |
| $F_p$ | Fin pitch | 3 mm |
| $F_h$ | Fin height | 8 mm |
| $t_f$ | Fin material thickness | 0.2 mm |
| **PFHX details** | | |
| $t_{plate}$ | Plate thickness | 0.5 mm |
| $p_{f,air}$ | Fin pitch, air side | 2 mm |
| $h_{fin,air}$ | Fin height, air side | 8 mm |
| $t_{fin,air}$ | Fin thickness, air side | 0.2 mm |
| $\ell_{s,air}$ | Fin strip length, air side | 3 mm |
| $p_{f,ref}$ | Fin pitch, refrigerant side | 2 mm |
| $h_{fin,ref}$ | Fin height, refrigerant side | 3 mm |
| $t_{fin,ref}$ | Fin thickness, refrigerant side | 0.2 mm |
| $\ell_{s,ref}$ | Fin strip length, ref side | 3 mm |

## 4.2. Results of Optimization

The optimization is performed once with the total cooling drag and once with only the internal cooling drag as the objective. The two following subsections show these results separately and for the two HX models.

### 4.2.1. FTHX vs. PFHX

The optimization algorithm was used to generate optimal ram-air FTHX and PFHX with the objective of reducing the total cooling drag $D_{cool}$ in cruise. The comparative results of this sizing procedure along with the drag values at take-off are visualized in Figure 4.1 and, for more precise reference, noted in Table 4.3.

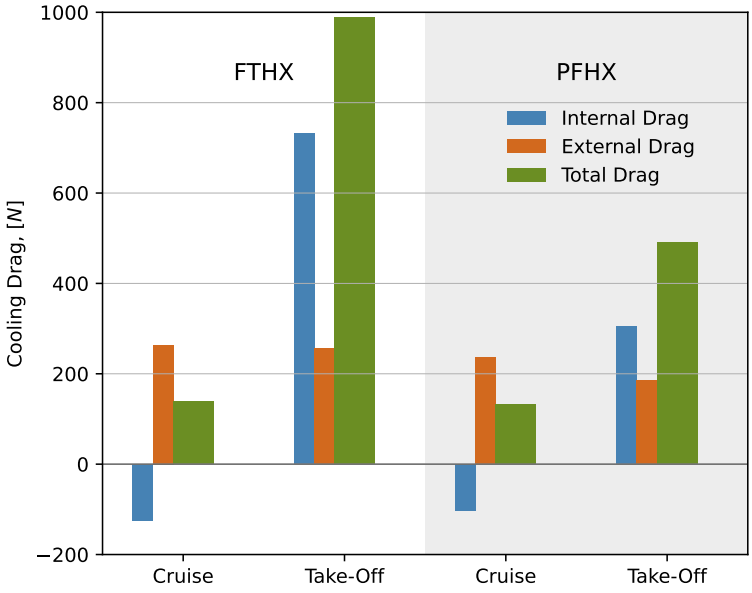


**Figure 4.1:** The cooling drag for the optimized FTHX and PFHX at cruise and take-off. Precise values are noted in Table 4.3.

**Table 4.3:** The total cooling drag and it's internal and external contributions for the optimized ducted ram-air FTHX and PFHX.

| | Cruise | Take-Off |
|---|---|---|
| [N] | **FTHX** | |
| $D_{int}$ | -125 | 732 |
| $D_{ext}$ | 264 | 256 |
| $D_{cool}$ | 139 | 988 |
| | **PFHX** | |
| $D_{int}$ | -104 | 305 |
| $D_{ext}$ | 236 | 185 |
| $D_{cool}$ | 132 | 490 |

The results show a slight preference for the PFHX over the FTHX in cruise. This is in line with recommendations in literature[2], which state PFHX to be the preferred HX for aerospace applications. While the FTHX is is able to offset slightly more drag in cruise than the PFHX, indicating that it attains a higher $j/f$ ratio, a measure of heat-transfer to air-side pressure drop incurred in a HX, the PFHX is more compact and thereby causes less external drag. Looking at the design results in Table 4.6, the FTHX has a larger frontal area than the PFHX. This enables the PFHX to be housed in a smaller duct cowling which reduces external drag. Figure 4.2 depicts the FTHX and PFHX duct cowling designs generated in OpenVSP with the outputs from **TOS** at the same scale. The hollow view portrays the placement of the HX within the cowling.

While the PFHX experiences rather moderate cooling drag at take-off, the FTHX cooling drag at take-off could be considered excessive, perhaps even impeding take-off performance, and thus, from a perspective of pure drag and the installation size, the PFHX is the likely winner in a trade off. This large difference in take-off cooling drag is explained by the much larger air intake that the FTHX design carries. Remember that the systems are designed to run full at take-off. Hence, as visualized in Figure 4.2 and noted in Table 4.6, the FTHX installation requires twice the air mass flow at take-off. The cooling drag at take-off is higher than in cruise for both HX, as the air intake at take-off is higher to compensate for the smaller temperature gap between the air and the coolant at ground conditions. Moreover, waste heat recovery is less efficient at lower Mach numbers, as postulated by Meredith[14] and also further substantiated in subsection 4.3.5. The reason why the external cooling drag varies so little between the take-off and the cruise condition is because, despite the larger dynamic pressure in cruise, the lip suction effect caused by spilling at the inlet offsets a large portion of external drag. The FTHX duct, with its very large air inlet, runs at a spillage rate of 70% in cruise, while the PFHX does at

55% which helps further explain why the FTHX external drag in cruise is not much larger, despite the larger frontal area.
To add caution to this interpretation, it is very possible that the lip suction effect on the FTHX is overestimated, as the upper surface of the cowling depicted in Figure 4.2a is much more flat than the one of the PFHX and the base duct used to construct the surrogate model. The ESDU 86002 [30] design handbook postulates that the lip suction effect is more pronounced for hooded inlets, where the forebody curves down. Hence, a shape more akin to Figure 4.2b.
One should keep in mind that the results displayed here, alone, don't fully reflect the arguments that would go into choosing a HX, most importantly, the HX mass. It is possible that if the FTHX is lighter than the PFHX, it can offset the larger cooling drag in cruise. Furthermore, the FTHX model yields smaller refrigerant side pressure drops, resulting in decreased pumping power. In addition, the results can not be considered definitive, as the channel dimensions of both HX are fixed. Using larger inputs for the refrigerant side fin height on the PFHX has shown that if chosen improperly, the PFHX can easily underperform and yield much worse results than the FTHX. Because of these uncertainties, in order to make a more precise judgment it would be advised to firstly, include the HX mass model and refrigerant side pressure drop models into the optimization objective and secondly, extend the design vector to also include more detailed HX design parameters.
For this study, only looking at cooling drag, the observation can however be made that in line with expectations, the PFHX performs better than the FTHX. Note also that in the inputs for this comparison, the FTHX and PFHX air side and coolant side channel dimensions were purposely kept similar, in order to make the comparison more fair.

**Table 4.4:** The design features of the optimized ducted ram-air FTHX and PFHX.

| | **FTHX** | **PFHX** |
|---|---|---|
| **Final Design Vector** | | |
| $n_{pass}$ | 128 | 108 |
| $B_H$, [m] | 1.416 | 1.305 |
| $B_W$, [m] | 1.362 | 0.8799 |
| $B_D$, [m] | 0.0838 | 0.0553 |
| $\theta$, [°] | 70 | 69.97 |
| **Duct Stations** | | |
| $A_1$, [m$^2$] | 0.414 | 0.186 |
| $A_2$, [m$^2$] | 0.660 | 0.393 |
| $A_{HX,fr}$, [m$^2$] | 1.928 | 1.148 |
| $A_{4,TO}$, [m$^2$] | 0.579 | 0.270 |
| $A_{4,cruise}$, [m$^2$] | 0.141 | 0.101 |

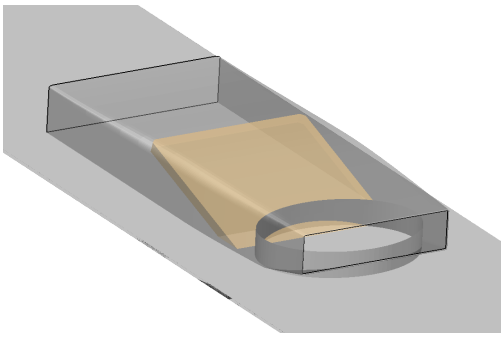

**(a)** FTHX duct at take-off

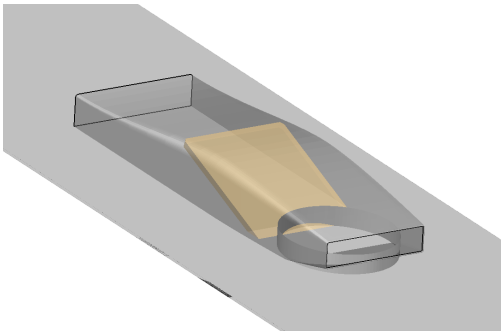

**(b)** PFHX duct at take-off

**Figure 4.2:** The wall-bound ram-air duct cowlings corresponding to the HX from Table 4.6 depicted at the same scale.

The PFHX is notionally fitted to the fuselage of a 19-seater aircraft, Unifier19 in this case. Figure 4.3 depicts this and shows how even this comparatively compact installation alters the appearance of the fuselage significantly. In real life, the installation faces two major problems. To begin with, if the duct is placed as it is in Figure 4.3, some rows of passengers would not be able to look outside through windows and the placement of an emergency exit, if certification requires it, is also more difficult. One solution could be to move the duct backwards, which in turn leads to the second problem, that is the aerodynamic surface of the duct. Assuming that the current shape of the duct is more or less preserved, it would exert a non-negligible moment around the center of balance of the aircraft when the angle of

attack is changed. It is expected that with shifting back the duct, this moment counters any change in angle of attack, similarly to a horizontal stabilizer. However, the lack of control provided by the duct would likely complicate making the aircraft aerodynamically stable such that it is unlikely to be preferred by aircraft designers. Moreover, the added weight of the installation might prohibit moving the installation too far back, lest it makes the aircraft longitudinally unstable.

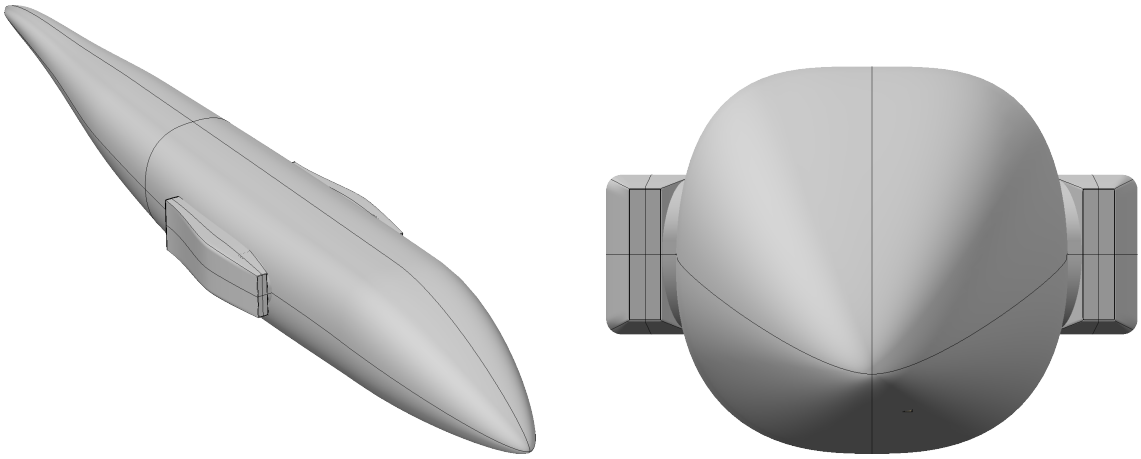

**(a)** Iso view **(b)** Front view

**Figure 4.3:** The PFHX installation from Table 4.3 fitted to the Unifier19 fuselage.

### 4.2.2. Balancing Internal and External Drag Sources

Many papers found in literature consider only the internal drag contribution of a ducted ram-air HX. Clearly, Figure 4.1 already proves that neglecting external drag sources of the cooling drag is a stark underestimation of the total cooling drag. However, besides influencing the cooling drag values, the observance of external drag sources also changes design guidelines of the HX core as this subsection will prove. By reducing the objective function in the optimization to merely the cruise internal drag, the results shown in Figure 4.4 are produced.

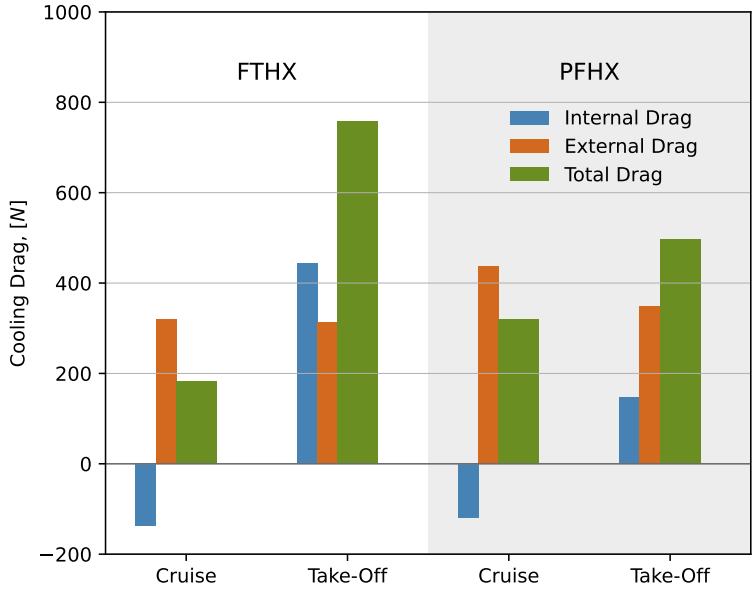


**Figure 4.4:** The cooling drag for the FTHX and PFHX with minimal internal drag at cruise and take-off. Precise values are noted in Table 4.5.

**Table 4.5:** The total cooling drag and it's internal and external contributions for the ducted ram-air FTHX and PFHX with minimized internal drag.

| | Cruise | Take-Off |
|---|---|---|
| [N] | **FTHX** | |
| $D_{int}$ | -136 | 443 |
| $D_{ext}$ | 319 | 314 |
| $D_{cool}$ | 182 | 758 |
| | **PFHX** | |
| $D_{int}$ | -119 | 148 |
| $D_{ext}$ | 438 | 349 |
| $D_{cool}$ | 319 | 497 |

As is expected, the waste heat recovery is exploited further with the FTHX again attaining a higher $j/f$ ratio than the PFHX. The total cooling drag in cruise for both the FTHX and the PFHX is, nevertheless, aggravated due to the larger external drag. Interestingly, the FTHX total cooling drag at take-off is reduced when compared to the results presented in Figure 4.1, due to a large reduction in internal drag. When only considering the internal drag, the optimizer seeks to maximize the frontal area of the HX. For the PFHX, both the number of passage layers $n_{pass}$ and the core width $B_W$ approach their upper bounds but are limited by the core depth $B_D$. When it comes to the FTHX, a similar trend is observed. $B_W$ and $n_{pass}$ meet their upper bound but $B_W$ doesn't fully reach it, either because it leads to too large diffuser expansion ratios incurring losses or because the design vectors in the optimization didn't properly explore the space at the $B_W$ upper bound. Result polishing, where a gradient based optimization is applied after the differential evolution algorithm converges, was turned off as it was shown to add a lot of time to the optimization process while giving little additional insight.

In order to reduce the air side pressure drop, and thus the internal drag, the optimizer tries, for both HX, to shorten the friction length, which for the air is the core depth $B_D$, and simultaneously needs to extend the frontal area to still match the required heat rejection rate. One way to word it is that when only the internal drag is observed, the optimizer strives to turn the HX into a pancake. Contrary to that, when the external drag is also accounted for, as in Figure 4.1, a non-trivial solution in the design space is found that balances the internal and external drag, reducing their sum.
The fact that the balance between internal and external drag changes between cruise and take-off was expected. Meredith already writes in his initial report on aircraft engine cooling from 1935 [14] that the waste heat recovery effect is more pronounced with increasing $M$, which is further touched upon at the end of this chapter. Simultaneously, the external drag for a certain duct is assumed to scale with the dynamic pressure $q_\infty$ and the spillage rate $SR$ in this model, which work against each other. Note in addition, that the external drag is also affected by the closing of the flap at the outlet.

The duct cowlings are again depicted in Figure 4.5. This time, the protrusion is significantly higher for both HX and the PFHX duct cowling is barely streamline anymore. Notably, the duct diffuser of the PFHX was also lengthened above the base value of 1.5 m in order to respect the maximum ramp angle $\alpha$, in line with the method defined in the design rules in subsection 3.4.1.

**Table 4.6:** The design features of the optimized ducted ram-air FTHX and PFHX.

| | **FTHX** | **PFHX** |
|---|---|---|
| **Final Design Vector** | | |
| $n_{pass}$ | 140 | 137 |
| $B_H$, [m] | 1.548 | 1.653 |
| $B_W$, [m] | 1.480 | 1.403 |
| $B_D$, [m] | 0.0766 | 0.0522 |
| $\theta$, [°] | 69.74 | 69.86 |
| **Duct Stations** | | |
| $A_1$, [m$^2$] | 0.396 | 0.149 |
| $A_2$, [m$^2$] | 0.794 | 0.799 |
| $A_{HX,fr}$, [m$^2$] | 2.291 | 2.320 |
| $A_{4,TO}$, [m$^2$] | 0.497 | 0.200 |
| $A_{4,cruise}$, [m$^2$] | 0.140 | 0.0862 |

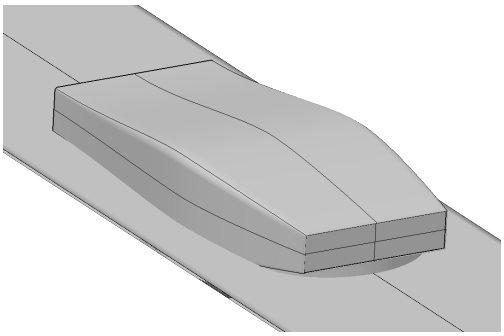

**(a)** FTHX duct at take-off

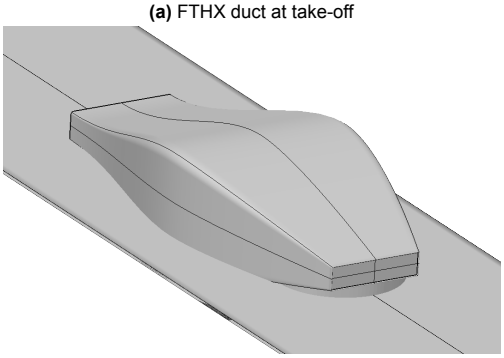

**(b)** PFHX duct at take-off

**Figure 4.5:** The wall-bound ram-air duct cowlings corresponding to the HX from Table 4.6 depicted at the same scale as Figure 4.2.

## 4.3. Sensitivity Study

The base case that is evaluated in subsection 4.2.1 yields valuable results that contribute to the understanding of cooling drag. However, some parameters that were chosen to construct this base case, more precisely the duct, are picked more or less arbitrarily for lack of a proper resource that might provide a value.
Section 4.3.1 seeks to analyze the impact of the burial constraint and the diverter height on the external cooling drag in order to assess their importance in the design of a ram-air duct and the HX-placement around the fuselage. In addition, for lack of a proper model, the nozzle efficiency was assumed ideal in the base case. In order to see how different assumptions may affect the cooling drag and optimum HX design, losses are introduced in subsection 4.3.2
The effects of changing the TMS operational temperature and the critical ambient temperature for sizing are quantified in subsection 4.3.3 and subsection 4.3.4, respectively. Finally, subsection 4.3.5 looks at how the internal and external cooling drag contributions scale with cruise velocity.

The sensitivity study is in parts performed on a fixed HX design, namely the optimal PFHX from subsection 4.2.1. The FTHX and PFHX are expected to behave similarly to changing external parameters, not pertaining to the design of either HX. Therefore, the sensitivity study can be considered valid for both types of HX. For sections, where the optimization algorithm is rerun under new conditions, the PFHX model is used.

### 4.3.1. Varying the Burial Constraint and the Diverter Height

The burial constraint $b$ nearly directly controls the protrusion height of the duct cowling. Thereby, a larger value for $b$ allows to bury the HX deeper inside the fuselage which reduces the protrusion height $h_{max}$, also reducing the frontal area $A_{max}$. This in turn varies the external drag by altering the $f_1$ factor that goes into determining the duct-specific drag coefficient as well as altering the reference area for the pressure drag. The sensitivity study for $b$ and $h_{lip}$ is performed for a fixed HX design vector. This way, the stochastic influence of the differential evolution optimizer on single results is eliminated and the data is generated at a lower computational cost.

The effects of varying $b$ and $h_{lip}$ on the external contribution to cooling drag $D_{ext}$ in cruise are shown in relation to each other in Figure 4.6. The general trend with increasing $b$, regardless of $h_{lip}$, unsurprisingly shows that a more relaxed burial constraint reduces external drag very effectively. The graphs with non-zero $h_{lip}$ in Figure 4.6 show that this trend is limited, however. When the burial constraint is relaxed two scenarios can occur. In the first one, the lower ramp angle $\alpha$ limits the burial depth of the HX, such that the burial constraint is never met.
The other one is that the duct cowling eventually reaches a point where the maximum protrusion height is defined by the duct inlet (station 2 in the stack geometry) and not the HX (station 3 in the stack geometry). Relaxing the burial constraint further no longer changes the duct cowling shape beyond that point, as the design rules in **TOS** prohibit slumped duct cowlings, where the height of the HX station (3) is lower than the inlet or outlet. Therefore, $D_{ext}$ levels off at some point. The internal drag model remains unaffected when varying $b$ and $h_{lip}$ as the implemented model is insensitive to the changes. $D_{int}$ is equivalent to the cruise value listed in Table 4.3 for the PFHX.

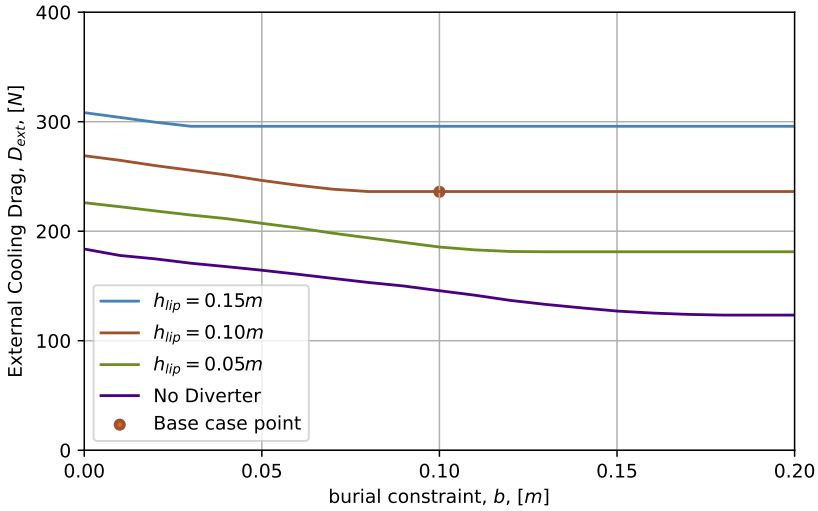


**Figure 4.6:** The external contribution to the cooling drag $D_{ext}$ for the base case TMS operation with varying burial constraint $b$ and diverter height $h_{lip}$. $D_{ext}$ summed for a TMS with 2 HX.

The obvious take-away from Figure 4.6 is that being able to bury the HX deeper in the fuselage leads to lower external drag. Moreover, as was already seen when constructing the surrogate model for the external drag in subsection 3.5.5, the external drag can be greatly reduced when decreasing the frontal area of the diverter or even removing it altogether, since the simplified diverter geometry incurs a large spot of stagnant air at the front. This, however, is a design choice that needs to be weighed against the effect that not having a lip rise has on air mass flow intake, and thus is not as trivial as the graph suggests.
While these findings certainly bear some truth, they should be regarded with a dose of skepticism. For one, the results in Figure 4.6 are produced with the surrogate drag model, the accuracy of which shall be explored in chapter 5. Next to that, and most importantly for the diverter-less case, the external drag model does not account for the effect of the fuselage boundary layer, which would certainly affect both the mass flow into the duct, necessitating a larger inlet as well as affect the external drag of the ducted ram-air HX installation. In future works, more focus should be put on representing these interaction effects.

### 4.3.2. Varying the Assumed Nozzle Isentropic Efficiency

The nozzle isentropic efficiency $\eta_{noz}$ was assumed ideal so far. While nozzle losses are very small and the assumption of them being negligible compared to other losses is acceptable for a conceptual tool, assessing the impact of $\eta_{noz}$ on the internal drag can be interesting to see how many resources should be allocated to better assessing $\eta_{noz}$ in the future.
Similar to the approach in the above section, the varying $\eta_{noz}$ shall be implemented on a fixed FTHX design, again the optimum design vector listed in Table 4.3. In addition to that, the optimization is re-evaluated for different $\eta_{noz}$ to see how design guidelines under increasing duct losses may change. All values other than $\eta_{noz}$ are the same as in Table 4.1 and Table 4.2.

The explored range of nozzle losses is very limited. In ”Mechanics & Thermodynamics of Propulsion” by Hill and Peterson [20], the authors state $\eta_{noz}$ values ranging from 0.95 to 0.98 for turbomachinery nozzles. However, the extent to which turbomachinery losses are applicable to the ducted ram-air HX is questionable, not only because their designs vary but also because the compressors in these devices build up a large amounts of pressure, allowing for greater losses. Generally, losses above 1% would be too pessimistic in this tool, given that in the implementation of Pittaluga’s diffuser model in **DRAX** in subsection 3.3.1, an ideal isentropic efficiency was assumed for a straight diffuser where no expansion occurs ($AR = 1$). Excessive values for $\eta_{noz}$ would therefore be inconsistent with other parts of the model. The discussion of the results below also shows that larger losses cannot be supported by the system without some puller fan that curbs the nozzle losses.

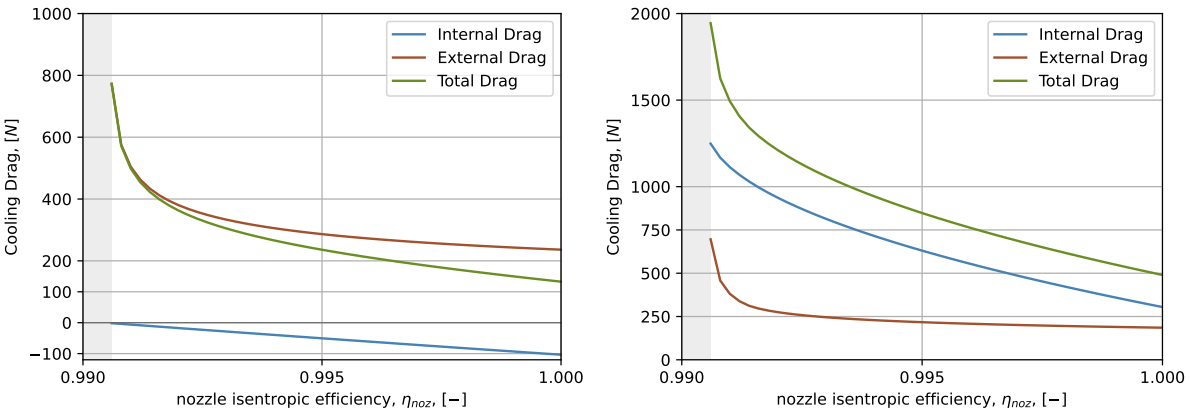


**(a)** Cruise **(b)** Take-off

**Figure 4.7:** Cooling drag of the fixed FTHX from Table 4.3 for varying nozzle efficiency.

Figure 4.7 shows how the cooling drag is affected by changes in the assumed nozzle isentropic efficiency $\eta_{noz}$ for cruise and at take-off. The variance in cooling drag is stark, even within the limited range of 1% losses considered here.
Initially, focusing on the internal drag, one can see that in cruise, with nozzle losses approaching 1%, the PFHX installation no longer offsets cooling drag. This finding is important as it shows that, unless a system is very well designed, the Meredith effect can not be exploited. At take-off, the increase in internal cooling drag is very pronounced, such that a loss of just less than 1% at take-off increases the total cooling drag four-fold. In fact, the internal drag follows an asymptotic behavior with increasing nozzle loss. At some point, it can no longer be evaluated at take-off as the total pressure losses of the installation surmount the dynamic pressure upstream, $q_\infty$. In that case, following the procedure of Figure 3.30 and assuming $p_4 = p_0$ at the outlet leads to $p_4 > p_{t,4}$, which besides not making sense, cannot be solved by the isentropic flow equations. In Figure 4.7, this asymptotic behavior is clearly visible and the unresolved region where the loss-threshold $p_{t,3} \cdot \eta_{noz} < p_0$ is crossed is marked in gray. In that case, if a nozzle is known to have larger losses, a puller fan must be installed within the nozzle in order to restore some pressure.
As this model is shape-sensitive to the duct design, the different nozzle and diffuser designs that are fitted around the HX affect the external drag too. While this effect is not very pronounced at take-off, the difference in proportionality of internal and external drag in cruise means that in this condition, the change in external drag is nearly as relevant as the internal drag rise. Moreover, when the losses start deteriorating (left part of the curve), the nozzle goes from contracting to expanding as it must trade the little remaining dynamic pressure in the system to raise the static pressure from station 3 (HX-outlet) to 4 (nozzle outlet). In the model, this leads to an increase in the outlet area which is so large that it surpasses the frontal area of the part of the cowling closest to the HX. The direct result is an increase in the projected area of the duct, which is why the external drag rises this rapidly at some point. This highlights the multidimensionality of thermal management problems and the many nuances that play into designing and integrating a ducted ram-air HX.

Figure 4.8 shows the cooling drag in cruise and at take-off for reoptimized PFHX. Reoptimizing the HX under the assumption of different $\eta_{noz}$ leads to similar results as above, albeit the rise in cooling drag with increasing nozzle losses is slightly curbed. In addition, it is then also possible to design a system which can sustain the 1% nozzle losses. The output design vectors for the different FTHX optimizations are given in Table 4.7 along with the duct cross sections. The design trend with increasing the nozzle losses is to increase the frontal area $A_{HX,fr}$ of the heat exchanger. This way, the area ratio $AR$ in the diffuser is increased which raises the static pressure head needed to surmount the HX and nozzle pressure losses. This suggests that depending on the assumption of ducting losses, different designs are favorable.

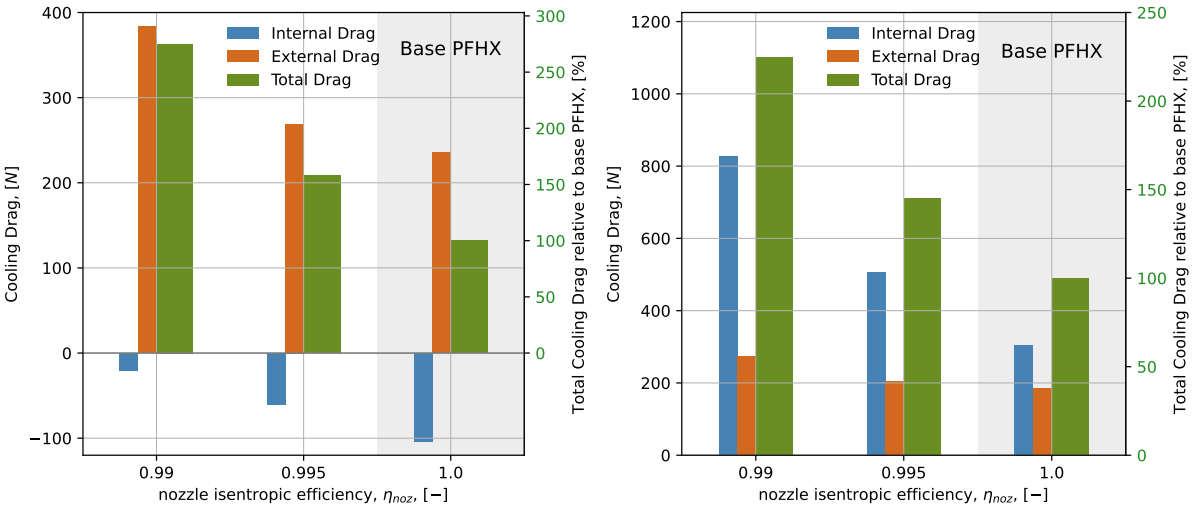


**(a)** Cruise **(b)** Take-off

**Figure 4.8:** Cooling drag of the reoptimized PFHX for varying nozzle efficiency.

**Table 4.7:** The design features of the reoptimized ducted ram-air PFHX for varying nozzle losses.

| $\eta_{noz}$, [-] | 0.99 | 0.995 | 1.00 |
|---|---|---|---|
| **Final Design Vector** | | | |
| $n_{pass}$ | 110 | 109 | 108 |
| $B_H$, [m] | 1.341 | 1.317 | 1.305 |
| $B_W$, [m] | 1.253 | 0.9770 | 0.8779 |
| $B_D$, [m] | 0.0554 | 0.0611 | 0.0553 |
| $\theta$, [°] | 69.98 | 69.92 | 69.97 |
| **Duct Stations** | | | |
| $A_1$, [m$^2$] | 0.1598 | 0.164 | 0.186 |
| $A_2$, [m$^2$] | 0.575 | 0.442 | 0.393 |
| $A_{HX,fr}$, [m$^2$] | 1.680 | 1.287 | 1.148 |
| $A_{4,TO}$, [m$^2$] | 0.634 | 0.326 | 0.270 |
| $A_{4,cruise}$, [m$^2$] | 0.0978 | 0.0962 | 0.101 |

### 4.3.3. Varying the TMS Operating Temperature

The refrigerant inlet temperature of the TMS that is chosen for the base design (Table 4.1) is reasonably high. For fuel cells, this is acceptable. However, it is not unlikely that the TMS must operate at lower temperatures. For instance, the Unifier19 FC-TMS runs at a FC inlet temperature of 45 °C, which works out to $T_{ref,i} = 80$ °C in the heat exchanger under the operating conditions postulated in the documentation [1].

It can be said that a higher coolant temperature should be beneficial towards reducing cooling drag and TMS power. For one, a higher $T_{ref,i}$ increases the temperature gap in the HX, which under consideration of Equation 3.1, restated below, promotes the heat transfer rate $\dot{Q}$ in the HX. As a consequence, either the heat transfer area, proportional to the HX size can be reduced, lowering drag, or the refrigerant mass flow rate can be decreased, which reduces the pumping power.

Since the goal here is to see how different TMS temperature requirements affect the cooling drag, the refrigerant mass flow rate $\dot{m}_{ref}$ is maintained constant, such that the outlet temperature of the HX decreases at the same rate as $T_{ref,i}$. The expected result is an increase in the HX frontal area and an increase in cooling drag with decreasing $T_{ref,i}$.

$$\dot{Q} = \epsilon \cdot C_{min} \left(T_{ref,i} - T_{air,i}\right)$$

It would be nice to see how the HX size and cooling drag can be minimized if the FC is allowed to run at higher temperatures. This could be done by increasing $T_{ref,i}$ to, for instance 110 °C. However, the data for Ethylene Glycol obtained through *CoolProp* is limited to temperatures up to 100 °C [54] and as such, **DRAX** in its current state cannot explore higher $T_{ref,i}$ for Ethylene Glycol, unless amended. Nevertheless, the trends that can be observed when decreasing $T_{ref,i}$ should suffice to deduce trends of increasing $T_{ref,i}$ beyond 100°C.
The optimization algorithm is rerun for a PFHX with a $T_{ref,i}$ of 90 °C and 80 °C. This results in refrigerant outlet temperatures of 75 °C and 65 °C, respectively. Figure 4.9 shows the variation of the cooling drag in cruise and at take-off for these changed $T_{ref,i}$ along with the design outputs in Table 4.8 and depicted in Figure 4.10. The observations are not entirely in line with expectations. While reducing the refrigerant inlet temperature causes cooling drag to rise significantly at take-off, largely due to the need to pass more air through the system, the cruise drag remains practically steady and goes down by 1 N per -10 °C increment. The PFHX installation that is sized at the take-off condition requires a larger frontal area $A_{HX,fr}$ as $T_{ref,i}$ is reduced since the heat transfer area must be enlarged to compensate for the smaller temperature gap with the ambient air. These designs are more akin to the ones generated when only the internal drag at cruise was used as the design objective in subsection 4.2.2. Since the air side pressure drop is proportional to the air mass velocity $G$ in the passages (see Equation 3.34), the larger diffusion area resulting in smaller internal flow velocity incurs smaller air side pressure drops, leading to increased internal cooling drag offset. On top of that, the increased spillage of the ducts for the inlet temperature of 90 °C and 80 °C means that a larger portion of the external drag is offset, which curbs the rise in external drag to a great extent at cruise.

That is not to say that the lower TMS operating temperatures are favorable for aircraft performance. On the contrary, the significant increase in cooling drag at take-off as well as the larger installation size still make higher TMS operating temperatures the more attractive choice. As such, increasing the TMS operating temperature by even just a few degrees, say to 105 °C could bring about a very advantageous reduction in take-off cooling drag and installation size.
Figure 4.11 further puts the difference in size of the base PFHX installation and the one with the lowest refrigerant inlet temperature in perspective. The effects of the installation discussed in subsection 4.2.1 on passenger comfort, compliance with safety regulations and the impact of the aerodynamic surface and the weight of the installation on stability and controllability would be further aggravated with the larger installation.

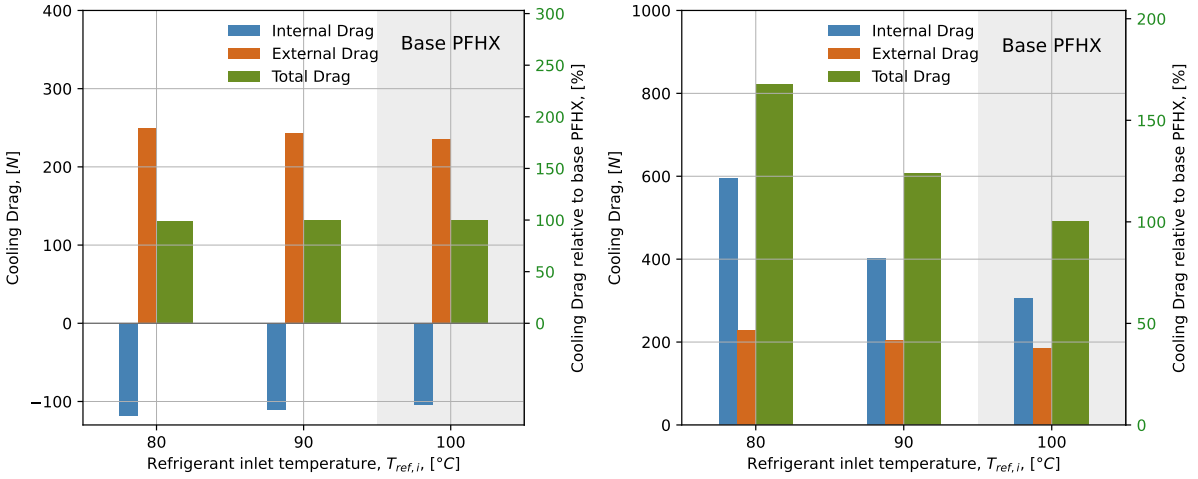


**(a)** Cruise

**(b)** Take-off

**Figure 4.9:** Cooling drag of the reoptimized PFHX for varying refrigerant inlet temperature.

**Table 4.8:** The design features of the reoptimized ducted ram-air PFHX for varying refrigerant inlet temperature.

| $T_{ref,i}$, [°C] | 80 | 90 | 100 |
|---|---|---|---|
| **Final Design Vector** | | | |
| $n_{pass}$ | 113 | 111 | 108 |
| $B_H$, [m] | 1.365 | 1.341 | 1.305 |
| $B_W$, [m] | 1.163 | 0.990 | 0.8779 |
| $B_D$, [m] | 0.0555 | 0.0553 | 0.0553 |
| $\theta$, [°] | 69.98 | 69.97 | 69.97 |
| **Duct Stations** | | | |
| $A_1$, [m$^2$] | 0.291 | 0.227 | 0.186 |
| $A_2$, [m$^2$] | 0.544 | 0.455 | 0.393 |
| $A_{HX,fr}$, [m$^2$] | 1.588 | 1.328 | 1.148 |
| $A_{4,TO}$, [m$^2$] | 0.438 | 0.332 | 0.270 |
| $A_{4,cruise}$, [m$^2$] | 0.115 | 0.108 | 0.101 |
| **Spillage Rates** | | | |
| $SR$, [%] | 64 | 60 | 55 |

**Figure 4.10:** The frontal views of the ducts sized for 80 °C, 90 °C and 100 °C coolant inlet temperatures, from left to right. Same scales apply.

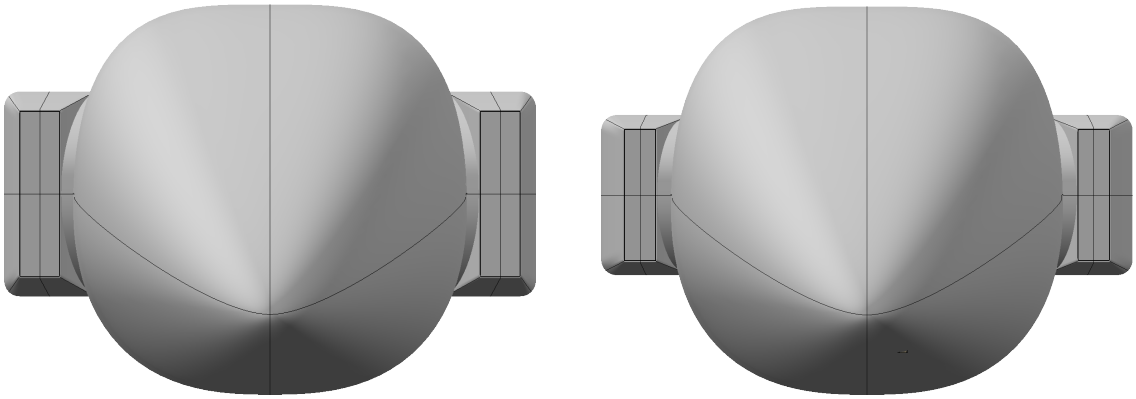

**(a)** The PFHX installation sized for $T_{ref,i} = 80$ °C

**(b)** The PFHX installation sized for $T_{ref,i} = 100$ °C (base)

**Figure 4.11:** The placement of the PFHX installations on the Unifier19 fuselage.

### 4.3.4. Varying the Critical Ambient Temperature

In the reference case noted in Table 4.1, the ambient temperature on the ground is offset by $T_{off} =$ +15 °C. This means that the system is sized such that it can maintain thermal balance at an ambient temperature at take-off of $T_0 = 30$°C. One drawback of the TMS imagined in the optimization method is that it assumes a static source temperature, as it demands that the heat balance is matched at all times.

While power electronics are temperature sensitive, small temporary deviations in temperature could be permitted at critical mission points, i.e. take-off. Moreover, considering that FCs do tend to have a large thermal mass, meaning that the increase in temperature per input of heat unit is small, a slight heat imbalance at take-off could be accepted given that the FC temperature rises slowly. The idea of allowing the power electronics to absorb some waste heat in their thermal mass in critical points is also suggested by Kellerman [27].

One way to reduce the criticality of the HX sizing point is to lower the temperature offset. A conservative

new value for $T_{off}$ could be 10 °C. The expected result of running the optimization under this relaxed temperature offset is a smaller HX with a smaller intake, as less air for cooling is required, that reduces cooling drag in cruise notably. The optimization is also run for a much more critical case where the ambient temperature offset at take-off is 30 °C, amounting to an outside temperature of 45 °C, which in the U.S. military handbook MIL-HNDBK-310 [55] is classified as a particularly hot day occurring at 5% frequency.

Figure 4.12 shows the cooling drag under consideration of the relaxed and tightened ambient temperature offset at take-off. The newly generated designs are compared to the baseline PFHX in Table 4.9 and depicted in Figure 4.13. At take-off, the cooling drag rise is explained by the increased air mass flow needed to make up for the reduced temperature gap between the coolant and the ambient air. Hence, a larger temperature offset causes more drag, although the small reduction in take-off cooling drag between the 15 °C and the 10 °C temperature offset would not be enough to justify making the TMS less robust.
Similarly to the previous analysis in subsection 4.3.3, the cooling drag development in cruise is rather counter intuitive but a look at Table 4.9 gives insight into what is happening. For larger critical offset temperatures, the installation size increases and again produces designs capable of improved waste heat recovery. Hence, the higher internal cooling ”thrust” at 30 °C. Simultaneously, as the temperature offset is not carried over into cruise, this design is oversized for that condition and therefore a larger spillage rate is found which increases the drag offset modeled in the external drag model. Again, that is not to say that the overall performance of the system makes this installation favorable. Only a more detailed analysis including the mass of the heat exchanger and the surrounding cowling can tell how the systems compare to each other in terms of added power consumption by combining the cooling drag and the installation mass in a single value.
In absolute terms, the reduction in cooling drag for the oversized 30 °C case is likely not large enough to make up for the debts incurred by the size and mass of that system over the other analyzed cases. Including another figure of a fuselage fitted duct would be redundant at this point but the discussions and comparisons from the previous subsection and Figure 4.11 are just as applicable here. Nevertheless, this analysis would suggest that oversizing a ducted ram-air HX installation has no impeding effect on the cooling drag of the system and that oversizing the air inlet and, assuming that it is designed to properly exploit lip suction, could in fact lower cooling drag throughout a typical mission.

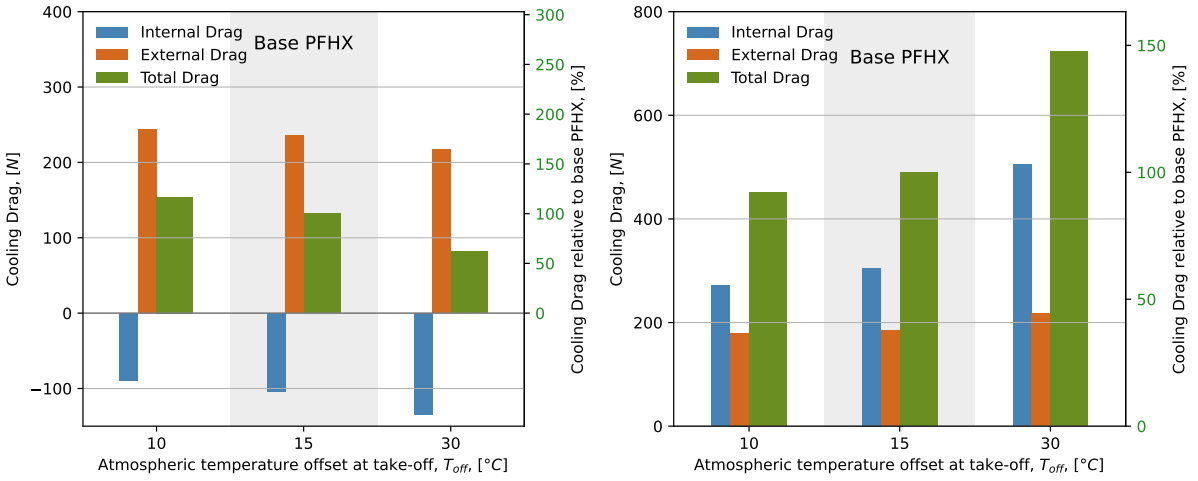


**(a)** Cruise **(b)** Take-off

**Figure 4.12:** Cooling drag of the reoptimized PFHX for varying atmospheric temperature offset at take-off.

**Table 4.9:** The design features of the reoptimized ducted ram-air PFHX for varying atmospheric temperature offset at take-off.

| $T_{off}$, [°C] | 10 | 15 | 30 |
|---|---|---|---|
| **Final Design Vector** | | | |
| $n_{pass}$ | 107 | 108 | 112 |
| $B_H$, [m] | 1.293 | 1.305 | 1.353 |
| $B_W$, [m] | 0.849 | 0.8779 | 1.094 |
| $B_D$, [m] | 0.0554 | 0.0553 | 0.052 |
| $\theta$, [°] | 69.98 | 69.97 | 69.95 |
| **Duct Stations** | | | |
| $A_1$, [m$^2$] | 0.178 | 0.186 | 0.267 |
| $A_2$, [m$^2$] | 0.376 | 0.393 | 0.508 |
| $A_{HX,fr}$, [m$^2$] | 1.098 | 1.148 | 1.481 |
| $A_{4,TO}$, [m$^2$] | 0.255 | 0.270 | 0.393 |
| $A_{4,cruise}$, [m$^2$] | 0.107 | 0.101 | 0.095 |
| **Spillage Rates** | | | |
| $SR$, [%] | 50 | 55 | 70 |

**Figure 4.13:** The frontal views of the ducts sized for 10 °C, 15 °C and 30 °C temperature offsets at take-off, from left to right. Same scales apply.

### 4.3.5. Varying the Cruise Speed

Research Question 2 asked how the cooling drag scales with ambient temperature and flight conditions. The above sections already answer the first part of that question and to some degree the comparison of cruise to take-off cooling drag preludes the second answer. Namely, the balance between internal and external cooling drag sources flips from take-off to cruise. Figure 4.14 reflects how the cooling drag, both internal and external, changes in cruise with a changing Mach number $M_{cr}$ and equivalent airspeed $V_{EAS}$.

As is expected, the two cooling drag sources follow opposite trends. With rising $M$, the internal drag turns into a thrust force while the external drag rises at an increasing rate. The rise in external drag is the result of three factors; the increase in dynamic pressure which is proportional to ${V_{EAS}}^2$, the closing of the flap which works to slightly increase the estimated $C_D$ of the installation, and the lip suction effect which in turn offsets the $C_D$ to some extent and which rises with spillage and thus, the air velocity. The result is that, beyond a little kink at very low $M_{cr}$ where the nozzle opening supposedly changes the projected area of the duct, the external drag rise is nearly linear, although with a slightly increasing rate of ascent.

At low airspeeds, the decrease in internal drag is faster than the increase in external drag until the rate of change appears to level off. With the opposing trends and varying rates of change, this leads to an interesting observation that up to around $M_{cr} = 0.225$, the total cooling drag decreases to a minimum. Above that, the external cooling drag rises faster than the internal drag offset, meaning that around the considered reference case's $M_{cr}$ of 0.31, the simple observation is made that increasing the flight speed increases the total cooling drag, albeit at a slow rate. If one only considered the internal cooling drag, one might be mislead to conclude that higher $M_{cr}$ are beneficial since more drag is offset internally. However, the analysis provided here shows that the internal thrust increase cannot outdo the external drag increase of the duct cowling at a realistic cruise velocity, let alone that of the rest of the aircraft.

The Mach numbers above 0.3 in Figure 4.14 are shaded to reiterate that due to the negligence of compressibility effects in the external drag model, the confidence in the external drag at $M_{cr} > 0.3$ is limited. For the reference case, which operates barely in that limit, this should not lead to vastly incorrect results.

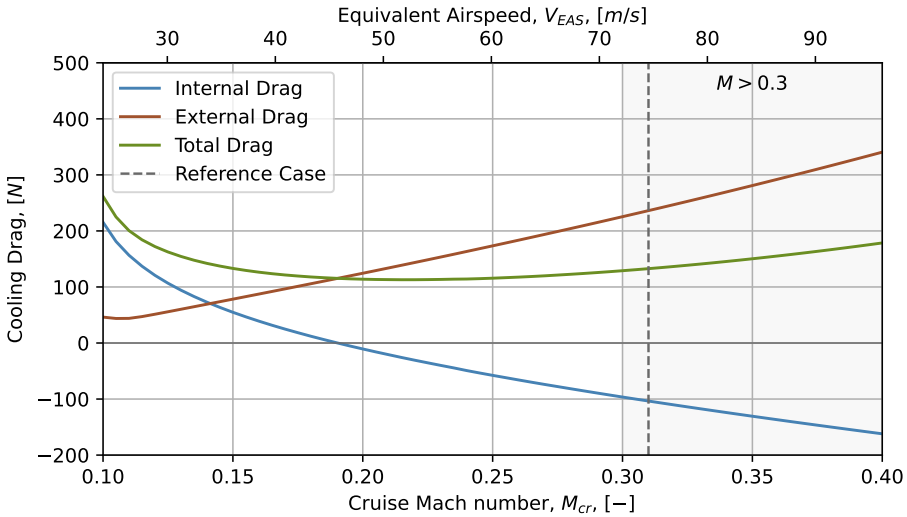


**Figure 4.14:** The cooling drag variation with the Mach number on the bottom x-axis and the equivalent airspeed in cruise on the top x-axis for the base FTHX (see Table 4.3) with the 1 MW TMS specified in Table 4.1. Adjusted duct outlet area $A_4$ to match the required heat rejection rate.

These findings echo the claim made by Meredith [14], that the drag-offset effect is improved at higher Mach numbers. Thereby, the drag model of the tool is to some extent partially validated, as the results observed here are in line with scientific literature.

# 5

# Model Validation and Verification

To ensure the proper working of the cooling drag estimation tool and estimate the level of confidence that can be attributed to the results in chapter 4, parts of the tool will be validated in different ways in this chapter. Starting off with the heat exchanger models in section 5.1, the heat transfer properties and pressure drops shall be validated against experimental data from Hao [5] and Dong [41].
Thereafter, external drag results of the CFD simulations are checked against common values in subsection 5.2.1 and the surrogate external drag model is compared with respect to the CFD results. For that, an exemplary PFHX design is analyzed with openFoam with the same method described in section 3.5 and the resulting drag force is compared to the surrogate model result.
Lastly, the results from chapter 4 are compared to results found in the Unifier19 documentation [1]. Due to the differences between the models, diverging results are expected. However, the rough values should still be in agreement and not vastly differ.

## 5.1. Heat Exchanger Model

The heat transfer and pressure drop model of the PFHX can be compared to experimental data from Hao [5], as was done by Scoccimaro [19]. The provided dimensional details and the operating conditions of one test point of Hao are noted in Table 5.1.

**Table 5.1:** The dimensions of the offset strip fin heat exchanger and the operating condition at one test point from Hao[5].

| **Core Dimensions**, [mm] | | | |
|---|---|---|---|
| $B_W \times B_D \times B_H$ = 200 $\times$ 110 $\times$ 200 | | | |
| **Air Side** | | **Water Side** | |
| $h_{fin,air}$, [mm] | 9.5 | $h_{fin,ref}$, [mm] | 2 |
| $p_{fin,air}$, [mm] | 1.7 | $p_{fin,ref}$, [mm] | 3.3 |
| $t_{fin,air}$, [mm] | 0.15 | $t_{fin,ref}$, [mm] | 0.15 |
| $\ell_{s,air}$, [mm] | 4 | $\ell_{s,ref}$, [mm] | 3 |
| $n_{pass,air}$ | 15 | $n_{pass,ref}$ | 14 |
| $T_{air,i}$, [°C] | 19.5 | $T_{ref,i}$, [°C] | 56.6 |
| $\dot{m}_{air}$, [kg/s] | 0.3625 | $\dot{m}_{ref}$, [kg/s] | 0.54 |

The heat transfer achieved in the experimental set-up is 10 kW, opposed to the 11.311 kW predicted with the heat exchanger model integrated in this work amounting to a 13.3% difference. Inaccuracies in the model are not the only source of discrepancies, however. The thermal balance analysis that Hao [5] performed shows that some heat in the experiment is lost to the ambient, such that if considering only the heat lost by the water in the experiment, the difference is less than 10%.
The pressure drop discrepancies are larger with the air side pressure drop in the experiment attaining 1 kPa, while the PFHX model predicts 0.652 kPa. The predictive model presented in Hao's work

estimates a pressure drop of about 0.9 kPa, which might point to other imperfections in the experimental execution.

The FTHX model validation is performed with the experimental data from Dong [41]. The dimensions of the HX that is used for reference are listed in Table 5.2. Water-side dimensions were not specified in the source and are therefore assumed. Likewise, the air temperature is not given, therefore it was chosen to be room temperature (21 °C). Equation 5.1 reiterates the relation between the louver specific $Re_{Lp}$ and the frontal velocity $V$ used by Dong and the the passage ratio $\sigma$.

**Table 5.2:** The dimensions of the flat tube louvered fin heat exchanger and the experimental operating conditions. Some values are not given in Dong[41] and therefore assumed.

| **Core Dimensions**, [mm] | |
|---|---|
| $B_W$ | 250 |
| $B_D$ | 65 |
| $B_H$ | 200 |
| **Air Side** | |
| $F_p$, [mm] | 2 |
| $F_h$, [mm] | 8 |
| $t_f$, [mm] | 0.2 |
| $L_a$, [°] | 28 |
| $L_p$, [mm] | 1.2 |
| $n_{pass,air}$ (assumed) | 18 |
| $T_{air,i}$ (assumed), [°C] | 21 |
| $\sigma$ (assumed), [-] | 0.632 |
| **Water Side** | |
| $h_{tube}$ (assumed), [mm] | 3.3 |
| $n_{pass,ref}$ (assumed) | 17 |
| $T_{air,i}$, [°C] | 90 |
| $\dot{m}_{ref}$, [m$^3$/h] | 2.3 |

$$Re_{Lp} = \frac{VL_p}{\sigma\nu} \tag{5.1}$$

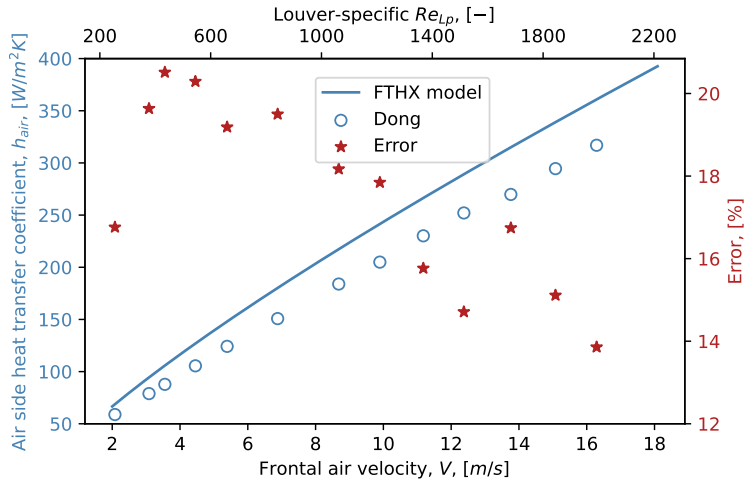


**(a)** Air side heat transfer coefficient comparison.

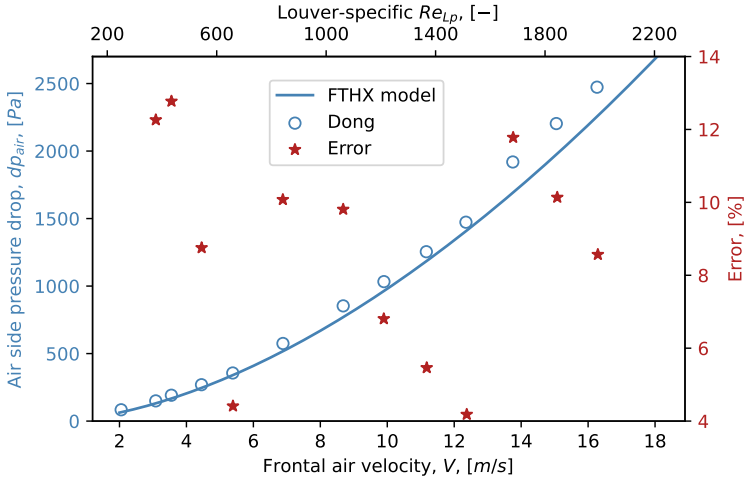


**(b)** Air side pressure drop comparison.

**Figure 5.1:** The validation for the air-side heat transfer coefficient and pressure drop of the FTHX model with experimental data from Dong[41].

The air-side heat transfer coefficient, plotted in Figure 5.1b shows overestimation of up to 20% with respect the experimental data with the largest error at very low air velocities. At the higher end of $Re_{Lp}$, the error is slightly reduced but still undesirably high. The air-side pressure drop plotted underneath is slightly better predicted with the mean error around 10%. The highest error is again at the very low air velocities. At medium $Re_{Lp}$, the pressure drop is predicted somewhat well but shoots up again above $Re_{Lp}$ with the upward shift of the experimental data suggesting that some unpredicted phenomenon occurs.

As a conclusion to this section, it can be stated that the heat transfer and pressure drop of both models are not satisfactorily agreeable with the experimental data from Hao [5] and Dong [41]. Of course, imperfections in data acquisition can explain the differences to a lesser extent but the differences are

in some points very significant. Therefore, in further work on **DRAX**, the implementation of different HX models might be worth revisiting. Note also that the heat transfer and pressure drop models were thoroughly checked to ensure that the theoretical models and the methodology from chapter 3 were properly implemented.

## 5.2. External Drag Model

The objective of this section is to assess the validity of the results for the external duct cowling drag obtained directly from openFoam. This can be done by first sanity-checking the numerical results of the base duct (Figure 3.18) with some easily estimable values for the drag, as in subsection 5.2.1. Thereafter, performing a grid-convergence study and reviewing the convergence history of the simulations can help assess if the simulation mesh and solution criteria are correctly set, such as is done subsection 5.2.2.
At last, in subsection 5.2.3, the external drag results from the surrogate model are compared to simulation results by assessing an exemplary PFHX duct design in openFoam.

### 5.2.1. OpenFoam Numerical Results

A very simple way to validate the results of the simulation is to compare them to values that one can derive with a relatively high level of confidence. First and foremost, that applies to the viscous drag. In subsection 3.5.2 of the methodology, the use of a Spalding wall function to approximate the near-wall region of the flow was presented. To assess if that approach to the representation of the region of the flow where viscous effects dominate, one may compare the viscous drag of the duct to the viscous drag of a flat plate with the same surface as the wetted area of the duct. For that, one may use the Schlichting equation for the skin friction coefficient in fully turbulent flow, noted in Equation 5.2.

$$C_f = \left[2\log_{10}(Re) - 0.65\right]^{-2.3}, Re < 10^9 \qquad (5.2) \qquad\qquad Re = \frac{V_\infty L_D}{\nu} \qquad (5.3)$$

Using the equation for $Re$ with the duct length $L_D$ as the characteristic length-scale and the take-off conditions as inputs, a $Re$ of 1.29e+7 is obtained. Since this is much larger than the critical $Re$ for flow transition of a flat plate at 5e+5, the laminar section of flow at the start of the duct cowling may be neglected when calculating the skin friction coefficient. The resulting skin friction coefficient $C_f$ using Equation 5.2 then comes out to 2.48e-3.
Conversely, by obtaining the viscous drag through simulation and extracting the wetted area of the duct in *ParaView*, the $C_f$ from the simulation can be calculated and compared. The viscous drag and wetted area (not including the duct inlet and outlet planes) of the base duct at take off are 27.068 N and 6.278 $m^2$, respectively. Going through Equation 5.4, the resulting skin friction coefficient from simulation is 2.37e-3. This represents a less than 5% difference from the value estimated above, which is satisfactory for the expected level of accuracy of the cooling drag estimation tool and simulation results.

$$C_f = \frac{D_{visc}}{A_{wet} \cdot q_\infty} \qquad (5.4)$$

The sanity check for the pressure drag component of the external drag is very similar. If the duct is considered a streamline half-body, its pressure drag coefficient $C_{D,press}$ can be compared to ones found in literature. Such value is mentioned in Miedema, 2016 [56] as being 0.09 . Thereupon, $C_{D,press}$ of the simulated duct is evaluated with Equation 5.5, the pressure drag $D_{press}$ and the frontal area $A_{max}$ of the base duct at take-off being 75.207 N and 0.4417 $m^2$, respectively. The resulting pressure drag coefficient from simulation is 0.0936, which is surprisingly close to the reference value.

$$C_{D,press} = \frac{D_{press}}{A_{max} \cdot q_\infty} \qquad (5.5)$$

Finally, the total external drag coefficient $C_D$, as derived in Equation 5.6 may be assessed and compared to values from Hoerner [23]. The $C_D$ of the base duct comes out to 0.127 which compares very well to the values Hoerner's values for belly-slung radiator housings ranging from 0.10 to 0.18 . The strong outliers among the simulated ducts are the diverterless case and the opposite case with an enlarged diverter (Var 5 and 6 in subsection 3.5.5) which have a $C_D$ of 0.0725 and 0.174, respectively.

The effect of changing the diverter height is already critically addressed in subsection 4.3.1.

$$C_D = \frac{D_{visc} + D_{press}}{A_{max} \cdot q_\infty} \tag{5.6}$$

As a conclusion of these numerical validations, one can state that the range of the openFoam simulation results matches sensible expectations. This is a very pleasing result which can serve to maintain the confidence in the validity of the external drag results. The following subsection aims to verify the simulation model by performing a grid convergence study and assessing the convergence history of the simulations.

### 5.2.2. Grid Convergence and Solver Convergence History

As was explained in subsection 3.5.2, the wall function conceived by Spalding [47] was used to reduce the $y^+$ requirement of the mesh around the duct. As such, the grid was generated with a $y^+$ value of 153, allowing for a much coarser grid than if no wall function is used, which necessitates $y^+$ of 1.
The meshes of the 8 duct variations were also made with a $y^+$ aim of 153. To assess if there are significant changes when the the near-wall inflation layer of cells is refined, the base duct simulation can be rerun with a $y^+$ value half as big as the initial value, hence 76.5, and thereupon compared to the base results. The inflation layer is again extended to the point where the final layer has a dimension similar to the surrounding castellated mesh. Thereby, 10 cell layers are inflated with the last layer thickness being 3.1 mm and the overall inflation layer thickness being 15.6 mm, similar to the base mesh where those values are 3.0 mm and 11.9 mm, respectively.
Table 5.3 shows the results of the initial simulation and the refined case. The drag results of the refined case do differ with respect to the base with the resulting pressure drag in the refined case being 7.46% smaller than in the initial simulation and the total pressure drag being 6.05% smaller than the base. While this shows that grid refinement changes the results and even further refining the grid may still lead to more accurate results, the increase in runtime of the refined case by more than 70% represents an argument in favor of the less refined base case, given that the results are not dramatically different. Moreover, the differences between the base mesh and the refined mesh cannot be extrapolated to even lower $y^+$ as it just as well may be that for a more refined mesh, the resulting drag values rise with respect of what is here the refined mesh.
On top of that, the analyzed duct is very rudimentary. For a case where the drag of a known specific design is analyzed, an increase in runtime even beyond the refined case would very likely be acceptable, since the required fidelity of the results is much higher. For the tool that is built in this work, the values seem accurate enough, as is shown in subsection 5.2.1.

**Table 5.3:** The simulation results of the initial and refined simulation of the base duct at take-off conditions.

| | | **Base**, $y^+ = 153$ | **Refined,** $y^+ = 76.5$ | Difference, [%] |
|---|---|---|---|---|
| Timestep | [s] | 0.2189 | 0.2275 | +3.93 |
| Clocktime | | 9045 | 15539 | +71.80 |
| $D_{press}$ | [N] | 75.2066 | 69.5992 | -7.46 |
| $D_{visc}$ | | 27.0676 | 26.4866 | -2.15 |
| $D_{ext}$ | | 102.2742 | 96.0858 | -6.05 |
| $C_{D,press}$ | [-] | 0.09363 | 0.08666 | -7.46 |
| $C_f$ | | 2.371e-3 | 2.320e-3 | -2.15 |
| $C_D$ | | 0.1273 | 0.1196 | -6.05 |

Figure 5.2 shows the convergence history of the base duct and its refined version along with the duct variations. The y-axis of Figure 5.2 is normalized with respect to each simulation's converged value, in an attempt to make the various plots more comparable. At the start of the simulation, there are large oscillations for each of the ducts. Then, in all cases but Var5, the drag force rapidly decreases, undershoots its final value and slowly comes back up and converges to the final state.
For Var5, which is the diverterless duct, the convergence history looks much different. Instead of the large undershoot shown for the duct variations that do have a diverter, the drag value in Var5 early on starts oscillating around the final value. As such, the simulation already converges at half the simulation

timesteps than the other ducts. It is also interesting to see that the convergence history of the refined base duct, presented above behaves in line with the reference case base duct. In fact, the convergence, not only in real terms, i.e. the runtime, is increased but also the duration in simulation timesteps that is plotted in Figure 5.2 is lengthened.
Rounding up, the simulations all look well converged, such that the conclusion may be drawn that the drag force convergence criterion was set correctly.

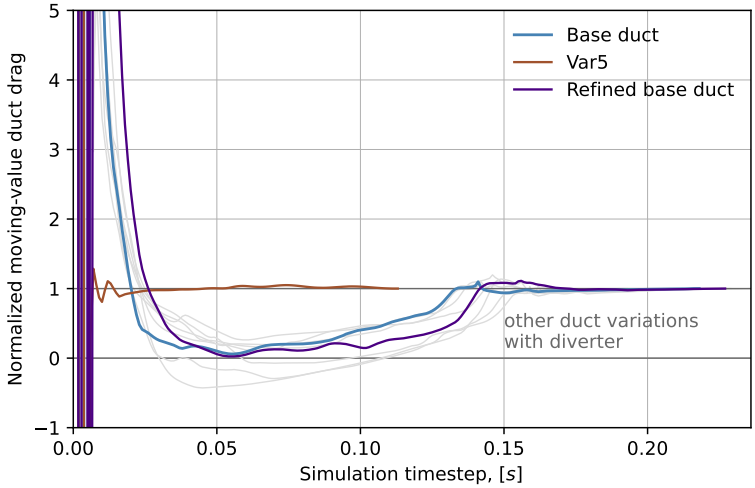


**Figure 5.2:** Caption

### 5.2.3. Surrogate Model validation

While the surrogate model for external drag constructed in subsection 3.5.5 is one of the major advances of this model compared to existing models, it is also expected to be one of the pieces in the cooling drag estimation tool with the lowest fidelity. To check if the surrogate model gives a good enough representation of the external drag, the flow around the duct of a PFHX output design is simulated in openFoam and the resulting drag checked against surrogate model outputs.
This is done for the take-off condition as well as the duct in its cruise condition, with the contracted outlet nozzle. For the cruise duct, the simulation is once performed under ambient take-off conditions, since that is how the model data was generated and then again for ambient cruise conditions, to see how the negligence of $Re$ effects in the surrogate model might affect the quality of results. This also means that in order to maintain the same $y^+$ in cruise, the mesh needs to be refined with respect to the one from the take-off condition, as the $Re$ changes between take-off and cruise. As a result, the wall-adjacent cell has a height of 1 mm, the inflation layer consists of 7 cell layers and the total inflation layer thickness is 13.3 mm. An additional particularity of the simulation performed under cruise conditions is that the duct inlet and outlet boundary conditions are adjusted to reflect the effect of spillage in cruise.

The drag coefficients of the surrogate model and the openfoam simulation for the take-off duct are compared in Table 5.4. While the viscous drag values agree rather well, there is a significant difference for the pressure drag that is predicted at take-off. The total external drag estimated with the surrogate model is 13.7% smaller than the simulation result. Moreover, Table 5.4 shows that the transformation function $f_A(h_{max}/L_D)$ that derives the wetted area from the frontal area of the duct slightly underestimated the wetted area $A_{wet}$. The deviation of the total drag by more than 10% is not favorable but it can still be considered within acceptable measures.

**Table 5.4:** The comparison of the simulation results for the external drag versus the values predicted with the surrogate model. Take-off duct generated for a PFHX at take-off conditions. Values for single duct.

| Take-Off PFHX | | Simulation | Surrogate Model |
|---|---|---|---|
| $D_{press}$ | [N] | 82.6722 | 69.4955 |
| $D_{visc}$ | | 28.4164 | 26.332 |
| $D_{ext}$ | | 111.0886 | 95.8275 |
| $A_{max}$ | [m$^2$] | 0.516599 | 0.516599 |
| $A_{wet}$ | | 6.45822 (extracted) | 6.101287 (estimated) |
| $C_{D,press}$ | [-] | 0.0880148 | 0.073986534 |
| $C_f$ | | 0.0024199 | 0.002373624 |
| $C_D$ | | 0.1182675 | 0.102020197 |

The results of the cruise duct comparison are slightly more off. Table 5.5 contains the results of the two simulations performed for the cruise duct and the surrogate model. Comparing the drag coefficients of the take-off simulation and the surrogate model, the surrogate model assumes a $C_D$ before applying the spillage factor is 18% smaller than the corresponding simulation projects. The largest error is found in the pressure drag coefficient, indicating that the effect of contracting the outlet nozzle on the external drag is still underestimated.
Before moving on to the comparison between the simulation under cruise ambient and duct boundary conditions, recall that the surrogate drag model was constructed under the assumption that data gathered under take-off conditions would serve as a good enough basis for the drag coefficient in cruise. Hence, this prior comparison validates if the model does what it was made to do, namely, give the $C_D$ of a certain duct cowling under take-off conditions, which can then be scaled with dynamic pressure. This next analysis checks not only how the surrogate model compares with the simulation in cruise but also checks the validity of the aforementioned strategy.

The pressure drag in cruise obtained by the simulation under cruise conditions is much lower than the one from the surrogate model due to the spillage being accounted for already. In fact, the simulated pressure drag is so low that it ends up being smaller than the viscous drag and even the pressure drag from the duct at take-off that has no spillage. The friction coefficient is in line with expectations and actually slightly lower than under take-off conditions, attributable to the higher $Re$ in cruise.
To better understand what happens in the cruise simulation, one should take a closer look at the simulation outputs. For that, observe the convergence history of that particular simulation in Figure 5.4 as well as the pressure coefficient field in Figure 5.5 and the axial velocity field in Figure 5.3.
Starting off with Figure 5.4, one may notice that the simulation does not meet the converge criterion. In fact, after a timestep of about 0.35 s it enters a state of constant oscillation, hinting that some transient effect, such as unstable flow or vortex shedding is taking place, which prohibits convergence. This was not present for the simulations that were run to gather data for the surrogate model. Subsequently, the display of the axial velocity field in Figure 5.3 shows a significant area of recirculating flow above the duct inlet. By calculating the pressure coefficient $C_p$ over the simulated half-duct in ParaView, Figure 5.5 can be generated, which shows that the separated flow above the inlet generates a considerable suction effect, which given the diverging shape of the front part of the duct, creates a substantial forward force.

**Table 5.5:** The comparison of the simulation results for the external drag versus the values predicted with the surrogate model. Cruise duct generated for the PFHX at take-off and cruise conditions. Values for single duct.

| Cruise PFHX | | Sim. (Take-off, $SR = 0$) | Sim. (Cruise) | Surrogate Model |
|---|---|---|---|---|
| $D_{press}$ | [N] | 99.831 | 32.715 | 146.13824 |
| $D_{visc}$ | | 27.143 | 47.6498 | 49.36957 |
| $D_{ext}$ | | 126.974 | 80.3644 | 107.603 (195.508 w/o spill.) |
| $A_{max}$ | [m$^2$] | 0.5166 | 0.5166 | 0.5166 |
| $A_{wet}$ | | 6.1098 | 6.1098 | 6.0997 |
| $C_{D,press}$ | [-] | 0.1063 | 0.01858 | 0.08298 |
| $C_f$ | | 0.002443 | 0.002288 | 0.0023743 |
| $C_D$ | | 0.13518 | 0.04563 | 0.06110 (0.1110 w/o spill.) |

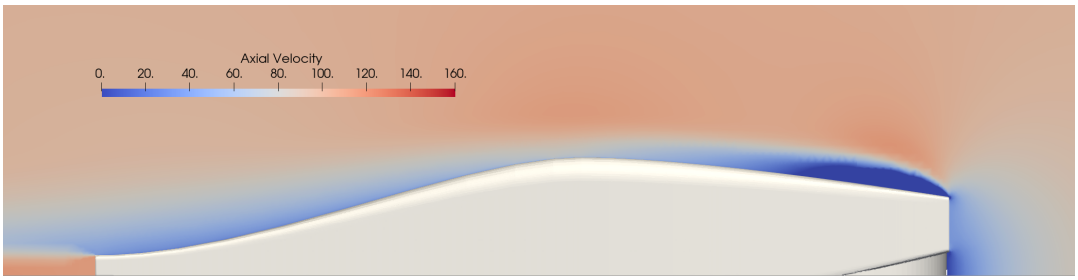


**Figure 5.3:** The velocity field around the cruise duct with cruise ambient and boundary conditions. Generated in ParaView for the last simulation timestep (t=0.5s). $Re$ = 1.52e7, $SR$ =63%

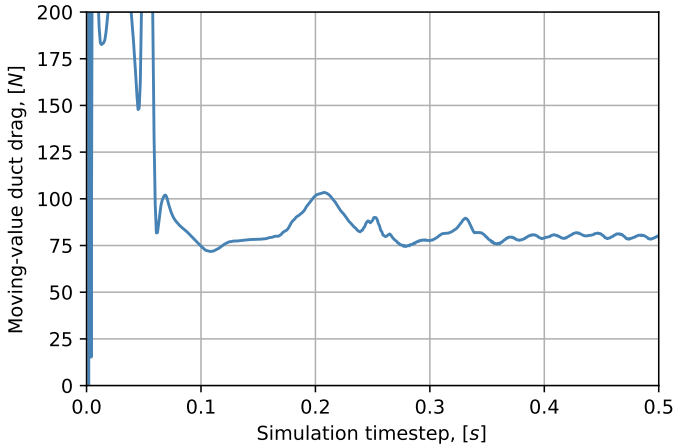


**Figure 5.4:** The convergence history of the cruise simulation

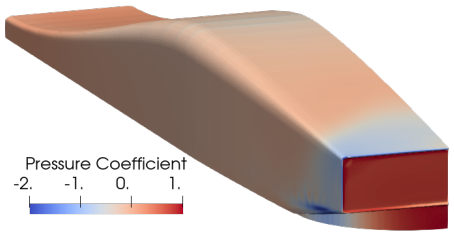


**Figure 5.5:** The pressure coefficient $C_p$ on the half duct surface that is simulated in openFoam. Pendant to Figure 5.3.

This would suggest that the lip suction effect predicted at take-off is in fact even more pronounced in cruise. However, it is hard to imagine that the difference in the drag coefficient that is found here can be explained only through this lip suction effect which probably means that the $Re$ effects are also very pronounced between take-off and cruise. For instance, it is likely that the higher $Re$ delays detachment on a longer part of the curved-down duct aftbody.

The lip suction effect that is predicted in the simulations seems very large and itself should be checked against expectations from literature. According to Bräunling [52], in an ideal flow without any losses or viscous effects, the lip suction effect should in theory be able to offset all of the pre-entry ram drag, which is denoted in Equation 5.7. According to NASA [51], in reality the offset of pre-entry drag amounts to 30%-60%, depending on the design.

$$D_{pre} = \dot{m}_1 \cdot (V_1 - V_0) + A_1 \cdot (p_1 - p_0) \tag{5.7}$$

When spillage is nil, the pre-entry ram drag $D_{pre}$ is zero. As spillage goes up, so does $D_{pre}$. In this work, the pre-entry drag is integrated within the internal drag model, since it considers the system (0-4) as one and not as two such as (0-1) and (1-4). The reduction in cooling drag that is attributed to lip suction in the surrogate model above is 87.9 N for one duct cowling. If one calculates the pre-entry ram drag of the PFHX installation above, it comes out to 250.67 N. Thereby, the lip suction offset amounts to 35% of the pre-entry ram drag, which actually puts it on the conservative side of estimates from [51]. It can thus positively be said that the lip suction effect, which has caused some counterintuitive results in chapter 4 in fact does agree in magnitude with common literature.

## 5.3. Cooling Drag Results

Lastly, the cooling drag and duct sizing model can be compared to the values found for cooling drag in Unifier19 [1]. The key data for estimating the cooling drag of one of the aircraft candidates within the Unifier 19 project, called PVS1, is presented in Table 5.6. The reporting around cooling drag in the Unifier19 document [1] suggests that the TMS features are estimated with the help of an early stage sizing tool. As a consequence, the level of confidence that can be attributed to this data is possibly low. The report also states values for cooling drag, claimed to be calculated with the methodology of Hoerner [23]. It is assumed that a HX similar to the PFHX from this work is implemented in the Unifier19 tool. Given that the detailed HX dimensions are not provided, the air side and coolant side passage properties are taken from Table 4.2.
While the reference TMS used in chapter 4 has a constant heat rejection rate, the one on the PVS1 concept varies throughout the mission. As a result, the duct and the HX are slightly over-engineered for the cruise condition, which might in fact be beneficial to reducing just the cooling drag, as was seen in chapter 4.

**Table 5.6:** Fuel Cell and Thermal Management System data of the PVS1 Unifier19 design candidate. Data as reported in public document [1]

| | **Climb** | **Cruise** |
|---|---|---|
| FC electric power output, [kW] | 782.3 | 524 |
| FC efficiency, [-] | 0.52 | |
| Airspeed, [m/s] | 48 | 77 |
| Coolant flow rate, [l/min] | 180 | 120 |
| Coolant FC inlet temperature, [°C] | 45 | |
| Coolant | 50/50 MEG | |
| Number of FC HX | 2 | |
| HX width, [mm] | 1100 | |
| HX height, [mm] | 880 | |
| Combined FC HX frontal area [$m^2$] | 1.936 | |
| Area-proportional FC cooling drag, [N] | 1,239 | 682 |

Furthermore, not being given in the documentation, the HX depth and tilt are assumed to be 15 cm and 0-70°, respectively. Note that the cooling drag value provided in the public documents sums up cooling drag for the FC and other power electronics in one number without giving any indication of which system causes what proportion of cooling drag, or if external drag is included in the calculation, although the fact that cooling drag in cruise is positive and much larger than 0 hints towards external drag sources being accounted for. The combined size of all the HX is also known, such that one may derive the proportion of FC-caused cooling drag from the proportionality of its HX frontal area, as it is noted in the last row of Table 5.6.
The HX is used as an input to the duct sizing method described in section 3.6 with the cooling drag results shown in Figure 5.6. For the HX tilt angle of $\theta = 0°$, the results are in a similar range, however when changing the tilt to 70° the model naturally predicts much lower cooling drag. Due to the fact that many essential design details are not given in the documentation and therefore guessed, this result is fine. Moreover, the difference between the cooling drag at take-off and cruise are in line with the Unifier19 model.

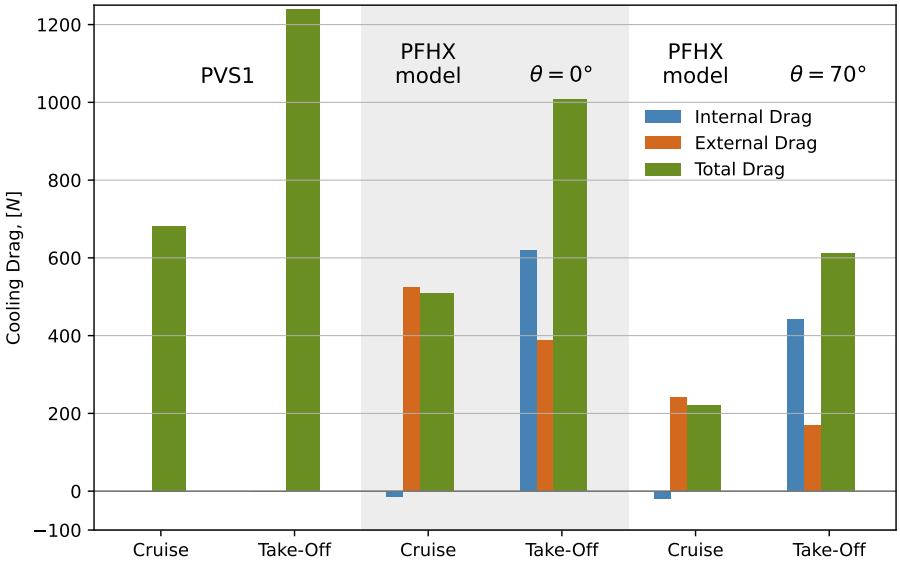


**Figure 5.6:** The comparison of the PVS1 Unifier19[1] design candidate cooling drag to the results from the PFHX model in this work.

# 6

# Conclusions

To conclude this work, one may recapture its main findings and see how they reflect the research questions that were initially formulated. Thereafter, the extent to which the research objective has been fulfilled can be assessed before expressing recommendations for future work, both on this tool as well as other studies surrounding cooling drag and TMS integration.

First and foremost, the extent to which cooling drag impacts aircraft performance is non-negligible. Accounting for the optimal heat exchanger designed for the 1 MW reference case, the cruise cooling drag of 133 N represents a significant penalty. Assuming a lift-to-drag ratio of 15.1 for a 19-seater aircraft, like the PVS1 concept in Unifier19[1], these 133 N of cooling drag would be equivalent to the drag-due-to-lift of an additional 205 kg of payload.
In addition to the on-paper performance, solutions to stowing away HXs within an aircraft were addressed by generating simplified, but relatively streamlined duct cowlings around the HX. By devising a set of design rules and defining a range of key duct design variables and constraints and furthermore simplifying the problem of the fuselage-bounded duct to a wall-bounded duct, a quick and easy way to generate realistic ducts with corresponding drag estimates was developed. Moreover, it was shown within a preliminary scope that varying certain design features, such as the diverter height and the burial constraint brings the potential to greatly reduce external drag. Still, the method that brought about these results crucially neglects the fuselage boundary layer, such that the positive effects of reducing the diverter height or removing it altogether are likely overestimated. Very conclusive however, is the observation that tilting the heat exchanger is always favorable, which is also the most effective way of reducing the frontal area of the external cowling while maintaining a large HX frontal area.

When this work was initiated, the question to which extent the so-called Meredith effect could reduce cooling drag stood open. The introduction of an external drag model, adapted to the cowling shapes that are expected to house the HX, as well as the consideration of internal losses at the very least reduce that interval. It was shown that for the optimized heat exchangers, the internal force due to heat recovery is present but only under the condition of a very well designed nozzle. Moreover, the generated force is insufficient to let the HX installation act as a thruster. Crucially, it was shown that attempting to exploit this effect while neglecting the external drag of the installation lead to much worse results in overall cooling drag of the installation, despite the internal system offsetting more drag than in a wholly drag-optimized system.

The effect of changing the TMS operating temperature on cooling drag was demonstrated and showed that reducing the HX inlet temperature of the coolant did not affect the cooling drag in cruise but severely increased it at take-off. The installation size of the ducted ram-air HX is directly impacted by the TMS operating temperature and increases with lower temperature. Inversely, this means that being able to push the operating temperature envelope of the FC and thereby allowing for higher coolant inlet temperatures, incurs significant reductions in cooling drag during take-off all the while making the installation more compact. Furthermore, a higher TMS operating temperature will allow to maintain a large enough

temperature gap between the ambient and the coolant even on hotter days, thus extending the operational envelope of the system.
Interestingly, the effect of varying the critical temperature offset at take-off on overall cooling drag was in parts contrary to anticipations. In line with expectations, the take-off cooling drag during very extreme heat events (45 °C ambient) is 50% higher than on a moderately hot day (30 °C ambient), this is mostly explained by the larger air mass flow rate at take-off. Subsequently placing a system sized for a 30 °C temperature offset (45 °C ambient) in normal cruise conditions actually leads to projections of smaller cooling drag than of the base system. The influences leading to that are, firstly the better heat recovery capabilities of the oversized installation and secondly, the increase in lip suction at the inlet, which makes up for the increase in drag associated to the larger frontal area of the installation. While this provides an interesting insight into the caveats of cooling drag estimation, looking at the installation sizes produced with **TOS** also shows that these installations are bulkier and likely include other weight penalties which are not made up for by the small absolute difference in cooling drag. Nevertheless, this analysis shows that over-engineering ones installation for an extreme heat event is possibly less penalizing from a drag point of view, than engineers think. Of course, this assumes a variable area nozzle to regulate airflow but this system can be quite simple, for example a single flap mechanism.

Going through the research questions one-by-one:

**Research Question 1**

How does one best integrate HX into an aircraft to ensure good TMS operation and minimal burden on aircraft performance?

Try to reduce the frontal area of the installation by tilting the HX and allowing for it to be partially buried within the fuselage. The latter is only possible to a certain extent as, if the air inlet is directly followed by the diverter, the lower ramp angle of the diverter can limit the burial depth for a given diverter length.

**Research Question 2**

How does cooling drag scale with the ambient conditions and TMS operational conditions?

The cooling drag is very strongly impacted by the TMS operational temperature throughout the mission. A higher ambient temperature also affects the cooling drag. However, sizing an installation to handle a very high critical ground temperature does not lead to severe Drag impediments of the same system under normal cruise conditions, despite being over-engineered.

**Research Question 3**

How do internal and external drag sources scale with each other?

At take-off, internal drag sources dominate due to the higher required air mass flow rate. In cruise the internal drag offset is insufficient to provide a net thrust force of the installation, even when taking into account favourable effects such as inlet lip suction.

**Research Question 4**

What balance between internal and external drag is the best to improve aircraft performance? (i.e., is an internally streamlined design at the cost of external losses advantageous or vice versa?)

Only regarding cooling drag, the answer is non-trivial. The internal ducting should be well designed to avoid excessive losses in the diffuser and nozzle. However, minimizing the external outline of the installation is crucial to reducing the sum of internal and external drag sources.

**Research Question 5**

Which type of HX provides the best drag performance? PFHX or FTHX?

This cannot be stated definitively. Only if the mass of the HX and the added TMS pumping power due to pressure losses are taken into account, a more precise answer can be given. However, the results have shown that when both HX have similar channel properties, the optimized PFHX yields lower cooling drag than the FTHX, largely due to fitting into a more compact duct.

**Research Question 6**

What HX shape provides the best drag performance? Thin and wide or thick and compact?

Similarly to RQ 5, the answer is non-trivial if one considers both internal and external drag sources. If only internal drag sources are considered, a thin HX with a large frontal area appears best, with the thickness eventually being limited by the available design space (either through constraints on the frontal area or channel dimensions) and the pressure drop of the coolant.

**Research Objective**

*Develop a model/ method which estimates cooling drag for ducted ram-air heat exchangers on a base of influential parameters.*

The objective was met. The tool combines a range of semi-empirical models and a duct sizing strategy, which makes the installation less abstract and more tangible with respect to an aircraft fuselage. Moreover, the observance of phenomena such as the inlet lip suction and the general presence of a dynamic external drag surrogate model provides a substantial advancement with respect to existing models. However, the method lacks a model to take into account the fuselage boundary layer in the air ingestion and the external drag interference effects that take place.

# 7

# Recommendations

Lastly, certain recommendations on further work on the tool and studies in research surrounding cooling drag and HX installations can be made.

The sensitivity analysis on the nozzle efficiency has shown that the model is very sensitive to ducting losses at take-off, when the freestream dynamic pressure is low. In order to limit the cooling drag at take-off, the nozzle design must be very efficient. It is likely that more design freedom could be achieved if a puller fan is included in the duct model, which restitutes some of the lost pressure. Furthermore, it would be interesting to elaborate, if there can be a net power saving from including a puller fan in the system. This should, moreover, not neglect the effect of a windmilling puller fan at cruise.
An additional study in itself could be the more detailed design of subparts of a HX installation, including a puller fan and the variable area nozzle.

The effect of the boundary layer on air intake was mitigated in the base design by raising the inlet outside of the fuselage boundary layer. Simultaneously, when constructing the surrogate drag model, it was shown that a diverterless duct may reduce external cooling drag. To evaluate the extent to which this is true, a mass momentum model of the boundary layer may be included to reflect the reduction of air mass flow into a boundary layer submerged inlet. In a more precise analysis that is outside of the scope of this tool, the effect of the fuselage boundary layer on the duct drag may be modeled in a more computationally expensive CFD simulation than the one performed in this work.

In order to assess the overall performance of the installation, besides the drag, also the mass of the HX and the cowling as well as the added pumping power due to the coolant pressure drop could be included in one single objective. For instance, the increase in power consumption of all these contributors could be unified into one value that should be minimized. In that case, it would be interesting to see not only how different HX types compare to each other, but also, how the optimum design of the HX might change.

A likely extension to the tool would also be the inclusion of a 2-phase heat transfer model in order to facilitate the use of **DRAX** in connection with Vapor Compression Cycles (VCC) and pumped 2-phase TMS (P2P), that were discussed in subsection 2.1.1 and subsection 2.1.2.
Beyond that, the addition of a microtube heat exchanger ($\mu$HX) model into DRAX would represent a very significant step forward in assessing the viability of this type of HX in the context of large heat loads produced by FC. Certainly, the size of the installations pictured in chapter 4 grants more attention to more compact solutions promised through $\mu$HX, which may affect the appearance and performance of aircraft to a lesser extent.

The analysis of the ducted ram-air HX in this work was conducted under the assumption of perfectly axial flow. However, the inflow conditions would change with angle of attack and yaw angle and likely negatively affect the air mass flow and the external drag caused by the installation. Setting up a campaign of simulations or experiments that reflect the changes in cooling performance and drag could

give impactful insights into how to better size the installation for the critical condition, i.e. take-off and early climb, since that is when the largest deviations in inflow direction are expected. One such test campaign was recently performed by AeroDelft [57] where the airflow to the HX was observed at different angles of attack. Naturally, these test campaigns are very costly. The AeroDelft test took place in the open jet facility (OJF) of TU Delft which requires a large allocation of budget and work hours. Thus, widening the scope of CFD simulations to analyze the external drag would be a more viable option.

Another point of attention when it comes to experimentation and further simulation is the effect of lip suction due to spillage. The simulations performed as part of this work point towards the lip suction being a major force on the installation. It would be unwise, however, to overestimate its effect and thereby underestimate the cooling drag. One way to more conclusively determine the lip suction effect would be to model a whole duct and cowling, where the HX is represented by a porous medium. That way, the lip suction effect is less impacted by the boundary condition on the duct inlet in the simulation as the flow around the inlet lip is no longer constrained.

At last, as was noticed in chapter 5 when validating the heat exchanger models, the models do not seems to show particularly good agreement with experimental data. If a type of HX that should be implemented in a TMS and its design features are known, a test campaign on that HX should be performed. The acquired data for the pressure drop and the heat transfer could be used in **DRAX** to more accurately represent the HX.

# References


[1] D. Eržen et al. *Unifier19; D2.2: Final concurrent design report*. European Commission: Project CORDIS, 2021.

[2] B. Sundén and J. Fu. *Heat transfer in aerospace applications*. 1st ed. London, United Kingdom: Academic Press, 2017.

[3] F-Chart Software. *Heat Transfer Library: Compact HX*. URL: https://fchart.com/ees/heat_transfer_library/compact_hx/hs100.htm#reference (visited on 06/11/2025).

[4] E.U. Schlünder et al. *Heat Exchanger Design Handbook*. 1st ed. VDI-Verlag GmbH, 1983. ISBN: 3-1841-9080-3.

[5] J.-H. Hao et al. "An experimental study on the offset-strip fin geometry optimization of a plate-fin heat exchanger based on the heat current model". In: *Applied Thermal Engineering* 154 (2019), pp. 111–119. ISSN: 1359-4311. DOI: https://doi.org/10.1016/j.applthermaleng.2019.03.072.

[6] H. Lim, U. Han, and H. Lee. "Design optimization of bare tube heat exchanger for the application to mobile air conditioning systems". In: *Applied Thermal Engineering* 165 (2020), p. 114609. ISSN: 1359-4311. DOI: https://doi.org/10.1016/j.applthermaleng.2019.114609.

[7] M. Springer and K. Thole. "Entry region of louvered fin heat exchangers". In: *Experimental Thermal and Fluid Science - EXP THERM FLUID SCI* 19 (Aug. 1999). DOI: 10.1016/S0894-1777(99)00028-X.

[8] D. Küchemann. *Aerodynamics of Propulsion*. 1st ed. New York, United States of America: McGraw-Hill Book Company, Inc., 1953.

[9] Hartzell Propeller. *Hydrogen-Powered Flight Makes Major Headway: Universal Hydrogen Marks Milestone First Flight*. URL: https://hartzellprop.com/hydrogen-powered-flight-hartzell-propeller/ (visited on 11/28/2024).

[10] Twitter. *Universal Hydrogen Co.* URL: https://twitter.com/Universal_H2?ref_src=twsrc%5Etfw%7Ctwcamp%5Etweetembed%7Ctwterm%5E1615858592799920129%7Ctwgr%5Eec3c62fb7e0114115f651bea8227da6b93f2529f%7Ctwcon%5Es1_&ref_url=https%3A%2F%2Fwww.geekwire.com%2F2023%2Fhydrogen-plane-testing-central-washington%2F (visited on 11/28/2024).

[11] ZeroAvia. URL: https://zeroavia.com/ (visited on 06/11/2025).

[12] Fuel Cell Works. *PROJECT NEWBORN Advances Hydrogen-Powered Aviation with Integrated Fuel Cell Propulsion System*. URL: https://fuelcellsworks.com/2025/04/16/clean-energy/project-newborn-advances-hydrogen-powered-aviation-with-integrated-fuel-cell-propulsion-system (visited on 06/11/2025).

[13] H2Fly. *Our Vision*. URL: https://www.h2fly.de/vision/ (visited on 06/11/2025).

[14] F.W. Meredith. *Cooling of Aircraft Engines*. Aeronautical Research Committee, 1935.

[15] S. Kazula. *Variable Pitot-Triebwerkseinlässe für kommerzielle Überschallflugzeuge*. 1st ed. Wiesbaden, Germany: Springer Vieweg, 2022. DOI: https://doi.org/10.1007/978-3-658-35456-5.

[16] F. Pittaluga. "A Set of Correlatons Proposed for Diffuser Performance Prediction". In: *Mechanics Research Communications* 8(3) (1981), pp. 161–168. DOI: https://doi.org/10.1016/0093-6413(81)90005-7.

[17] G. Sovran and E.D. Klomp. *Experimentally Determined Optimum Geometries for Rextilinear Diffusers with Rectangular, Conical or Annular Cross-Section*. Elsevier, 1967, pp. 270–319.

[18] M.R. Nichols. *Investigation of Flow through an Intercooler set at various Angles to the Supply Duct*. NACA, 1942.

[19] A. Scoccimarro. "Preliminary Design Methods for the Thermal Management of Fuel Cell Powered Aeroengines". Master's thesis. TU Delft, 2023.

[20] P. Hill and C. Peterson. *Mechanics and Thermodynamics of Propulsion*. 2nd ed. Addison-Wesley, 1992. ISBN: 0201146592. URL: https://books.google.se/books/about/Mechanics_and_Thermodynamics_of_Propulsi.html?id=uYJTAAAAMAAJ&redir_esc=y.

[21] T.L.C. Hoogerdijk. "Aircraft Integration of Air-Based Thermal Management Systems for Propulsive Fuel Cell Systems". Master's thesis. TU Delft, 2023.

[22] M. Niehuis and P. Jeschke. "Performance Calculation of the Thermal Management System for a Fuel Cell Aircraft Engine". In: Sept. 2024. DOI: 10.33737/gpps24-tc-047.

[23] S.F. Hoerner. *Fluid-Dynamic Drag: theoretical, expermintal and statistical information*. 1st ed. United States of America: Published by the Author, 1965.

[24] L.J. van Dongen. "MODELLING AND DESIGN GUIDELINES FOR RAM AIR DUCTS USING THE MEREDITH EFFECT". Master's thesis. TU Delft, 2024.

[25] F. Yu, J. Bartasevicius, and M. Hornung. "Comparing Potential Flow Solvers for Aerodynamic Characteristics Estimation of the T-FLEX UAV". In: (2022). Presented at the 33rd Congress of the International Council of the Aeronautical Sciences (ICAS). URL: https://www.icas.org/ICAS_ARCHIVE/ICAS2022/data/papers/ICAS2022_0367_paper.pdf.

[26] V. Habrard et al. "Thermal Management System Modeling for Preliminary Design of Fuel Cell-Based Aircraft". In: *AIAA 2023 Forum* 4303 (2023). DOI: https://doi.org/10.2514/6.2023-4303.

[27] H. Kellermann et al. "Design and Optimization of Ram Air–Based Thermal Management Systems for Hybrid-Electric Aircraft". In: *Aerospace* 8.3 (2020). DOI: https://doi.org/10.3390/aerospace8010003.

[28] P. Malan and E.F. Brown. "Prediction of Inlet Drag for Aircraft Conceptual Design". In: *ICAS* 90.5.3.1 (1990). https://www.icas.org/ICAS_ARCHIVE/ICAS1990/ICAS-90-5.3.1.pdf.

[29] P.P. Walsh and P. Fletcher. *Gas Turbine Performance*. 2nd ed. Oxford, United Kingdom: Blackwell Science, 2004.

[30] R.W. Gilbey. *ESDU item 86002: Drag and pressure recovery characteristics of auxiliary air inlets at subsonic speeds*. IHS, 2004.

[31] J. Roskam. *Airplane Design Part 5: Component Weight Estimation*. Ottawa, Kansas, Unitded States of America: Roskam Aviation and Engineering corporation, 1985.

[32] R.K. Shah and D.P. Sekulić. *Fundamentals of Heat Exchanger Design*. Hoboken, New Jersey, Unitded States of America: John Wiley and Sons, 2003.

[33] R. M. Manglik and A. E. Bergles. "Heat transfer and pressure drop correlations for the rectangular offset strip fin compact heat exchanger". In: *Experimental Thermal and Fluid Science* 10.2 (1995). Aerospace Heat Exchanger Technology, pp. 171–180. ISSN: 0894-1777. DOI: https://doi.org/10.1016/0894-1777(94)00096-Q.

[34] R. da Silva Collares. "A thermal management system parametric model for fuel cell powered aircraeft conceptual design". Master's thesis. Universidade de São Paulo, Escola de Engenharia de São Carlos, 2024.

[35] S. Katzoff. *High-Altitude Cooling, V-Ducting and Cowling*. NACA, 1948.

[36] W. M. Kays, A. London, and Ernst R. Eckert. "Compact heat exchangers". In: *Journal of Applied Mechanics* 27 (1960), pp. 377–377. DOI: https://doi.org/10.1115/1.3644004.

[37] J.D. Mattingly, W.H. Heiser, and D.T. Pratt. *Aircraft Engine Design*. 2nd ed. 1801 Alexander Bell Drive, Reston, VA 20191-4344: American Institute of Aeronautics and Astronautics, Inc, 2002.

[38] PWR Advanced Cooling Technology. *Tube and Fin Heat Exchangers*. URL: https://www.pwr.com.au/products/tube-fin-heat-exchangers/ (visited on 06/11/2025).

[39] Robert J. Ribando. *Heat Transfer Today: Heat Exchanger Photos*. URL: https://www.robertribando.com/modules/heat-exchanger-photos/ (visited on 06/11/2025).

[40] F.P. Incropera et al. *Fundamentals of Heat and Mass Transfer*. 6th ed. 111 River Street, Hoboken, NJ: John Wiley and Sons, Inc., 2007.

[41] J. Dong et al. “Heat transfer and pressure drop correlations for the multi-louvered fin compact heat exchangers”. In: *Energy and Conversion Management* 48 (2007), pp. 1506–1515. DOI: https://doi.org/10.3390/aerospace8010003.

[42] CoolProp. *Welcome to CoolProp*. 2025. URL: https://coolprop.org/#welcome-to-coolprop (visited on 07/13/2025).

[43] E.Y. Ng, P.W. Johnson, and S. Watkins. “An analytical study on heat transfer performance of radiators with non-uniform airflow distribution”. In: *Proceedings of the Institution of Mechanical Engineers, Part D: Journal of Automobile Engineering* 219.12 (2005), pp. 1451–1467. DOI: 10.1243/095440705X35116.

[44] B.S. Petukhov, T.F. Irvine, and J P. Hartnett. *Advances in Heat Transfer*. 1st ed. Vol. 6. New York: Academic Press, 1970.

[45] L. Henriksson et al. “Experimental Investigation of Heat Transfer Rates and Pressure Drops through Compact Heat Exchangers - Where the Heat Exchanger is Angled Relative to the Incoming Airflow -”. In: *International Journal of Automotive Engineering* 6 (Mar. 2016), pp. 7–14. DOI: 10.20485/jsaeijae.6.1_7.

[46] The SciPy community. *scipy.optimize - newton*. 2008. URL: https://docs.scipy.org/doc/scipy/reference/generated/scipy.optimize.newton.html (visited on 06/25/2025).

[47] D. B. Spalding. “A Single Formula for the “Law of the Wall””. In: *Journal of Applied Mechanics* 28.3 (Sept. 1961), pp. 455–458. DOI: 10.1115/1.3641728.

[48] A. Wimhurst. *Computational Fluid Dynamics, Fundamentals Course 1*. Fluid Mechanics 101, 2019.

[49] F. R. Menter. “Two-equation eddy-viscosity turbulence models for engineering applications”. In: *AIAA Journal* 32.8 (1994), pp. 1598–1605. DOI: 10.2514/3.12149.

[50] Wolf Dynamics. *Turbulence modeling in OpenFOAM: Theory and applications*. 2021. URL: https://www.wolfdynamics.com/training/turbulence/OF2021/turbulence_2021_OF8.pdf (visited on 07/08/2025).

[51] Glenn Research Center, NASA. *Inlet Performance*. 2021. URL: https://www.grc.nasa.gov/www/k-12/airplane/inleth.html (visited on 10/28/2024).

[52] W.J.G. Bräunling. *Flugzeugtriebwerke: Grundlagen, Aero-Thermodynamik, Kreisprozesse, Thermische Turbomaschinen, Komponenten- und Emissionen*. VDI-Buch. Springer Berlin Heidelberg, 2004. ISBN: 9783540405894. URL: https://books.google.de/books?id=2yrCF9-XE7YC.

[53] The SciPy community. *scipy.optimize - differential*$_{evolution}$. 2008. URL: https://docs.scipy.org/doc/scipy/reference/generated/scipy.optimize.differential_evolution.html (visited on 07/13/2025).

[54] A. Melinder. *Fitting Report for MEG*. URL: https://coolprop.org/_downloads/4e6bd34ef1888b4daa1662944ee0ea7e/MEG_fitreport.pdf (visited on 08/10/2025).

[55] *MIL-HNDBK-310: Global Climatic Data for Developing Military Products. (Base Document)*. United States Department of Defense, 1997.

[56] S.A. Miedema. *Slurry Transport: Fundamentals, A Historical Overview & The Delft Head Loss & Limit Deposit Velocity Framework*. 1st ed. Delft, NL: Dr.ir. S.A. Miedema, 2016.

[57] LinkedIn. *AeroDelft*. 2025. URL: https://www.linkedin.com/posts/aerodelft_achievement-tudelft-stallspeed-activity-7345782468274208770-MzHR?utm_source=share&utm_medium=member_desktop&rcm=ACoAAEGOILUBxwk_kcU49H-AGT7YFAhPJnPO6tI (visited on 08/22/2025).